Time-reversal focusing and space-time control of interferences: novel Loschmidt Echo procedures in wave dynamics

por

Hernán Laureano Calvo

Presentado ante la Facultad de Matemática, Astronomía y Física
como parte de los requerimientos para acceder al grado de
DOCTOR EN FÍSICA
de la

Universidad Nacional de Córdoba

Marzo de 2010

Director: Dr. Horacio Miguel Pastawski

Abstract

Keywords: Time-reversal mirror; Quantum Chaos; Semiclassical theories and applications; Loschmidt Echo; Synchronization, coupled oscillators; Control Systems

PACS: 03.65.Wj; 03.67.-a; 43.60.-c; 03.65.Sq; 05.45.Mt; 05.45.Gg

The focalization of acoustic waves propagating through complex media was succesfully achieved by the time reversal mirror (TRM) procedure. In the experiment, the escaping waves are recorded as they cross the frontier between a region denoted as the cavity and a free propagating space and then re-emitted to achieve the time reversal. Surprisingly, this simple prescription allows to recover the initial excitation with high precision and constitutes an alternative version of the Loschmidt echo. The remarkable robustness of the technique against inhomogeneities in the system and imperfections in the procedure enabled several applications in Medical Physics, Oceanography and Telecommunications.

In this thesis, we addressed the TRM procedure in a completely new perspective. This consists in proposing the time reversed function inside the cavity as the target function of the injection process. This inverse time scattering approach led to the development of the perfect inverse filter, a prescription for processing the recorded information that compensates any feedback and ensures the exact time reversal of the dynamics of acoustic and quantum waves. We have also developed a novel strategy, based on the wave-particle duality intrinsic in a linear wave equation, to analyze the dynamical stability of the TRM against imperfections in the protocol and perturbations in the evolution operator.

Resumen

Palabras Clave: Espejo de reversión temporal; Caos cuántico; Teorías y aplicaciones semiclásicas; Eco de Loschmidt; Sincronización, osciladores acoplados; Sistemas de control

PACS: 03.65.Wj; 03.67.-a; 43.60.-c; 03.65.Sq; 05.45.Mt; 05.45.Gg

La focalización de ondas acústicas que se propagan por un medio inhomogéneo fue lograda con éxito a través del procedimiento conocido como espejo de reversión temporal (TRM). En este experimento, las ondas salientes son almacenadas al cruzar la frontera entre un region denominada cavidad y el espacio de propagación libre y luego son reemitidas para lograr la reversión en el tiempo. Sorpresivamente, esta simple prescripción permite recuperar la excitación inicial con gran precisión y constituye una versión alternativa al eco de Loschmidt. La notable robustez de esta técnica frente a inhomogeneidades en el sistema e imperfecciones en el procedimiento ha permitido diversas aplicaciones en áreas como Física Médica, Oceanografía y Telecomunicaciones.

En esta tesis, analizamos el procedimiento TRM dentro de una nueva perspectiva. Ésta consiste en proponer la función temporalmente revertida dentro de la cavidad como la función objetivo en un proceso de inyección. Este enfoque de dispersión inversa en el tiempo dio lugar al desarrollo del filtro de inversión perfecta, una prescripción que procesa la información registrada con el fin de compensar cualquier acción retardada y asegurar la reversión temporal exacta en la dinámica de ondas acústicas y cuánticas. Además, desarrollamos una nueva estrategia, basada en la dualidad onda-partícula intrínseca en una ecuación de onda lineal, para analizar la estabilidad dinámica del TRM frente a imperfecciones en el protocolo y perturbaciones en el operador de evolución.

Agradecimientos

Esta tesis concluye una etapa muy valiosa en mi vida contribuyendo a mi formación como físico. A lo largo de estos cinco años he tenido la satisfacción de poder aprender no sólo en el ámbito científico sino también en lo personal de aquellos con quienes he compartido el tiempo. A todos ellos les estoy enormemente agradecido.

Estoy especialmente agradecido con mi director, Horacio Pastawski, quien a lo largo de esta etapa me ha brindado su conocimiento, tiempo y dedicación. Su trasmitida pasión por la Física ha sido un motor propulsor a lo largo de mi carrera que me motivó a imaginar los problemas desde varios puntos de vista. Sin duda fue un gusto poder trabajar a su lado y ojalá pueda seguir haciéndolo en los próximos años.

Estoy muy agradecido con Rodolfo Jalabert, de quien me pude enriquecer durante mi estadía en Estrasburgo. Ha sido muy grato trabajar junto a él y aprender nuevas formas de encarar el problema de la focalización. Deseo también agradecer a Diego Wisniacki por haber aportado con discusiones y por proveernos de rutinas numéricas.

Agradezco a los integrantes del grupo LaNAIS de RMS, por la buena disposición y por generar un buen ambiente de trabajo. Quiero agradecer a Ernesto Danieli, Luis Foá Torres y Elena Rufeil, con quienes pude aprender las primeras etapas del PIF y me brindaron sus conocimientos acerca de este problema. En particular, estoy muy agradecido con Luis, por ser además un soporte clave durante este último mes de mucho trabajo en la preparación de los seminarios generales. A su vez, agradezco a mis compañeros Federico Pont y Belén Franzoni con quienes he compartido la oficina durante estos cinco años y por su eterna ayuda en todos los trámites que nos han tocado realizar. También quiero agradecer a Axel Dente con quien tuve el gusto de comenzar a diseñar nuevas rutinas en CUDA y con quien pude discutir sobre problemas de Física en común. Además, agradezco a Fernando Pastawski por sus sugerencias y correcciones de los manuscritos para publicación. Deseo agradecer también a Mariana Salas por la ayuda aportada en la corrección del inglés.

En el plano personal, quiero agradecer profundamente a mis padres y hermanos por el enorme apoyo brindado y por su constante participación durante mi carrera. A su vez, quiero agradecer a mi tío Rafael no solo por sus consejos y seguimiento a lo largo de estos años sino también por todos los libros que me ha ido legando.

Estoy tambien agradecido con mis compañeros de la "Comisión del Café", con quienes día a día ha sido un gusto tomar un café y charlar sobre temas diversos. En la última etapa, quiero tambien agradecer a Mariano Zuriaga, Fernando Zuriaga y Silvina Pérez, por los almuerzos compartidos.

Por último, y quizá más importante, quiero agradecer a Yamila, mi mujer, por todos estos años de constante apoyo y paciencia. Estoy muy feliz de haber compartido esta etapa con ella. Su inagotable fuerza de voluntad me ha permitido seguir adelante día a día y poder concluir toda esta etapa de dedicación y esfuerzo. Estoy eternamente agradecido con vos, Yami, por todo esto y ojalá la vida me regale muchos años más a tu lado!

Contents

1 On time reversal experiments and the questions they posed **1**

2 Towards the design of a perfect time reversal mirror **11**
2.1 Solution of the inverse time problem 12
2.2 Exact reversal through the Perfect Inverse Filter 16
2.2.1 Multi-dimensional external PIF 16
2.2.2 Time reversal via injection: the Quantum Bazooka 18
2.3 Internal Perfect Inverse Filter 21
2.3.1 Multi-dimensional internal PIF 25
2.3.2 Application examples 26
2.4 Comparison with other results 33
2.5 Summary 35

3 Focusing of classical waves **37**
3.1 Modeling the classical wave equation 38
3.2 Classical PIF 42
3.2.1 PIF in a two-dimensional membrane 45
3.3 The Pair Partitioning method 49
3.3.1 Unbounded systems as damped oscillations 52
3.4 Summary 55

4 Semiclassical time reversal focusing **57**
4.1 Semiclassical expansion of the quantum TRM 58
4.2 Focalization in the optimal condition 61
4.2.1 Momentum contribution 64
4.3 Spatial and temporal resolutions 66
4.3.1 Ergodic approach 68
4.4 Evaluating the focusing: The Trotter-Suzuki strategy 69
4.5 Focalization in regular systems 71
4.6 Evaluating the Loschmidt Echo: The Lanczos-Trotter method 72
4.7 Summary 75

5 Irreversible processes and the time reversal focusing **77**
5.1 Focalization in open systems 78
5.2 Focalization and the Loschmidt Echo 82
5.3 Summary 88

6 Conclusions **91**

A Calculus of Green's functions through decimation **97**
A.1 Quantum Green's functions 97
A.2 Classical Green's functions 99

B Quantum-classical analogy in discrete systems **101**

C Calculus of integral identities **105**
C.1 Scaling of the focalization 105
C.2 Focalization in perturbed Hamiltonians 106

List of Figures

1.1 Time reversal echoes in NMR . . . 3
1.2 Polarization echo by Zhang, Meier and Ernst . . . 4
1.3 Schematics of the time reversal mirror procedure by M. Fink . . . 6
1.4 The time reversal mirror in a closed chaotic cavity by Draeger and Fink . . 7

2.1 Potential profile for a scattering barrier and its corresponding tight-binding model . . . 14
2.2 Time reversal mirror and perfect inverse filter procedures in a quantum bazooka . . . 18
2.3 Energy representation of the perfect inverse filter correction in the injection function . . . 20
2.4 Probability density with mixed incoming and outgoing components for the TRM and PIF procedures . . . 21
2.5 Decomposition of the registered signal between the incoming and outgoing components . . . 22
2.6 Scheme of a quantum bazooka for the internal PIF . . . 26
2.7 TRM and PIF focalization and contrast for the quantum bazooka device . 29
2.8 Schematics of a multichannel system . . . 30
2.9 PIF corrections and detected signals in the energy representation . . . 31
2.10 Time recovering of the initial state for the TRM and PIF procedures . . . 32
2.11 Spatial distribution of the initial state . . . 33

3.1 Schematics of the harmonic model for the acoustic waves . . . 40
3.2 Scheme of the equation of motion . . . 40
3.3 Recovering of the local energy and contrast of the initial state in a Helmholtz resonator . . . 45
3.4 Scheme of the harmonic membrane and PIF correction terms . . . 48
3.5 Recovering of the initial excitation for the TRM and PIF procedures . . . 49
3.6 Relative errors in the Pair Partitioning method . . . 53
3.7 Unbounded systems through damping effects included in the Pair Partitioning 54

4.1 Scheme of the involved times in the TRM sequence . . . 59
4.2 Schematics of the Bunimovich stadium . . . 63
4.3 Scaling of the focalization with the emission interval . . . 63

4.4 Focalization amplitude for different emission intervals and sizes of the cavity 70
4.5 Scheme of the Lanczos algorithm 73
4.6 Involved times in the wave packet propagation throug the Lanczos-Trotter method 75

5.1 Focalization in opened systems 82
5.2 Focalization amplitude and the Loschmidt echo 86
5.3 Focalization under external perturbations 87

A.1 Decimation method in tight-binding systems 98
A.2 Self-energy corrections in the thermodynamical limit 99

B.1 Tight-binding analogy with the classical harmonic chain 101
B.2 Displacement as function of time for coupled oscillators and tight-binding chains 103

C.1 Calculus of integral identities in the focalization under external perturbation 107

Chapter 1

On time reversal experiments and the questions they posed

Is it possible to turn time backwards? From immemorial times, this intriguing question has inspired the imagination of people, manifesting it through their artistic, philosophical and scientific expressions. In physics, the concept of time reversal leads to the *reversibility paradox* that puts in discussion an apparent conflict between the intrinsically reversible fundamental mechanical laws and the second law of thermodynamics, which describes the irreversible behavior of macroscopic systems.

We could say that this story begins in 1872, when Ludwig Boltzmann introduced his famous H-theorem and demonstrated from first principles how macroscopic systems composed by an astounding number of particles, *e.g.* a container with gas, arrive towards a stationary thermal equilibrium. Under the statistical mechanics perspective, this result states that the system experiences an increase of its entropy, and defines a concrete arrow of time in the dynamics. Immediately, a good friend of Boltzmann, the Austrian chemist Josef Loschmidt, objected that such mechanism of irreversibility cannot be deduced from the low-level time-symmetric equations of motion. Loschmidt proposed a *gedanken* experiment where a supernatural being, currently known as the *Loschmidt daemon* [Whe94, Kuh87], had the skill to revert simultaneously the velocities of all the particles and, consequently, the dynamics of the macroscopic gas.

In the seminal paper of Boltzmann, the time asymmetry slips into the theory through the *Stosszahlansatz* or molecular chaos hypothesis, where the velocities of two colliding particles in the gas are assumed to be uncorrelated. With the arrival of the chaos theory about a century later, it was possible to describe dynamics which are exponentially sensitive to small changes in initial conditions. The chaotic nature of the gas is omnipresent since a large amount of particles is involved. Hence, a general justification of the Boltzmann's assumption can be developed. Conversely, even slight imperfections in the Loschmidt daemon would degrade time reversibility. To avoid such imperfections, the overwhelmed daemon should possess a tremendous precision so that, even in theory, time reversal represents an impossible task.

The first experimental breakthrough into this problem had to wait until the second part

of the XXth century, when experiments in quantum mechanics gave the first realization of the Loschmidt daemon. This was the spin echo in nuclear magnetic resonance (NMR) [Hah50, BHa84]. Erwin Hahn realized that the time reversal could be achieved in systems of independent spins. In the experiment, spins which are initially aligned in a direction x in the plane perpendicular to the external field, precess with different Larmor frequencies $\Omega_i = \Omega_0 + \delta\Omega_i$ due to the local inhomogeneities of the magnetic field, δB_{zi}. As the spins spread in the plane, the net polarization intensity decreases steadily. At some moment t_R, a Loschmidt daemon acts in the form of a radiofrequency pulse that rotates each spin an angle of π around an axis y in the plane. As a consequence, each spin begins to "feel" as if its corresponding magnetic field had changed in sign. Thus, they rotate backwards and finally return to the original polarization forming an echo that starts spreading again (see Fig. 1.1a). Hahn noticed that this can be achieved by changing the sign of the Zeeman Hamiltonian

$$\mathcal{H}^i_{\text{Zeeman}} = -\gamma\left(B_z + \delta B_{zi}\right) S^z_i = -\hbar\left(\Omega_0 + \delta\Omega_i\right) S^z_i \underset{t=t_R}{\longrightarrow} -\mathcal{H}^i_{\text{Zeeman}}$$

associated to each spin i. The failure to obtain the initial polarization represents a quantifier of the processes beyond the daemon's control, such as spin-spin and spin-lattice interactions. Here, it is clear that the spin echo daemon only manages to revert a partial contribution to the total dynamics: that of the one-body interaction between each spin and the external field.

It took more than two decades for another experiment by Rhim, Pines and Waugh [RPW71] to implement the next nontrivial step: the time reversal of interacting spins. Their magic echo represents a more realistic realization of the Loschmidt proposal. As much as a gas can be idealized as particles jumping between nodes in a lattice, a quantum spin system also constitutes a lattice where neighbor spins "up" and "down" exchange according to their interaction. Based on a strategy similar to that of the spin echo, this procedure manages to revert the effective dipolar interaction between nearby spins (see Fig. 1.1b). Since it involves the collective energy, it achieves the time reversal of an actual many-body dynamics. However, the magic echo still showed a strong irreversibility which puzzled the community for more than two decades. In a classical model, one might imagine that the chaos present in many-body gas could play a relevant role, as it does in the Stosszahlansatz. However, there was no clear pathway for a theoretical interpretation along this concept in the extreme quantum regime of 1/2 spins. Further progress only appeared after the essence of the magic echo was distilled in the much simpler polarization echo technique developed in the group of R. Ernst [ZME92]. By using cross-polarization, a technique that uses the ^{13}C as a probe [MKB74], it was possible to inject and extract polarization from a single nuclei in a ^{1}H lattice. This enabled a manner to locally observe the forward and reverted evolutions of the polarization in the network. Indeed, the polarization is a quantity that can be described by a norm-conserving wave packet. In consequence, one might conceive a representation of the complex evolution of the polarization wave packet $|\psi_0\rangle$ as a result of a "complicated" (and perhaps chaotic or non-linear) Schrödinger equation.

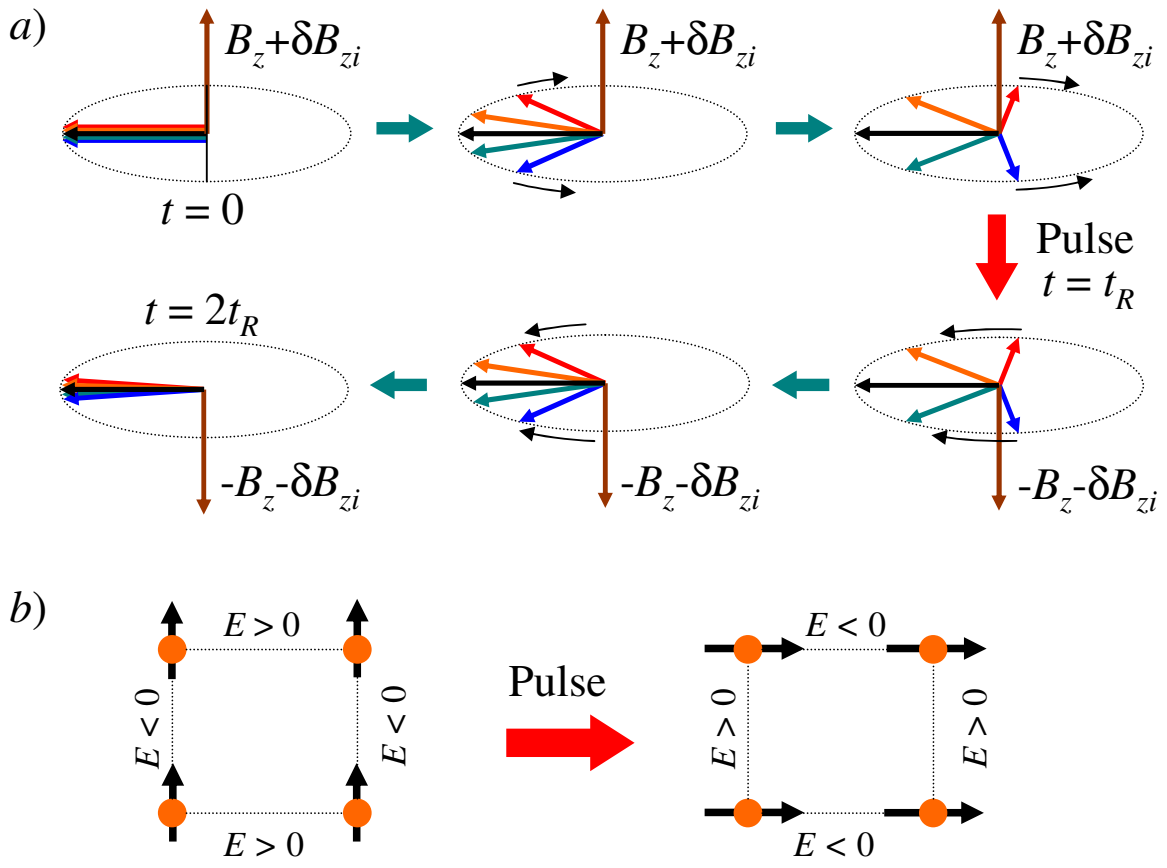

Figure 1.1: Time reversal echoes in NMR. a) Scheme of the Hahn's spin echo, the initially focused spins spreads in the rotation plane with different Larmor frequencies. After the inversion pulse at t_R, every spin feels the magnetic field as changed in sign and they focalize at $2t_R$. b) Magic echo for four coupled spins. They repel or attract depending the angle between their orientation and the internuclear vector. After the pulse, all the interactions change in sign.

The following experimental breakthrough was done at Córdoba in the group of Levstein and Pastawski [PLU95, UPL98, PLU00], by identifying a perturbation independent regime that gives a natural limit to the efficiency of the many-body Loschmidt daemon and relates it with the inherent chaos of the many-body dynamics. Here, the reversal in the dynamics of a many-spin system governed by a Hamiltonian $\mathcal{H}_0$ consists of a global action in the whole system. In a pictorial manner, this can be seen as a *hasty daemon*, who performs the instantaneous change in the sign of $\mathcal{H}_0$, at the price of doing it imperfectly. The resulting errors, such as imperfections in the inversion pulse or ignoring residual interactions, are summarized as a perturbation term Σ in the effective "backwards" Hamiltonian $-(\mathcal{H}_0 + \Sigma)$. Additionally, this term may also account for irreversible dissipative perturbations through a non-Hermitian component $\mathrm{Im}\,\Sigma = -\Gamma$. Hence, if the

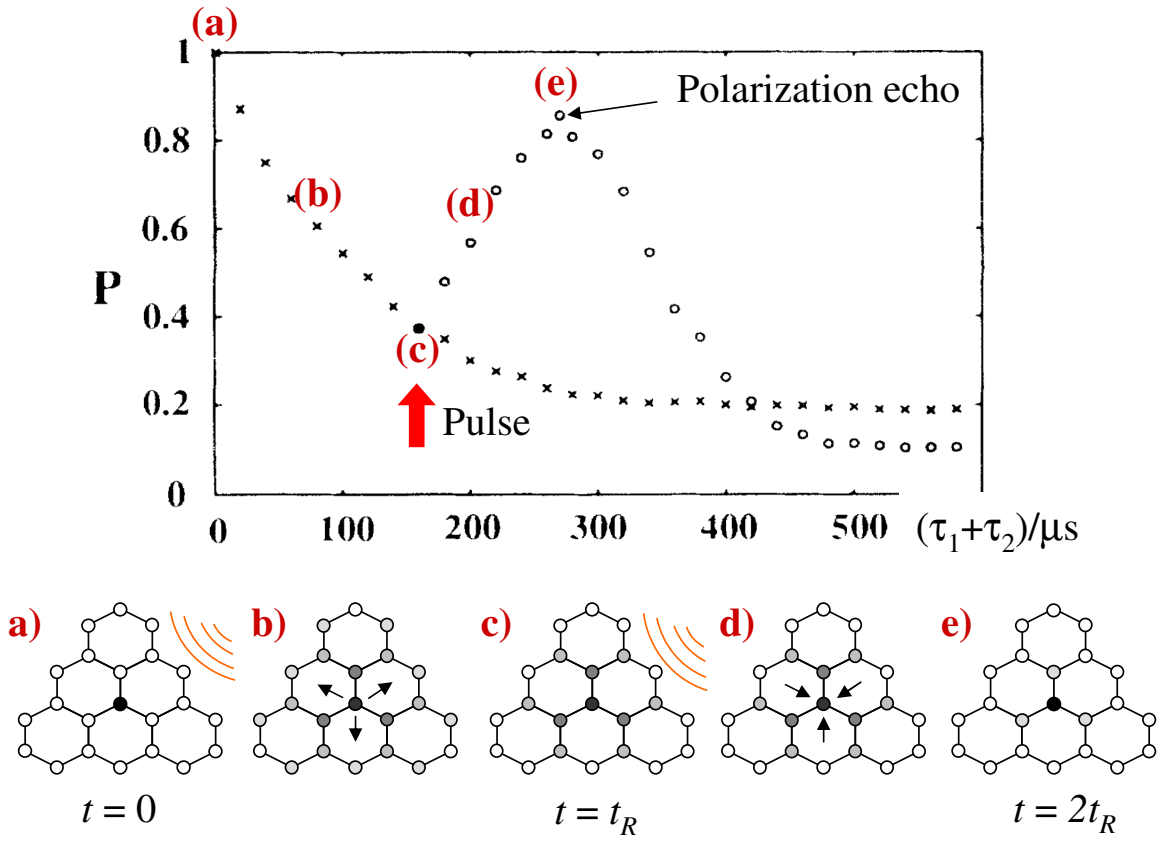

Figure 1.2: Top: Polarization as a function of time in the polarization echo experiment. Bottom: scheme of the time reversal operation in a many-body spin system. At the initial time, the local polarization is injected in the central spin and starts to decay through the chain. After the inversion pulse at time t_R, the dipolar interactions are changed in sign and the polarization refocuses in the center of the chain at time $2t_R$. Extracted from to Ref. [ZME92], © 1992 The American Physical Society.

reversal takes place at time t_R, the expected revival at time $2t_R$ is described through the return probability

$$M(2t_R) = \left|\langle\psi_0| \exp\left[-\mathrm{i}\left(-\mathcal{H}_0 - \Sigma\right)(2t_R - t_R)/\hbar\right] \exp\left[-\mathrm{i}\mathcal{H}_0 t_R/\hbar\right] |\psi_0\rangle\right|^2 , \tag{1.1}$$

as a measure of the *fidelity* of the time reversal process and for which the Córdoba group coined the name of *Loschmidt echo*[1] (LE). This definition, which also applies to classical systems, stresses the fact that in a more general context, the dynamical instability in quantum systems should be manifested as a sensitivity respect to perturbations in the dynamics. This contrasts with the classical chaos theory, where the instability is evidenced by perturbations in initial conditions. Indeed, previous studies using this last definition had suggested that Quantum Mechanics could not show dynamical chaos [CCG86].

[1]For a review on the early experiments of the LE see Ref. [PUL01].

In a seminal paper, Jalabert and Pastawski [JPa01] used a semiclassical description to show that the Loschmidt echo defined above presents a perturbation independent regime controlled by the Lyapunov exponent of the corresponding classical system. This semiclassical approximation describes a wave function evolving from an initial point, as a superposition of waves riding over the classical trajectories (or rays) connecting the initial and final points in the alloted time. The instability of the classical trajectories, which is an intrinsic property of $\mathcal{H}_0$, manifests itself when the evolution of the wave function is perturbed. In this context, chaos plays a limiting role in the reconstruction of the initial state. Numerical evidence of this regime was observed both in open and closed chaotic systems [CPW02, WVP02]. Since then, an increasing number of analytical and experimental work tackled the evaluation of the LE for quite different systems and perturbations.

Simultaneously, and for something more than a decade, another kind of Loschmidt daemon was being developed in the Laboratoire Ondes et Acoustique in Paris. There, the group of Mathias Fink designed the time reversal mirror (TRM) [DRF95, Fin99, Fin01], a procedure that attempted to reverse acoustic waves. This technique was shown to be quite accurate in the focalization of ultrasound propagating through heterogeneous media. In its simplest form, the TRM procedure can be summarized as follows (see Fig. 1.3):

- The propagation of a pulse inside certain working region, called the *cavity*, is detected as it arrives to an array of transducers at the boundaries that surrounds it. Their registries are recorded until a time t_R at which the excitation has already escaped to the environment and the signal has become negligible.

- Afterwards, each transducer, which can act alternatively as a microphone or loudspeaker, re-emits in the time reversed sequence producing an extra signal controlled by the "volume" knob. The experiments show that these waves follow the inverse dynamics, tending to reconstruct the original pulse at the time $t = 2t_R$.

When comparing standard waveguides with systems with strong scattering, they realized these last ones yield much better focalizations [Fin97]. This counter intuitive result was obtained in several experiments which evidence that disorder is the responsible for the robustness of time reversal. In fact, TRM experiments on a closed chaotic cavity found that even the use of a single transducer and a limited interval of the registration is enough to perform the time reversal with an acceptable level of quality [DFi97] (see Fig. 1.4). Other realizations have shown to be particularly stable in systems with multiple scattering mechanisms [TDF01], where the perturbation acts either locally (by removing scatterers) or globally (by changing the temperature). The stability of the focusing against the inhomogeneities and the partial use of available information enabled various applications: in medical physics [FMT03], it seeks to focalize energy to destroy kidney stones and tumors; in telecommunications [LRT04, HSt04], where the transmitted signal encodes information not detected anywhere else; and in oceanography [EAH02], where the attenuation of this signal encodes the fluctuations of the media.

It is clear that TRM experiments introduce an alternative way to obtain time reversal. Since the procedure involves a "persistent" action performed locally at the periphery of

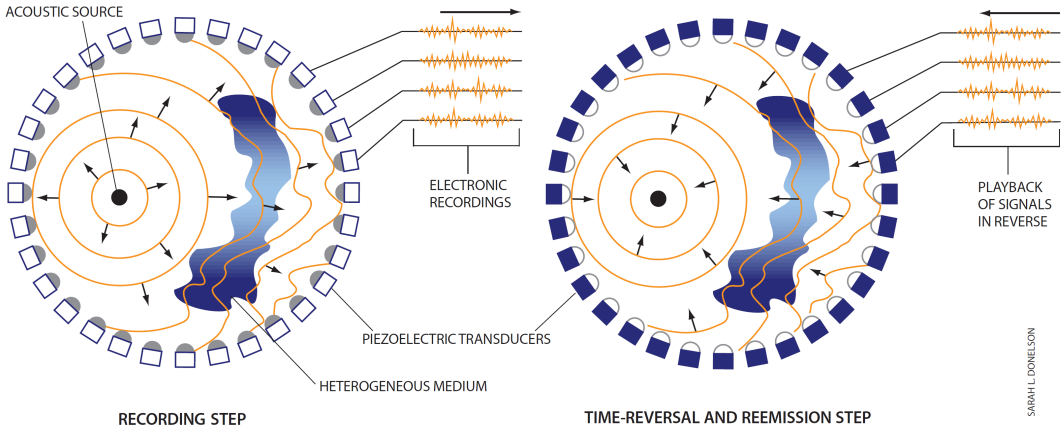

Figure 1.3: Scheme of the TRM procedure. In the recording step (left), the transducers act like microphones (white squares) and during the emission (right), they act as loudspeakers (blue squares). Extracted from Ref. [Fin99], © 1999 Scientific American, Inc.

the cavity, *i.e.* a low amplitude injection of wave excitation for a long period of time, we like to call it the *stubborn daemon*.

In spite of the impressive success of the TRM procedure, it is legitimate to recognize that a number of intriguing questions remain unanswered. A first question that we would like to address is: Why does it work? This is by no means obvious since the theoretical prescription for time reversal, *i.e.* one must ensure that the signal and its normal derivative at every point of the frontier reproduces the exact outcoming signal, does not seem to be satisfied. Indeed, the experimental procedure only "injects" a signal equivalent to that detected which sums up to the preexisting excitation. Besides, there is no control of the normal derivative. Assuming that an exact time reversal could be implemented, a natural question arises: Does this TRM prescription holds in Quantum Mechanics? Indeed, Quantum Dynamics follows a first order derivative in time (*i.e.* it is naturally dispersive), while the sound equation is second order. Therefore, it is not obvious that the same procedure would hold for both cases. Finally, considering the different rôle of chaos in the hasty daemon and its "relative", the stubborn daemon, one should also venture into a more fundamental question: Why does the disorder and chaos increase the stability in this form of time reversal? These are the main questions addressed in this thesis. In summary, we develop a formal theoretical description of the exact time reversal mirror and then we analyze its stability against different types of errors.

At the moment we started our work, there was no formal theory regarding the validity of the TRM protocol as implemented experimentally, even in the ideal case where no errors occur during the recording and emission steps. In order to obtain such a theory, we first focus on the concept of perfect reversal in a quantum mechanical system. Intuitively, it is clear that wave dynamics provides a common starting point in the analysis of both classical

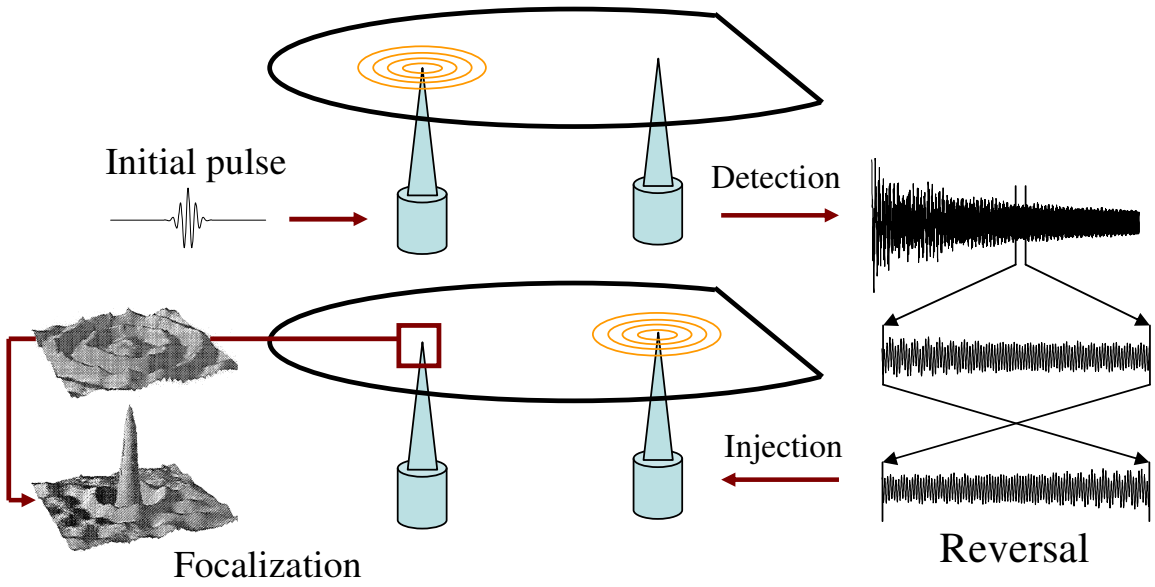

Figure 1.4: Scheme of the TRM procedure in a close chaotic cavity. Here, a single transducer and a portion of the signal are enough to perform the time reversal. Extracted from Ref. [Fin99], © 1999 Scientific American, Inc.

and quantum procedures. In practice, such study requires addressing an issue usually disregarded: the use of the Schrödinger equation (SE) with a time dependent source. This interest is not merely academic since it appears in many experimental situations. One that has particular interest for the NMR Córdoba group is the gradual injection of coherent polarization in a system of abundant nuclei through an NMR cross-polarization transfer [MKB74]. At the front line of spectroscopical techniques is the creation of a coherent excited state [WLE93, Zew00] through particular sequences of laser pulses at slow pumping rates. Finally, even more conventional experiments in AC electrical conductivity involve electrodes that could be seen as fluctuating sources of waves [Pas92].

In **Chapter 2**, we address the issue of a local time dependent injection of quantum waves. Firstly, we solve the inverse scattering problem, *i.e.* we deduce the local injection at the periphery of the cavity required to obtain the target function. The key to obtain this solution was to use the Schrödinger equation in a discrete form as a tight-binding system. The solution to the injection problem immediately allows us to design a novel time reversal procedure provided that the original excitation is initially outside the cavity. As expected, this requires to correct the TRM prescription by incorporating a filter, in this case a factor in the energy/frequency representation that, taking care of the feedback effects, ensures the exact time reversal. We will refer to this procedure as *perfect inverse filter* (PIF) [PDC07]. This study also quantifies the conditions for a perfect reversal. In particular, we assume that the signal originates externally and one has access to detect and record its entrance to the cavity and its further escape. As a possible implementation

of the PIF, we designed the *quantum bazooka* as an improved version of the acoustic bazooka proposed by Fink [Kup06]: when a waveguide injects a well defined wave packet into a resonant or chaotic cavity, it is reflected as a (typically noisy) persistent signal. The time reversed counterpart allows to store in the cavity the weak signal injected through a long period of time until it emerges as a burst of high power excitation.

In a second part of the chapter, we address the experimental cases where the original excitation is initially inside the cavity. This means that one can clearly differenciate between an excitation period and an escape period. This leads to a PIF correction that contains an important result not easily visualized in the previous situation: the filter does not depend on the internal scattering, but only on the group velocities of the various propagating modes outside the cavity. We test the quality of reversal in both the TRM and PIF procedures for two different cases. One is a cavity connected to a single channel waveguide as in a quantum bazooka, where the injection/detection is performed by a single transducer at the waveguide. The other is a cavity connected to a multichannel system. Here, the local excitation placed in the cavity is detected by several transducers as it escapes away.

In **Chapter 3**, we develop a PIF prescription for classical waves. We start describing the propagation of acoustic waves in continuous media through its analogy with a model of coupled harmonic oscillators. In this model, the propagators describe the displacements of the oscillators with respect to their equilibrium positions. The excitations arise as the response to either the usual impulsive force or a "displacive force", which we define as a combination of kicks that change the oscillator position without affecting its impulse. Each one of these define the Green's functions describing respectively the position-momentum and the position-position correlations. The analogy between classical and quantum propagators allows to derive the corresponding PIF prescription in the classical domain. As in the quantum case, we observe that the correction imposed by the PIF prescription also depends only on the group velocity of the outgoing waves. In classical systems, in particular where the dispersion relation in the outer region is linear, the TRM becomes exact. As an example of implementation of the PIF procedure, we consider a Helmholtz resonator coupled to a periodic waveguide where the dispersion relation is not linear [CDP07, CPa10]. To compute the displacements and velocities of the coupled oscillators within a fully time reversible algorithm, we develop the Pair Partitioning method [CPa07]. This also allows to get rid of finite size effects through a finite region of oscillators that includes additional "frictional" forces in the Hamiltonian.

Having a formal theory of an ideal TRM, we are able to give a first step to assess the stability of the procedure. To tackle this question, we address in **Chapter 4** the experiment shown in Fig. 1.4, where the TRM is implemented in a closed chaotic cavity with a single transducer during a finite emission period [DFi97]. In this chapter, we introduce the semiclassical approximation for the TRM [CJP08, CPJ09] and use it to quantify the focalization amplitude. The ergodic hypothesis appears as essential in our analysis, *i.e.* that there are infinite ways to reach any point in any given time. Under this assumption we find, in agreement with the acoustic experiments, that the focusing amplitude scales linearly with both the number of transducers and the width of the

emission window. Furthermore, the focusing amplitude results inversely proportional to the total area (volume) of the cavity.

In **Chapter 5** we seek to evaluate how dissipation and errors affect the focalization. First, we model a dissipative system by considering a small opening in the cavity (a non-Hermitian perturbation). Here, it is convenient to write the TRM focusing in terms of the nonescaping probability, *i.e.* the overlap between forward and backward propagations. In addition to the usual scaling observed in chapter 4, this leads to a focalization that decays exponentially with the escape rate Γ given by the opening. In a second part of the chapter, we analyze the TRM in systems with an Hermitian external perturbation acting only at the emission stage. Here, the focalization is expressed in terms of the Loschmidt echo amplitude. In fact, we follow the approximative scheme of the LE studies and find two decay regimes that depend on the strength of the perturbation: when a small emission window is used (as compared to the characteristic decay time $\tilde{\tau}$), we obtain a Fermi golden rule (FGR) describing typical experimental cases. In turn, when the final registration time is larger than $\tilde{\tau}$, the focalization saturates and only depends on the initial registration time. Among them, the FGR yields an important result concerning the stability of the TRM: the attenuation in the focalization decreases when the chaos of the system is increased (the more scattering, the better the focalization is).

Finally, in **Chapter 6**, we give the global conclusions and discuss some of the possible future perspectives of time reversal focusing that emerge from our work. Among them, we want to remark that, by using the new analytical tools we have developed to process and improve the focalization, new possibilities open ranging from non-invasive tumor hyperthermal surgery to directed and naturaly encoded telecommunications.

Chapter 2

Towards the design of a perfect time reversal mirror

As pointed out previously, the focalization of acoustic, elastic and electromagnetic waves has been successfully achieved through the time reversal mirror technique (TRM). Although this procedure enabled many experimental realizations with promising applications, which range from the destruction of kidney stones to high security communication, a complete theory for the TRM has not been fully developed yet and some puzzling questions regarding the limitations of the technique remain unanswered. In general, there is no answer [All69, BEM01] to the *inverse time problem*: What wave function must be injected to obtain a desired output? In this chapter we solve this problem for a reasonably general case and use this solution to implement a protocol for a perfect quantum time reversal experiment. Such solution was performed through a novel prescription called the perfect inverse filter (PIF), that reaches the exact time reversal in the dynamics inside a working region (the cavity), which is surrounded by an array of transducers [CFi92]. The comparison between both TRM and PIF methods gives a precise idea of how faithfully the TRM recovers the original state and serves us to identify those cases where such reversal departs from the ideal one.

Throughout the chapter, we work under the conditions for a perfect reversal: the complete wave amplitude is detected as it crosses the frontiers of the cavity and no absorption or localization mechanisms are present. These yield a natural separation of the system in two portions: the cavity, where one attempts to reverse the dynamics; and the outer region, where the excitations finally escape (see Fig. 2.1). The application of the PIF strictly depends on where the original excitation is initially placed, being necessary to consider two different situations:

- The *external* PIF: when the source that creates the initial excitation is placed outside the cavity, the registered signal consist of a well-defined wave packet which initially travels towards the cavity. Once the wave packet crosses the frontier of transducers, it spreads by bouncing on the walls or inhomogeneities and a low amplitude signal remains emerging towards the outside for a long period. Its reversal

could be imagined as an *acoustic bazooka* device, where the persistent emission of signal at the level of noise produces an excitation that accumulates in the cavity and finally escapes towards the outside as a concentrated burst of energy.

- The *internal* PIF: when the source is placed inside the cavity, the signal is detected as the excitation decays. This is also the case of a well resolved incoming wave that enters into the cavity and is detected as escapes towards the outside. In these situations, the entrance is not detected and we deduce the complete propagation in terms of the outgoing signal and the response on the transducer.

Exploiting the close correspondence between the Schrödinger and the classical wave equations, we introduce the PIF within a quantum formalism where the corresponding propagators are well known. Besides, as we shall see in Chapter 3, the prescription remains valid to describe sound propagation with identical results. Since the corresponding procedures deal with the general properties of the propagators, the discrete Schrödinger equation is a well-suited formalism describing, in a comprehensive way, the separation between the cavity and the outer region, required for the formal solution to the inverse time problem (*i.e.* include the signal and its normal derivative at the boundaries of the cavity). For this purpose, a single transducer is enough to exhibit the physical idea of the procedure. The formal derivation for several transducers in multi-dimensional systems follows the same arguments and is presented for both the external and internal cases.

We start with the study of the external PIF prescription and then we evaluate the obtained results in the quantum version of the acoustic bazooka. In the second part, we introduce the internal PIF for a single transducer and implement the procedure in a quantum bazooka configuration. As an example of PIF with several transducers, we solve the time reversal in a multichannel system with a local excitation placed inside the cavity. In all these cases we compare the PIF and TRM procedures numerically.

2.1 Solution of the inverse time problem

To start, we resort to the Schrödinger equation in a one-dimensional system describing the probability amplitude $\psi(x)$ to find a particle in a given position x

$$\left[-\frac{\hbar^2}{2m}\nabla_x^2 + U(x)\right]\psi(x) = \varepsilon\psi(x). \tag{2.1}$$

We can discretize this equation obtaining a finite differences approach

$$-\frac{\hbar^2}{2m}\frac{\dfrac{\psi(x+a)-\psi(x)}{a} - \dfrac{\psi(x)-\psi(x-a)}{a}}{a} + U(x)\psi(x) = \varepsilon\psi(x), \tag{2.2}$$

where a is the lattice constant, *i.e.* the minimum distance between two possible positions. We describe this discrete Schrödinger equation through the *tight-binding* Hamiltonian

[PMe01]

$$H = \sum_{j\in A\cup B} E_j \hat{c}_j^+ \hat{c}_j + \sum_{j\in A\cup B} (V_{j+1,j}\hat{c}_{j+1}^+ \hat{c}_j + \text{h.c.}), \tag{2.3}$$

where $\hat{c}_j^+$ and $\hat{c}_j$ are the standard creation and annihilation operators for a particle at the coordinate $x_j = ja$. The site index j runs over the whole system, composed by the cavity A where the control of the wave amplitude is attempted, and the outer region B, *i.e.* the complementary infinite subspace of scattering states where the excitations escape. In the tight-binding model, the kinetic energy gives the first-neighbor hopping term $V_{i,j} = -V\delta_{i\pm1,j}$ with $V = \hbar^2/2ma^2$, whereas the potential energy $U(x_j)$ fixes the "site energy" $E_j = U(x_j) + 2V$. Therefore, the probability amplitude at site x_j, denoted as $\psi_j(\varepsilon)$, is obtained through the equations

$$(\varepsilon - E_j)\psi_j(\varepsilon) - V_{j,j-1}\psi_{j-1}(\varepsilon) - V_{j,j+1}\psi_{j+1}(\varepsilon) = 0, \tag{2.4}$$

and the Schrödinger equation takes the matrix form

$$(\varepsilon\mathbb{I} - \mathbb{H})\,|\psi(\varepsilon)\rangle = 0, \tag{2.5}$$

$$\begin{pmatrix} \ddots & & & & \\ & \varepsilon - E_{j-1} & -V_{j-1,j} & 0 & \\ & -V_{j,j-1} & \varepsilon - E_j & -V_{j,j+1} & \\ & 0 & -V_{j+1,j} & \varepsilon - E_{j+1} & \\ & & & & \ddots \end{pmatrix} \begin{pmatrix} \vdots \\ \psi_{j-1}(\varepsilon) \\ \psi_j(\varepsilon) \\ \psi_{j+1}(\varepsilon) \\ \vdots \end{pmatrix} = \begin{pmatrix} \vdots \\ 0 \\ 0 \\ 0 \\ \vdots \end{pmatrix}. \tag{2.6}$$

We consider an initial wave packet whose components $\psi_n(0)$ are located in the outer region B and travels towards the cavity A. As the wave packet crosses the frontier delimited by the transducers, the detected signal in the s-transducer takes the usual expression

$$\psi_s(t) = \sum_{n\in B} \mathrm{i}\hbar G_{s,n}^R(t)\psi_n(0), \qquad t \geq 0. \tag{2.7}$$

Here, the time retarded propagator

$$\mathrm{i}\hbar\mathbb{G}^R(t) = \exp\left(-\frac{\mathrm{i}}{\hbar}\mathbb{H}t\right), \qquad t \geq 0, \tag{2.8}$$

corresponds to the unitary time evolution operator where its (s,n) element is the temporal response at the s-site due to a Dirac delta excitation $\delta(t)$ originated in the n-site and satisfies

$$\mathrm{i}\hbar\frac{\partial}{\partial t}G_{s,n}^R(t) - \sum_{i\in A\cup B} H_{s,i}G_{i,n}^R(t) = \delta_{s,n}\delta(t), \tag{2.9}$$

with $\delta_{s,n}$ the Kronecker delta. We emphasize the term *retarded* propagator since the involved response is a consequence of $\delta(t)$, contrary to the *advanced* one that is defined for times $t < 0$ before such instantaneous excitation. For a more compact notation, we

omit the R superscript of such retarded propagators since the advanced ones will be not used henceforth. Its Fourier transform gives the representation in the energy domain that is usually known as the Green's function

$$\mathbb{G}(\varepsilon) = (\varepsilon\mathbb{I} - \mathbb{H})^{-1}. \tag{2.10}$$

In this representation,

$$\begin{aligned} \psi_s(t) &= \int_{-\infty}^{\infty} \psi_s(\varepsilon) e^{-\mathrm{i}\varepsilon t/\hbar} \frac{\mathrm{d}\varepsilon}{2\pi\hbar}, & (2.11)\\ &= \mathrm{i}\hbar \sum_{n\in B} \int_{-\infty}^{\infty} G_{s,n}(\varepsilon)\psi_n(0) e^{-\mathrm{i}\varepsilon t/\hbar} \frac{\mathrm{d}\varepsilon}{2\pi\hbar}. & (2.12) \end{aligned}$$

At this point, we separate the space in the portions A and B, regarding that the A sub-space is the region where one intends to control the wave function. Formally, the total Hamiltonian can be written as

$$\mathbb{H} = \mathbb{H}_A + \mathbb{H}_B + \mathbb{V}_{AB} = \mathbb{H}_0 + \mathbb{V}_{AB}, \tag{2.13}$$

where the hopping matrix $\mathbb{V}_{AB}$ links the transducers with the edge sites of A. For simplicity, we consider a semi-infinite system where the two regions are separated by a single transducer (see Fig. 2.1).

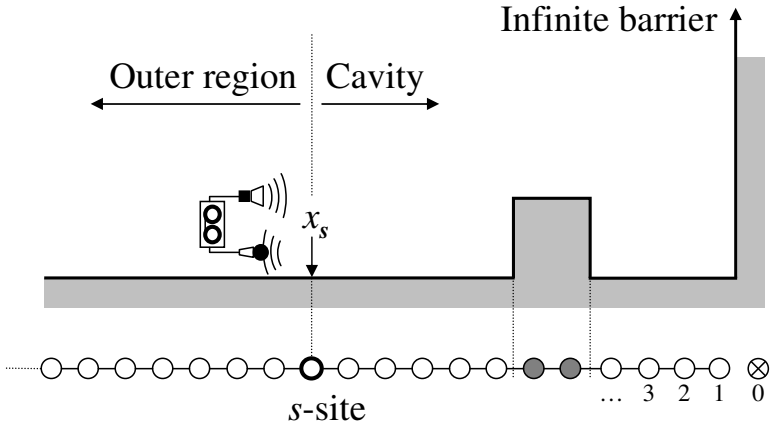

Figure 2.1: Top: potential profile for a scattering barrier located inside the cavity delimited by the transducer at x_s. Bottom: tight-binding model for the considered system.

By labeling the internal sites as m with $m < s \leq n$, and $n \in B$, it is possible to relate the internal and external sites by considering $\mathbb{V}_{AB}$ perturbatively. In this sense,

$$\begin{aligned} \mathbb{G}(\varepsilon) &= (\varepsilon\mathbb{I} - \mathbb{H}_0 - \mathbb{V}_{AB})^{-1}, & (2.14)\\ &= \left(\mathbb{I} - \mathbb{G}^{(0)}(\varepsilon)\mathbb{V}_{AB}\right)^{-1} \mathbb{G}^{(0)}(\varepsilon), & (2.15) \end{aligned}$$

where $\mathbb{G}^{(0)}(\varepsilon) = (\varepsilon\mathbb{I} - \mathbb{H}_0)^{-1}$ is the *unperturbed* Green's function matrix that solves Eq. (2.10) for $\mathbb{V}_{AB} = 0$. Expanding the first term of Eq. (2.15) as a geometric series, one obtains

$$\mathbb{G}(\varepsilon) = \mathbb{G}^{(0)}(\varepsilon) + \mathbb{G}^{(0)}(\varepsilon)\mathbb{V}_{AB}\mathbb{G}^{(0)}(\varepsilon) + \mathbb{G}^{(0)}(\varepsilon)\mathbb{V}_{AB}\mathbb{G}^{(0)}(\varepsilon)\mathbb{V}_{AB}\mathbb{G}^{(0)}(\varepsilon) + \ldots, \tag{2.16}$$

that can be represented recursively as the Dyson equation [Eco06]

$$\mathbb{G}(\varepsilon) = \mathbb{G}^{(0)}(\varepsilon) + \mathbb{G}^{(0)}(\varepsilon)\mathbb{V}_{AB}\mathbb{G}(\varepsilon), \tag{2.17}$$

and whose (m, n) element writes

$$G_{m,n}(\varepsilon) = G^{(0)}_{m,n}(\varepsilon) + \sum_{l,l'} G^{(0)}_{m,l}(\varepsilon)V_{l,l'}G_{l',n}(\varepsilon). \tag{2.18}$$

Since the separation between both spaces is given through the transducer at the s-site, the unperturbed Green's functions $G^{(0)}_{j,i}(\varepsilon)$ defined by $V_{s-1,s} = V_{s,s-1} = 0$ are exact zeros. Hence, Eq. (2.18) writes

$$G_{m,n}(\varepsilon) = G^{(0)}_{m,s-1}(\varepsilon)V_{s-1,s}G_{s,n}(\varepsilon). \tag{2.19}$$

Furthermore, the Dyson equation remains valid if we take the Green's function between the m-site and the transducer yielding

$$G_{m,s}(\varepsilon) = G^{(0)}_{m,s-1}(\varepsilon)V_{s-1,s}G_{s,s}(\varepsilon), \tag{2.20}$$

and the wave function for sites $m \leq s$ writes

$$\psi_m(t) = \mathrm{i}\hbar \sum_{n\in B} \int_{-\infty}^{\infty} G_{m,s}(\varepsilon)\frac{G_{s,n}(\varepsilon)}{G_{s,s}(\varepsilon)}\psi_n(0)e^{-\mathrm{i}\varepsilon t/\hbar}\frac{\mathrm{d}\varepsilon}{2\pi\hbar}, \tag{2.21}$$

$$= \mathrm{i}\hbar \int_{-\infty}^{\infty} G_{m,s}(\varepsilon)\frac{1}{\mathrm{i}\hbar G_{s,s}(\varepsilon)} \times \sum_{n\in B} \left[\mathrm{i}\hbar G_{s,n}(\varepsilon)\psi_n(0)\right] e^{-\mathrm{i}\varepsilon t/\hbar}\frac{\mathrm{d}\varepsilon}{2\pi\hbar}. \tag{2.22}$$

The sum within square brackets can be identified from Eq. (2.12) as the energy representation of the detected signal in the transducer, *i.e.*

$$\psi_m(t) = \mathrm{i}\hbar \int_{-\infty}^{\infty} G_{m,s}(\varepsilon)\frac{\psi_s(\varepsilon)}{\mathrm{i}\hbar G_{s,s}(\varepsilon)}e^{-\mathrm{i}\varepsilon t/\hbar}\frac{\mathrm{d}\varepsilon}{2\pi\hbar}. \tag{2.23}$$

This is the wave function inside the cavity that results from

$$\chi_s(\varepsilon) = \frac{1}{\mathrm{i}\hbar G_{s,s}(\varepsilon)}\psi_s(\varepsilon), \tag{2.24}$$

i.e. the Fourier transform of the signal that must be injected at each instant in order to obtain the *target function* provided that no amplitude existed in A at the initial time. This result only relies on the partition in complementary subspaces connected by a single Hermitian operator $\mathbb{V}_{AB}$. The key feature allowing this simple solution was the representation of the Schrödinger equation in a discrete basis. This enabled a natural separation into complementary subspaces that were re-connected through the Dyson equation.

2.2 Exact reversal through the Perfect Inverse Filter

Now that we know how to control the dynamics inside the cavity, an injection achieving the temporal reversion is possible. Here, we accounts the inverse propagation of the detected signal, which is obtained as $\psi_s^{\text{rev}}(t) = \psi_s^*(2t_R - t)$, for times $t_R \leq t \leq 2t_R$. In addition to the inversion of the temporal argument $t \longrightarrow 2t_R - t$, the complex conjugate operation represents the inversion in the momentum at the site of the transducer and is required for the time reversal. In this case, the energy representation of the reversed signal is performed as

$$\psi_s^{\text{rev}}(\varepsilon) = \int_{-\infty}^{\infty} \psi_s^*(2t_R - t) e^{\mathrm{i}\varepsilon t/\hbar} \mathrm{d}t \simeq \int_{t_R}^{2t_R} \psi_s^*(2t_R - t) e^{\mathrm{i}\varepsilon t/\hbar} \mathrm{d}t \tag{2.25}$$

$$= e^{\mathrm{i}\varepsilon 2t_R/\hbar} \left[\int_0^{t_R} \psi_s(t) e^{\mathrm{i}\varepsilon t/\hbar} \mathrm{d}t \right]^* = e^{\mathrm{i}\varepsilon 2t_R/\hbar} \psi_s^*(\varepsilon), \tag{2.26}$$

where the additional phase $e^{\mathrm{i}\varepsilon 2t_R/\hbar}$ accounts for the displacement in time of the signal. For this target function, the PIF prescription results

$$\chi_s^{\text{PIF}}(\varepsilon) = \frac{e^{\mathrm{i}\varepsilon 2t_R/\hbar}}{\mathrm{i}\hbar G_{s,s}(\varepsilon)} \psi_s^*(\varepsilon). \tag{2.27}$$

This is the injection that performs the exact time reversal in the dynamics inside the cavity, provided that there is no exctitations neither at the begining nor at the end of the detection. Besides, the filter can be seen as that one applies on the TRM injection

$$\chi_s^{\text{TRM}}(\varepsilon) = e^{\mathrm{i}\varepsilon 2t_R/\hbar} \frac{2V}{\hbar} \psi_s^*(\varepsilon), \tag{2.28}$$

and consists of the inverse of the Green's function at the site of the transducer. This compensates the feedback produced by the internal scattering of both the cavity and the outer region.

2.2.1 Multi-dimensional external PIF

Here we include the generalization for the external PIF in multi-dimensional systems with several transducers. As before, the system is separated in two sub-spaces: the cavity A with N_A sites $\mathbf{a}_i$ and the outer region B, being this last an infinite space of sites $\mathbf{b}_i$. The initial wave packet that starts in the outer region can be expanded in terms of the real basis states as

$$|\psi_B(0)\rangle = \sum_{n=1}^{N_B} \langle \mathbf{b}_n \, |\psi_B(0)\rangle \, |\mathbf{b}_n\rangle = \sum_{n=1}^{N_B} \psi_{\mathbf{b}_n}(0) \, |\mathbf{b}_n\rangle \,, \tag{2.29}$$

with $N_B \to \infty$. The arriving excitation is detected at the array of N_S transducers located in the positions $\mathbf{s}_i$ according to

$$|\psi_S(t)\rangle = \begin{pmatrix} \psi_{\mathbf{s}_1}(t) \\ \psi_{\mathbf{s}_2}(t) \\ \vdots \\ \psi_{\mathbf{s}_{N_S}}(t) \end{pmatrix} = \mathrm{i}\hbar \mathbb{G}_{S,B}(t)\,|\psi_B(0)\rangle\,, \tag{2.30}$$

where $\mathbb{G}_{S,B}(t)$ is the $N_S \times N_B$ matrix of propagators that link the outer sites with the array of transducers and whose elements write $[\mathbb{G}_{S,B}(t)]_{i,j} = G_{\mathbf{s}_i,\mathbf{b}_j}(t)$. Hence, the time reversal of the detected signal is

$$|\psi_S^{\mathrm{rev}}(t)\rangle = -\mathrm{i}\hbar \mathbb{G}^*_{S,B}(2t_R - t)\,|\psi_B^*(0)\rangle\,, \qquad t_R \leq t \leq 2t_R. \tag{2.31}$$

In the energy representation, the Green's functions matrix maintains the same recursive properties as before and the Dyson equation connecting internal and external sites is

$$\mathbb{G}_{A,B}(\varepsilon) = \mathbb{G}^{(0)}_{A,B}(\varepsilon) + \mathbb{G}^{(0)}_{A,\tilde{A}}(\varepsilon)\mathbb{V}_{\tilde{A},S}\mathbb{G}_{S,B}(\varepsilon), \tag{2.32}$$

where the hopping matrix $\mathbb{V}_{\tilde{A},S}$ links the transducers with the boundaries $\tilde{A} \subset A$ of the cavity. Again, $\mathbb{G}^{(0)}(\varepsilon)$ accounts for the unperturbed Green's functions with $\mathbb{V}_{\tilde{A},S} = 0$ and is exactly a zero matrix. We skip the ε dependence symbol for a more compact notation henceforth. Using of the Dyson equation to evaluate the response between the transducers and the cavity one obtains

$$\mathbb{G}_{A,S} = \mathbb{G}^{(0)}_{A,\tilde{A}}\mathbb{V}_{\tilde{A},S}\mathbb{G}_{S,S}, \tag{2.33}$$

and therefore

$$\mathbb{G}_{A,B} = \mathbb{G}_{A,S}\mathbb{G}^{-1}_{S,S}\mathbb{G}_{S,B}. \tag{2.34}$$

Then, the signal in the cavity that follows from the emission at the transducers can be deduced according to Eqs. (2.21) and (2.22)

$$|\psi_A\rangle = \mathbb{G}_{A,S}\mathbb{G}^{-1}_{S,S}\,|\psi_S\rangle\,, \tag{2.35}$$

and for the time reversed injection we use Eq. (2.26) to obtain

$$|\psi_A^{\mathrm{rev}}\rangle = e^{\mathrm{i}\varepsilon 2t_R/\hbar}\mathbb{G}_{A,S}\mathbb{G}^{-1}_{S,S}\,|\psi_S^*\rangle\,, \tag{2.36}$$

with $|\psi_S^*\rangle_i = \psi^*_{\mathbf{s}_i}(\varepsilon)$. Then, PIF injection for several transducers generalizes as

$$\left|\chi_S^{\mathrm{PIF}}\right\rangle = \frac{e^{\mathrm{i}\varepsilon 2t_R/\hbar}}{\mathrm{i}\hbar}\mathbb{G}^{-1}_{S,S}\,|\psi_S^*\rangle\,, \tag{2.37}$$

maintaining its original form according to Eq. (2.27). The N_S^2 elements of $\mathbb{G}_{S,S}(t)$ describe the response at the $\mathbf{s}_i$-transducer to a Dirac delta pulse emitted in the $\mathbf{s}_j$-transducer. According to the related experiments on the acoustic TRM, this operation is considered as noninvasive since all these values are measured at the cavity frontiers.

2.2.2 Time reversal via injection: the Quantum Bazooka

In the following example, we use the previous result in a *gedanken* scheme that achieves a perfect time reversal of an arbitrary wave packet by assuming that a persistent non-invasive injection and detection of waves at a single point is possible. We illustrate this by considering an incoming Gaussian wave packet in a semi-infinite space bounded by an infinite barrier at $x = 0$ which, together with a scattering barrier, define a reverberant region (see Fig. 2.1). At the point s, located to the left of the barrier, we alternate the use of an injector and detector of wave function (probability and phase). This set-up is a simplified variation of the acoustic bazooka devised by Fink and collaborators. However, instead of using the TRM, we proceed as follows:

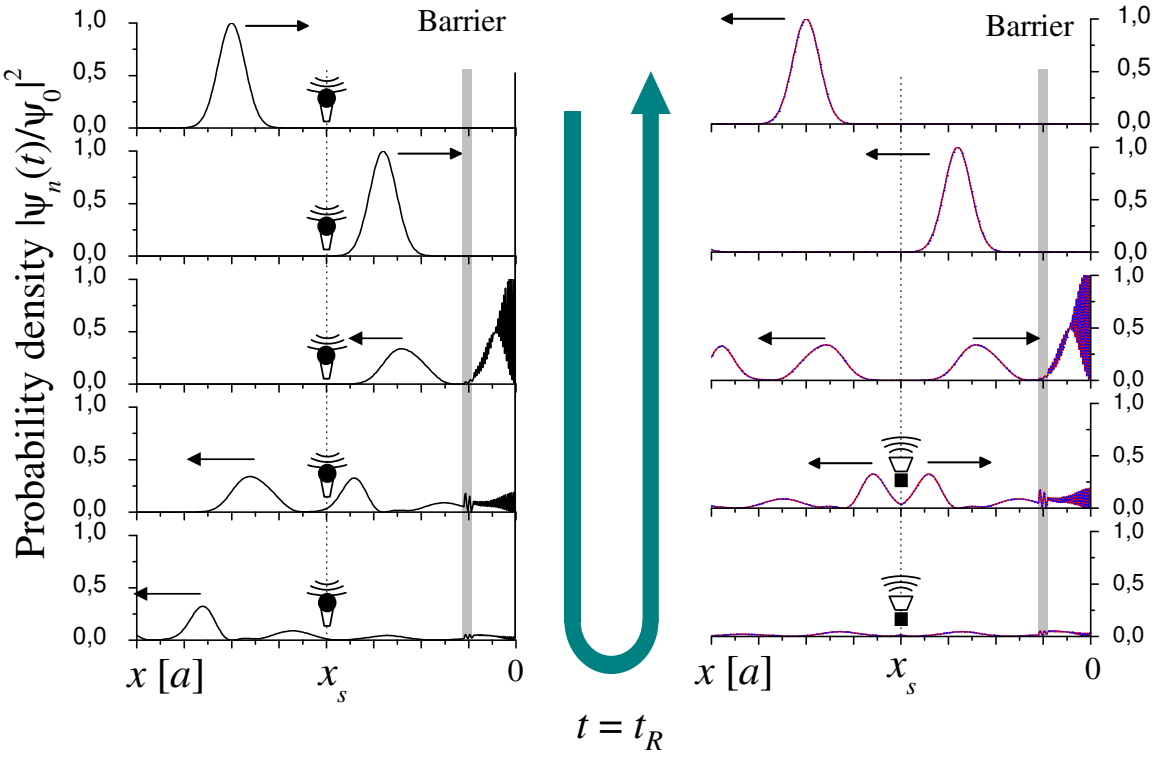

Figure 2.2: Rescaled probability density $|\psi_n(t)/\psi_0|^2$ (in the cavity and the outer region) for different times. The left panel shows the forward evolution between 0 and $t_1 < t_R$. The backward evolution is shown in the right panel between $2t_R - t_1$ and $2t_R$. The blue dotted line is the result of a PIF injection, while the solid red (superimposed) is obtained by injecting only the time-reversed wave recorded at x_s during the forward evolution. The initial Gaussian wave packet, which is centered at $x_s - 100a$, has $\sigma/a = 10$ and $k_0 a = \pi/2$.

1. By injecting a Dirac delta pulse in the transducer and detecting the resulting propagation in the same place, we obtain the response $G_{s,s}(t)$ of the system to an instantaneous excitation at the transducer and compute its Fourier transform $G_{s,s}(\varepsilon)$.

2. We start with an empty cavity ($\psi_m(0) = 0$, $\forall m \in A$) and a wave packet in B that travels towards it (*e.g.* a Gaussian centered at x_c). The probability density at time zero is shown in the top of the left panel of Fig. 2.2. It is followed by a sequence of snapshots of the density at selected times in the range $(0, t_1)$ (with $t_1 < t_R$) increasing from top to bottom and continuing in the right panel in the range $(2t_R - t_1, 2t_R)$ from bottom to top. The transducer is indicated by a vertical dotted line in each panel.

3. During the period $0 \leq t \leq t_R$, the wave packet amplitude and phase are registered while performing a free evolution: it *enters* to the cavity, collides with the barrier and then bounces back in the wall at the right end of the system. This diffuse wave finally *escapes* towards the outer region at the left side (see left panel of Fig. 2.2). Provided that there are no localized states in the cavity and that the wave packet does not return, the condition $\psi_s(t > t_R) \simeq 0$ can be faithfully fulfilled.

4. Now our target function is the wave packet with reversed evolution $\psi_s^{\text{rev}}(t) = \psi_s^*(2t_R - t)$ with $t_R \leq t \leq 2t_R$. Using the information registered in the previous step, we apply a Fourier transform and normalize it according to Eq. (2.27) as shown in Fig. 2.3. Transforming back to time we get the actual time dependent injection acting for a period t_R. The injection also produces a wave packet that travels to the left, *i.e.* escaping to the outer region. Hence, the perfect time reversion is restricted only to the cavity.

5. Once the injection has ceased, the *original* wave packet is recovered at time $2t_R$ with an inverted momentum: this can be seen as the Loschmidt echo. Figure 2.2 also shows, in red solid line, the echo resulting from TRM procedure. It requires only the recording of the outgoing wave described in step 3 which is time reversed and reinjected without further processing.

Notably, the PIF and TRM recovered signals are remarkably similar[1], their shape in $(t_R, 2t_R)$ is the same and coincides with the exact case. This indicates the high accuracy of the TRM in this condition where the relevant energies of the wave packet occupy a narrow region of the spectrum and the incoming and outgoing components of the excitation are well resolved.

On the other hand, differences between both procedures appear when the incoming and outgoing signals superpose. In such cases the PIF procedure *filters* the outgoing portion. A system in this regime is illustrated in Fig. 2.4 where we represent the probability density at the injection site. In the upper left panel we display the forward evolution as registered at the transducer. Here, one can roughly identify three time regimes: entrance (incoming) and escape (outgoing), separated by a (mixed) region where both components interfere. The lower left panel displays the time reversal procedure. The TRM would inject only the portion of the outgoing waves as registered in the upper panel. In contrast, the PIF

[1]In fact, both curves superpose when the TRM is multiplied by a factor $2V/\hbar$.

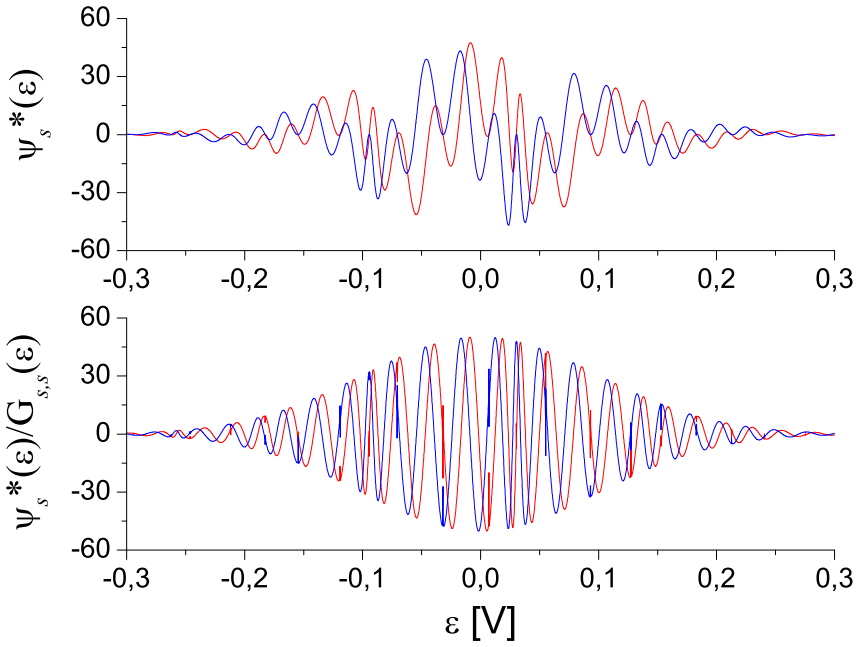

Figure 2.3: Top panel: Fourier transform of the registered wave amplitude at x_s. Real (red) and imaginary (blue) components are shown. Bottom panel: the same function is filtered through the PIF prescrition obtaining the injection function $\chi_s^{\rm PIF}(\varepsilon)$ (the phase that points the origin of time is omitted here).

procedure yields an injection that extends to the mixed region shown as a dark cyan dash-dotted line. The PIF intensity (blue dashed line) constitutes a substantial improvement over the TRM signal (red dotted line). According to the right panel, an exact coincidence between the original density and that obtained from the PIF procedure is found for all the points inside the cavity indicating a perfect time reversal.

For the considered situation, the TRM focusing can be improved by choosing a more natural separation between the incoming and outgoing components of the wave packet. Whenever provided by the experiment, the isolated incoming wave packet can be obtained from the dynamics of the corresponding homogeneous system where the scattering and the infinite barriers have been removed. In this case, the outgoing wave is built from the subtraction of both signals and is re-emitted to the original system in the inverse temporal sequence.

In Fig. 2.5, we show the previous signal that contains the three components described above. The separated components according to the homogeneous evolution are depicted in red dotted (incoming) and blue dashed (outgoing) respectively. Although it is not a perfect

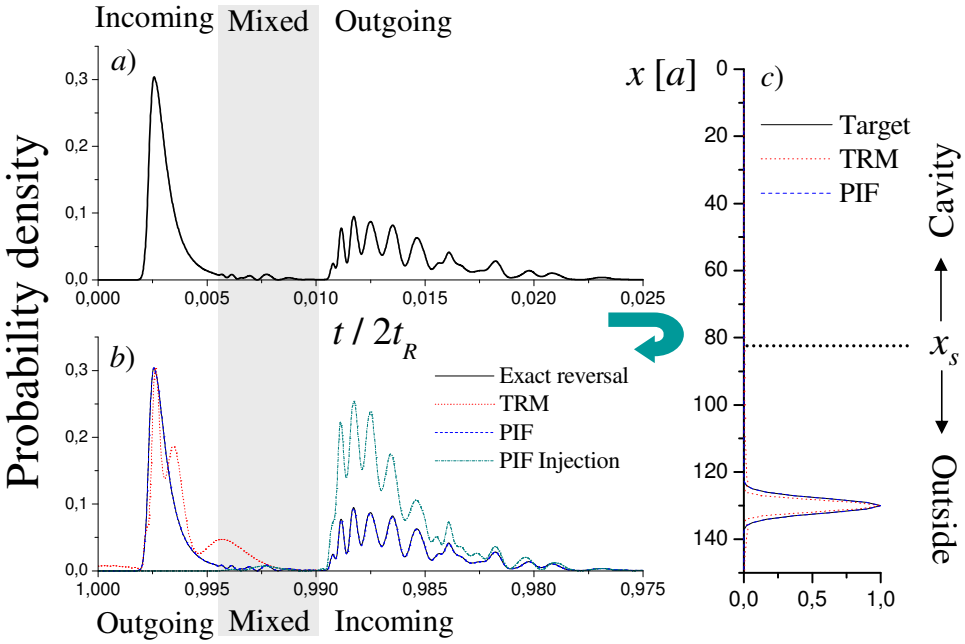

Figure 2.4: a) Probability density at x_s in the forward evolution of the wave packet. b) At right, the density injected at x_s by the PIF procedure (dark cyan dash-dotted line). Its evolution determines the reversed density (blue dashed), superposed with the exact one (black solid line). The density obtained from TRM (close to the focalization time) is depicted in red dotted line. c) Spatial focalization of the wave packet at $t = 2t_R$. The PIF (blue dashed) recovering superposes with the target wave (black solid). The height of the barrier is $0.2V$ and the width $5a$. The Gaussian wave packet has $\sigma = 3a$ and $k_0 a = 0.3\pi$.

time reversal of the initial excitation[2], the contrast in the focalization (see inset) shows an improvement over the previous approximate separation since there is no remaining excitations in the cavity. Furthermore, it is interesting to note that this outgoing wave can be conceived as the one that is originated inside the cavity. In such case, as we shall see in the following section, an exact reversion would require the correction given by the PIF for the internal source case.

2.3 Internal Perfect Inverse Filter

We now consider the situation in which, at the initial time, the excitation is concentrated inside the cavity. From $t_0 = 0$ until a registration time t_R, the discrete wave function

$$\psi_s(t) = \sum_{n \in A} \mathrm{i}\hbar G^R_{s,n}(t)\psi_n(0), \qquad 0 \leq t \leq t_R, \tag{2.38}$$

[2]Differences with the exact case are particularly due to the narrowness of the initial excitation.

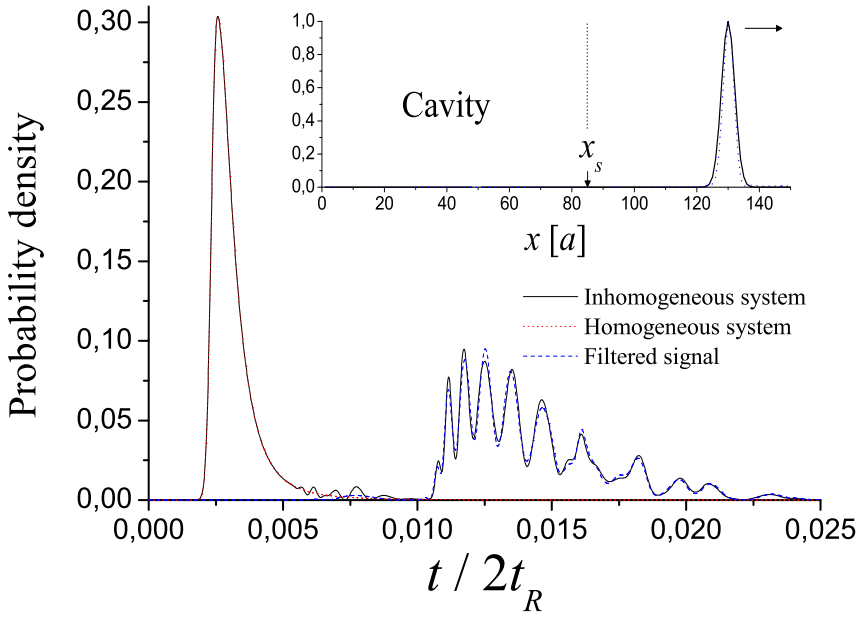

Figure 2.5: Filtering of the registered signal (black solid) between the incoming (red dotted) and the outgoing (blue dashed) components according to the corresponding homogeneous case. Inset: comparison of the rescaled spatial focalizations for the TRM (blue dashed) and the exact one (black solid).

is detected and recorded as it escapes through the frontier. The cavity A, either integrable or chaotic, is opened by a waveguide consisting of a 1d channel. Therefore, its frontier is controlled by a single transducer at $x_s = sa$, with s integer and a the distance between neighbor sites in the waveguide. Assuming that there are no localized states, the registration time t_R is taken long enough in order to ensure that all excitations leave the cavity. Although apparently a restriction, this simple model faithfully represents the essential underlying physics. A straightforward generalization in multi-dimensional systems would require the same idea exposed here and is developed in the following section.

As we have already shown in Sec. 2.1, the time reversion for a wave packet arriving at the cavity from the outer region is performed, in the energy domain, through the prescription

$$\chi_s^{\mathrm{PIF}}(\varepsilon) = \frac{1}{\mathrm{i}\hbar G^R_{s,s}(\varepsilon)} \psi_s^{\mathrm{rev}}(\varepsilon). \tag{2.39}$$

Here, the key is to notice that in the above expression, the Fourier transform of the

reversed signal contains the integration for all times

$$\psi_s^{\rm rev}(\varepsilon) \equiv \int_{-\infty}^{\infty} \psi_s^{\rm rev}(t) e^{{\rm i}\varepsilon t/\hbar} {\rm d}t, \tag{2.40}$$

accounting for the time reversed *complete evolution*, *i.e.* both the incoming and outgoing components are required in order to compute $\psi_s^{\rm rev}(\varepsilon)$. Since we want to reverse the signal that is produced inside the cavity, we should deal with the building up of the complete evolution from the knowledge of $\psi_s(t)$ at times $0 \leq t \leq t_R$. As a first step, we assume that the injection function is known and the reversed propagation at the transducer is

$$\psi_s^{\rm rev}(t) = \psi_s^*(2t_R - t), \tag{2.41}$$

$$= {\rm i}\hbar \int_0^t G_{s,s}^R(t-t')\chi_s^{\rm PIF}(t'){\rm d}t', \tag{2.42}$$

for times $t_R \leq t \leq 2t_R$ during the emission period. As a consequence of this PIF injection, the back propagation achieves an exact reversion inside the cavity and therefore the evolution at subsequent times ($t > 2t_R$) can be interpreted as a wave packet that starts at the focalization time with $\psi_n(2t_R) = \psi_n^*(0)$, regardless of the remanent non-returning waves outside the cavity. Thus, for subsequent times we expect for the reversed signal

$$\psi_s^{\rm rev}(t) = \sum_{n\in A} {\rm i}\hbar G_{s,n}^R(t-2t_R)\psi_n^*(0). \tag{2.43}$$

A comparison between Eqs. (2.38) and (2.43) shows us that for the most simple case in which all coefficients $\psi_n(0)$ are real, both evolutions become identical. The same but with opposite sign should be obtained if they were purely imaginary. In a more general situation where these coefficients present relative phases between them we should analyze the Fourier transform

$$\psi_s^{\rm rev}(\varepsilon) = \int_{t_R}^{2t_R} \psi_s^*(2t_R - t)e^{{\rm i}\varepsilon t/\hbar}{\rm d}t + {\rm i}\hbar \sum_{n\in A}\int_{2t_R}^{\infty} G_{s,n}^R(t-2t_R)\psi_n^*(0)e^{{\rm i}\varepsilon t/\hbar}{\rm d}t \tag{2.44}$$

$$= e^{{\rm i}\varepsilon 2t_R/\hbar}\left[\psi_s^*(\varepsilon) + {\rm i}\hbar\sum_{n\in A} G_{s,n}(\varepsilon)\psi_n^*(0)\right], \tag{2.45}$$

where the second term within the brackets can be interpreted as the *unknown* evolution for subsequent times. At this point, we account for the hopping terms $V_{s,s-1}$ and $V_{s-1,s}$ (with x_{s-1} inside de cavity) connecting the cavity with the outer region. Hence, we use the Dyson equation to rewrite

$$G_{s,n}(\varepsilon) = G_{s,n}^{(0)}(\varepsilon) + G_{s,s}(\varepsilon)V_{s,s-1}G_{s-1,n}^{(0)}(\varepsilon). \tag{2.46}$$

As compared to Eq. (2.18), notice that the inversion in the order of terms corresponds to the fact that we are refering to the internal sites n. Since the subsystem defined by the

cavity is closed and non absorbing, $V_{s,s-1}G^{(0)}_{s-1,n}(\varepsilon)$ is a real number and

$$G^*_{s,n}(\varepsilon) = G^*_{s,s}(\varepsilon)\left[V_{s,s-1}G^{(0)}_{s-1,n}(\varepsilon)\right]^* \tag{2.47}$$

$$= \frac{G^*_{s,s}(\varepsilon)}{G_{s,s}(\varepsilon)}G_{s,n}(\varepsilon). \tag{2.48}$$

Therefore, from this last property we obtain the unknown evolution as a correction in phase of the detected signal according to

$$\mathrm{i}\hbar\sum_{n\in A}G_{s,n}(\varepsilon)\psi^*_n(0) = -\frac{G_{s,s}(\varepsilon)}{G^*_{s,s}(\varepsilon)}\psi^*_s(\varepsilon), \tag{2.49}$$

which allows to rewrite the complete time reversed wave function that crosses the transducer (Eq. (2.45)) in terms of the partial detection

$$\psi^{\mathrm{rev}}_s(\varepsilon) = e^{\mathrm{i}\varepsilon 2t_R/\hbar}\left[1-\frac{G_{s,s}(\varepsilon)}{G^*_{s,s}(\varepsilon)}\right]\psi^*_s(\varepsilon). \tag{2.50}$$

Now that we have the complete $\psi^{\mathrm{rev}}_s(\varepsilon)$, the injection function according to the PIF formula is given by

$$\chi^{\mathrm{PIF}}_s(\varepsilon) = \frac{1}{\mathrm{i}\hbar G_{s,s}(\varepsilon)}\psi^{\mathrm{rev}}_s(\varepsilon) \tag{2.51}$$

$$= \frac{2}{\hbar}e^{\mathrm{i}\varepsilon 2t_R/\hbar}\ \mathrm{Im}\ G^{-1}_{s,s}(\varepsilon)\ \psi^*_s(\varepsilon). \tag{2.52}$$

This constitutes the PIF prescription for the case where the initial state is an excitation inside the cavity. As we shall see, the imaginary component of the inverse in $G_{s,s}(\varepsilon)$ is closely related to the group velocity of the scattered waves in the outer region. Therefore, contrary to the external source condition, the correction imposed by the PIF under the internal source case does not depend on the detailed structure of the cavity.

An alternative and more compact formulation for the internal PIF may be obtained based on the fundamental optical theorem [PFM02]. In words, it states that the continuous density of states at a given site x_0 is built upon the escape rates through the boundaries of the system. If we choose a semi-infinite chain and there is no escape to the left of site x_0, the excitation can only escape to the right of the frontier x_s with a rate[3] $\Gamma_s(\varepsilon)/\hbar$. In equations:

$$\mathrm{Im}G_{0,0}(\varepsilon) = G_{0,s}(\varepsilon)\Gamma_s(\varepsilon)G^*_{s,0}(\varepsilon). \tag{2.53}$$

Multiplying both sides by a pulse $\mathrm{i}\hbar\xi(\varepsilon)$ we find

$$\mathrm{i}\hbar\left[G_{0,0}(\varepsilon)-G^*_{0,0}(\varepsilon)\right]\xi(\varepsilon) = 2\mathrm{i}G_{0,s}(\varepsilon)\Gamma_s(\varepsilon)(-\mathrm{i}\hbar)G^*_{s,0}(\varepsilon)\xi(\varepsilon). \tag{2.54}$$

[3]The close connection between $\Gamma_s(\varepsilon)$ and the Green's function will be deduced explicitly in the following examples.

Since the outgoing wave originated at the focal point x_0 writes

$$\psi_0(\varepsilon) = \mathrm{i}\hbar G_{0,0}(\varepsilon)\xi(\varepsilon), \tag{2.55}$$

we reobtain the PIF prescription by identifying the second term in the left hand of Eq. (2.54) as the backward evolution in the focal point. Hence, the complete evolution, identical to the reversed one, results

$$\psi_0(\varepsilon) + \psi_0^*(\varepsilon) = \psi_0^{\mathrm{rev}}(\varepsilon) \tag{2.56}$$

$$= \mathrm{i}\hbar G_{0,s}(\varepsilon)\left[\frac{2}{\hbar}\Gamma_s(\varepsilon)\psi_s^*(\varepsilon)\right]. \tag{2.57}$$

The term between the square brackets is the excitation that should be injected at x_s to reproduce the reversed original signal in the cavity and coincides with the PIF prescription obtained in Eq. (2.52), provided that $\Gamma_s(\varepsilon) = \mathrm{Im}G_{s,s}^{-1}(\varepsilon)$ and $2t_R$ is redefined as the origin of time.

2.3.1 Multi-dimensional internal PIF

In the internal case, we deal with the construction of the subsequent times propagation as shown in Eq. (2.45). In this multi-transducer case, it takes the form

$$|\psi_S^{\mathrm{rev}}\rangle = e^{\mathrm{i}\varepsilon 2t_R/\hbar}\left[|\psi_S^*\rangle + \mathrm{i}\hbar\mathbb{G}_{S,A}\,|\psi_A^*\rangle\right], \tag{2.58}$$

noticing that the second term within the brackets is the "unknown" evolution. The subspaces separation is done through the hopping matrices $\mathbb{V}_{S,\tilde{A}}$ and $\mathbb{V}_{\tilde{A},S}$ connecting the cavity with the outer region. Here, $\tilde{A}$ is the subset of sites in the cavity that link to the array of transducers just outside. Hence, it is possible to rewrite $\mathbb{G}_{S,A}$ in terms of the Dyson equation

$$\mathbb{G}_{S,A} = \mathbb{G}_{S,A}^{(0)} + \mathbb{G}_{S,S}\mathbb{V}_{S,\tilde{A}}\mathbb{G}_{\tilde{A},A}^{(0)}. \tag{2.59}$$

For the considered Green's functions we have $\mathbb{G}_{S,A}^{(0)} = \mathbb{G}_{S,A}^{(0)} = 0$ and since the subsystem A is closed and non absorbing, $\mathbb{G}_{A,\tilde{A}}^{(0)}\mathbb{V}_{\tilde{A},S}$ is a real matrix. Therefore, we obtain for the complex conjugate Green's function

$$\mathbb{G}_{S,A}^* = \mathbb{G}_{S,S}^*\mathbb{V}_{S,\tilde{A}}\mathbb{G}_{\tilde{A},A}^{(0)} = \mathbb{G}_{S,S}^*\mathbb{G}_{S,S}^{-1}\mathbb{G}_{S,A}, \tag{2.60}$$

where the complex conjugate operation $(*)$ should not be confused with the adjoint $(\dagger)$. For the backward propagation we found

$$\mathrm{i}\hbar\mathbb{G}_{S,A}\,|\psi_A^*(0)\rangle = \mathrm{i}\hbar\mathbb{G}_{S,S}\left[\mathbb{G}_{S,S}^*\right]^{-1}\mathbb{G}_{S,A}^*\,|\psi_A^*(0)\rangle = -\mathbb{G}_{S,S}\left[\mathbb{G}_{S,S}^{-1}\right]^*|\psi_S^*\rangle\,, \tag{2.61}$$

where the relation

$$\left[\mathbb{G}_{S,S}^*\right]^{-1} = \left[\mathbb{G}_{S,S}^{-1}\right]^*, \tag{2.62}$$

is readily deduced from

$$\mathbb{G}_{S,S}\mathbb{G}_{S,S}^{-1} = \mathbb{I} = \mathbb{I}^* = \mathbb{G}_{S,S}^* \left[\mathbb{G}_{S,S}^{-1}\right]^* . \tag{2.63}$$

Finally, we use this last expression and rewrite Eq. (2.58) as

$$|\psi_S^{\text{rev}}\rangle = e^{\mathrm{i}\varepsilon 2t_R/\hbar}\left[\mathbb{I} - \mathbb{G}_{S,S}\left[\mathbb{G}_{S,S}^{-1}\right]^*\right]|\psi_S^*\rangle . \tag{2.64}$$

Now that we have the complete $|\psi_S^{\text{rev}}\rangle$, the injection function according to the PIF formula is given by

$$\left|\chi_S^{\text{PIF}}\right\rangle = \frac{1}{\mathrm{i}\hbar}\mathbb{G}_{S,S}^{-1}|\psi_S^{\text{rev}}\rangle = \frac{2}{\hbar}e^{\mathrm{i}\varepsilon 2t_R/\hbar}\text{Im}\ \mathbb{G}_{S,S}^{-1}\ \ |\psi_S^*\rangle , \tag{2.65}$$

in complete consistency with the (scalar) single transducer version of Eq. (2.52).

2.3.2 Application examples

PIF in a quantum bazooka configuration

In order to evaluate the Eq. (2.52) we propose a model for a quantum bazooka device composed by a stadium billiard coupled with a one-dimensional waveguide as shown in Fig. 2.6. The discretization in the Schrödinger equation gives the tight-binding structure of the Hamiltonian

$$\mathbb{H} = \mathbb{H}_A + \mathbb{H}_{AB} + \sum_{j\in B}\left(E_j\hat{c}_j^+\hat{c}_j + V_{j,j+1}\hat{c}_{j+1}^+\hat{c}_j + \text{h.c.}\right), \tag{2.66}$$

where $\mathbb{H}_A$ is the Hamiltonian of the billiard in a discrete basis and $\mathbb{H}_{AB}$ the coupling with the waveguide B.

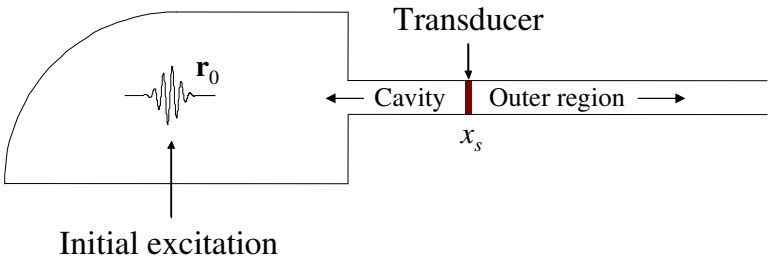

Figure 2.6: Basic scheme of a quantum bazooka device with a localized excitation inside. In the tight-binding model, the waveguide coupled to the billiard is represented by a one-dimensional semi-infinite chain.

Supposing a single semi-infinite waveguide, the cavity results delimited by a single transducer at site x_s. The Green's function is obtained through the decimation technique (see Appendix A) as

$$G_{s,s}(\varepsilon) = \frac{1}{\varepsilon - E_s - \Sigma_{\text{in}}(\varepsilon) - \Sigma_{\text{out}}(\varepsilon)}, \tag{2.67}$$

where $\Sigma_{\text{in}}(\varepsilon)$ and $\Sigma_{\text{out}}(\varepsilon)$ are the corrections to the self energy due to the presence of the sites inside and outside the cavity respectively [PMe01]. Note here that the contribution to the self energy due to the presence of the billiard is included in the $\Sigma_{\text{in}}(\varepsilon)$ term.

Decimation on the cavity gives the $\Sigma_{\text{in}}(\varepsilon)$ contribution as a continued fraction composed by the internal hoppings and site energies. In absence of magnetic fields or dissipation those parameters are all real numbers. Therefore,

$$\Sigma_{\text{in}}(\varepsilon) = \cfrac{V_{s,s-1}V_{s-1,s}}{\varepsilon - E_{s-1} - \cfrac{V_{s-1,s-2}V_{s-2,s-1}}{\varepsilon - E_{s-2} - \cdots \frac{V_{1,0}V_{0,1}}{\varepsilon - E_0 - \ldots}}}, \tag{2.68}$$

is also a real function, regardless the details of $\mathbb{H}_A$.

On the other hand, in the limit where the number of sites increases indefinitely, the homogeneous outer region, a linear chain with site energies E_{o} and hoppings V, contributes to the self energy as a complex function [PMe01]:

$$\Sigma_{\text{out}}(\varepsilon) = \Delta(\varepsilon) - \mathrm{i}\Gamma(\varepsilon), \tag{2.69}$$

with

$$\Delta(\varepsilon) = \begin{cases} \frac{\varepsilon - E_{\text{o}}}{2} + \sqrt{\left(\frac{\varepsilon - E_{\text{o}}}{2}\right)^2 - V^2} & \varepsilon - E_{\text{o}} < -2\,|V| \\ \frac{\varepsilon - E_{\text{o}}}{2} & |\varepsilon - E_{\text{o}}| \leq 2\,|V| \\ \frac{\varepsilon - E_{\text{o}}}{2} - \sqrt{\left(\frac{\varepsilon - E_{\text{o}}}{2}\right)^2 - V^2} & \varepsilon - E_{\text{o}} > 2\,|V| \end{cases}, \tag{2.70}$$

and

$$\Gamma(\varepsilon) = \begin{cases} \sqrt{V^2 - \left(\frac{\varepsilon - E_{\text{o}}}{2}\right)^2} & |\varepsilon - E_{\text{o}}| \leq 2\,|V| \\ 0 & |\varepsilon - E_{\text{o}}| > 2\,|V| \end{cases}. \tag{2.71}$$

In homogeneous systems where all the energies and hoppings are the same, the set of equations given by Eq. (2.4)

$$(\varepsilon - E_{\text{o}})\psi_j(\varepsilon) - V\left(\psi_{j-1}(\varepsilon) + \psi_{j+1}(\varepsilon)\right) = 0, \tag{2.72}$$

can be solved by the plane wave $\psi_j(\varepsilon_k) = \psi_k e^{-\mathrm{i}kja}$ that gives.

$$(\varepsilon_k - E_{\text{o}})\psi_k e^{-\mathrm{i}kja} + V\psi_k e^{-\mathrm{i}kja}\left(e^{\mathrm{i}ka} + e^{-\mathrm{i}ka}\right) = 0, \tag{2.73}$$

and defines the dispersion relation for the asymptotic waves

$$\varepsilon_k = E_{\text{o}} - 2V\cos(ka). \tag{2.74}$$

Then, the relationship between $\Gamma(\varepsilon)$ and the group velocity can be found as follows

$$v_g(\varepsilon_k) = \frac{1}{\hbar}\frac{\mathrm{d}\varepsilon_k}{\mathrm{d}k} = \frac{2Va}{\hbar}\sin(ka) = v_{\max}\sin(ka) \tag{2.75}$$

$$= v_{\max}\sqrt{1 - \left(\frac{\varepsilon_k - E_{\text{o}}}{2V}\right)^2} = \frac{2a}{\hbar}\Gamma(\varepsilon_k). \tag{2.76}$$

We choose $E_o = 2V$ so that the differential form of the Schrödinger equation for a particle with mass m is obtained as the limit $\hbar^2/2Va^2 \longrightarrow m$ when $V \to \infty$ and $a^2 \to 0$. Since only the imaginary component from $\Sigma_{\text{out}}(\varepsilon)$ is required, Eq. (2.52) writes

$$\chi_s^{\text{PIF}}(\varepsilon) = \frac{2}{\hbar} e^{\mathrm{i}\varepsilon 2t_R/\hbar} \Gamma(\varepsilon) \psi_s^*(\varepsilon). \tag{2.77}$$

The complex exponential serves to define the origin of time, and hence we can neglect it. Using the above definition of $\Gamma(\varepsilon)$ we get

$$\chi_s^{\text{PIF}}(\varepsilon) = \sqrt{1 - \left(\frac{\varepsilon - 2V}{2V}\right)^2} \frac{2V}{\hbar} \psi_s^*(\varepsilon) \tag{2.78}$$

$$= \frac{v_g(\varepsilon)}{v_{\max}} \chi_s^{\text{TRM}}(\varepsilon). \tag{2.79}$$

The exact reversal requires the injection of a TRM signal filtered by the group velocity of the scattered waves. When the initial state is a local excitation composed by a few sites inside the cavity, the Fourier transform of the detected signal $\psi_s(\varepsilon)$ will cover the whole energy band. The factor in the PIF procedure shows that in dispersive media the correction is effective near the band edges where the group velocity becomes negligible.

In the numerical solution, the propagation of an initial Gaussian wave packet with energy $(k_0^2 + \sigma^{-2})a^2V$ is recorded by a single transducer placed in the waveguide consisting of a single propagating mode (in practice, this waveguide is well represented by a one-dimensional chain). The time evolution was performed through a second order Trotter-Suzuki algorithm [Rae96]. Fig. 2.7 shows the recovered signal at the focal point, *i.e.* the center of the original wave packet. The focalization functions for both methods are close to the exact reversed propagation. However, a slight broadening of the focalized wave packet is observed in the TRM. In this case, the differences between PIF and TRM procedures are small because the initial excitation is mainly composed by states whose group velocity in the outgoing channel remains almost constant.

As mentioned before, when the initial state is a local excitation composed by a few sites inside the cavity, the Fourier transform of the detected signal $\psi_s(\varepsilon)$ will cover the whole energy band between $-2V$ and $2V$ and structural differences between both methods should appear.

Multichannel PIF

A more general case where the multi-dimensional version of Eq. (2.52) can be tested is the multichannel system schematically pictured in Fig. 2.8.

The idea is to generalize our previous result for frontiers fully delimited by an array of transducers according to Eq. (2.65). Here, a two dimensional cavity is surrounded by N_L transducers at the left and N_R at right. The total Hamiltonian is written as

$$\mathbb{H} = \begin{pmatrix} \mathbb{H}_L & \mathbb{V}_{L,C} & 0 \\ \mathbb{V}_{C,L} & \mathbb{H}_C & \mathbb{V}_{C,R} \\ 0 & \mathbb{V}_{R,C} & \mathbb{H}_R \end{pmatrix}, \tag{2.80}$$

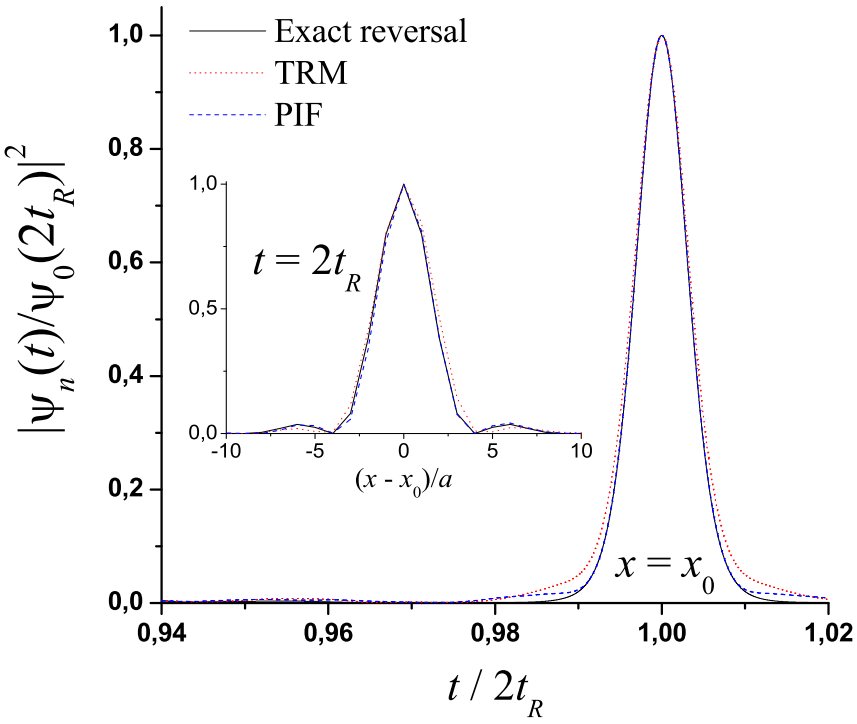

Figure 2.7: Focalization at the focal point for TRM (red dotted) and PIF (blue dashed) procedures contrasted with the exact reversal (black solid). PIF and TRM curves coincide with the exact one for times close to $2t_R$. Left inset: spatial contrast in the recovered signal at $t = 2t_R$.

where $\mathbb{H}_C$ is the block tridiagonal Hamiltonian describing the cavity and $\mathbb{H}_L$ ($\mathbb{H}_R$) is the Hamiltonian on the left (right) side. $\mathbb{V}_{L,C}$ and $\mathbb{V}_{C,R}$ are real matrices containing the hopping terms between the boundaries and the cavity. The unitary transform

$$\mathbb{U} = \begin{pmatrix} \mathbb{U}_L & 0 & 0 \\ 0 & \mathbb{I}_C & 0 \\ 0 & 0 & \mathbb{U}_R \end{pmatrix}, \tag{2.81}$$

with $\mathbb{I}_C$ the identity matrix in the cavity, separates the outer region into $N_L + N_R$ independent channels consisting of one-dimensional homogeneous chains[4]. The corresponding energy E_k^α of the k-channel, with α being L or R, follows the dispersion relation given by Eq. (2.74) for a finite number of sites, *i.e.*

$$E_k^\alpha = E_o - 2V \cos\left(\frac{k\pi}{N_\alpha + 1}\right), \tag{2.82}$$

[4]With *homogeneous* we mean that all the hoppings and site energies are the same.

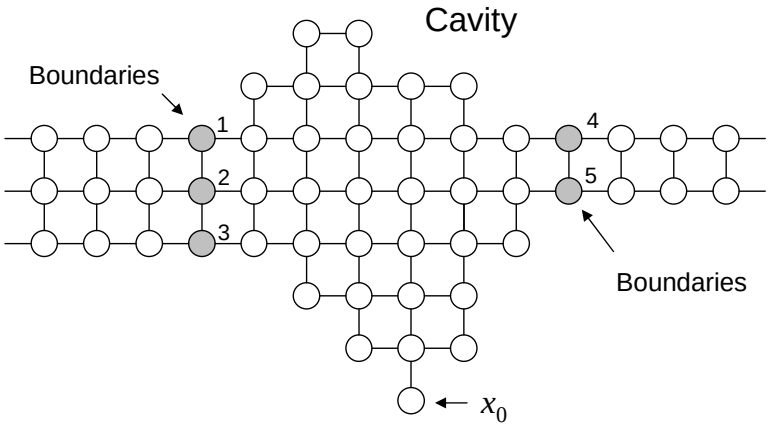

Figure 2.8: Scheme of the multichannel system.

where $k = 1, \ldots, N_\alpha$ and

$$[\mathbb{U}_\alpha]_{nk} = u^\alpha_{nk} = u^\alpha_{kn} = \sqrt{\frac{2}{N_\alpha + 1}} \sin\left(\frac{nk\pi}{N_\alpha + 1}\right), \tag{2.83}$$

is the n-site component of the k-channel.

By performing a decimation process in each one of these channels, the correction to the self energy is obtained from the diagonalization of each side Hamiltonian $\mathbb{H}_\alpha$

$$\tilde{\mathbb{H}}_{k,k} \equiv \left[\mathbb{U}^\dagger \mathbb{H} \mathbb{U}\right]_{k,k} = E^\alpha_k - \Sigma(\varepsilon - E^\alpha_k), \tag{2.84}$$

whenever the k-index runs over the boundaries of the cavity. Then, the Green's function in the reduced basis of the array of transducers can be expressed as

$$\mathbb{G}_{\alpha,\beta} \equiv \left[(\varepsilon \mathbb{I} - \mathbb{H})^{-1}\right]_{\alpha,\beta}, \tag{2.85}$$

and therefore we have

$$\begin{aligned} \text{Im}\ \mathbb{G}^{-1}_{\alpha,\beta} &= \text{Im}\left(\varepsilon \mathbb{I} - \mathbb{H}\right)_{\alpha,\beta} && (2.86)\\ &= -\left[\mathbb{U}\ \text{Im}\tilde{\mathbb{H}}\ \mathbb{U}^\dagger\right]_{\alpha,\beta}. && (2.87) \end{aligned}$$

The unitary transformation $\mathbb{U}$ is a diagonal block matrix without mixing terms between L and R sides of the cavity yielding, as indicated in Eq. (2.84),

$$\text{Im}\left[\mathbb{G}^{-1}_{S,S}\right]_{(n,m)\in\alpha} = \sum_{k=1}^{N_\alpha} u^\alpha_{nk} \Gamma(\varepsilon - E^\alpha_k) u^\alpha_{km}, \tag{2.88}$$

where $(n, m) \in \alpha$ means that both n and m transducers are taken in the same side of the system. Thus, the injection function is obtained by replacing Eq. (2.88) in Eq. (2.65) as,

$$\left|\chi^{\text{PIF}}_{S,\alpha}\right\rangle_n = \frac{2}{\hbar} e^{\mathrm{i}\varepsilon 2t_R/\hbar} \sum_{k,m=1}^{N_\alpha} u^\alpha_{nk} \Gamma(\varepsilon - E^\alpha_k) u^\alpha_{km} \left|\psi^*_{S,\alpha}\right\rangle_m. \tag{2.89}$$

As we have shown previously, the PIF correction for the internal source case is given by the group velocity at the boundaries. Notice here that the $\Gamma(\varepsilon)$ factors are centered on the self energies E_k^α whose width is given by the hoppings in the outer region.

A numerical evolution was performed in the time domain through a second order Trotter-Suzuki method [Rae96]. In the considered example, we have $N_L = 3$ transducers to the left and $N_R = 2$ to the right and the propagation is favored through the vertical hoppings[5]. Depending on this particular choice of the parameters, the PIF correction presents relevant differences with the TRM counterpart.

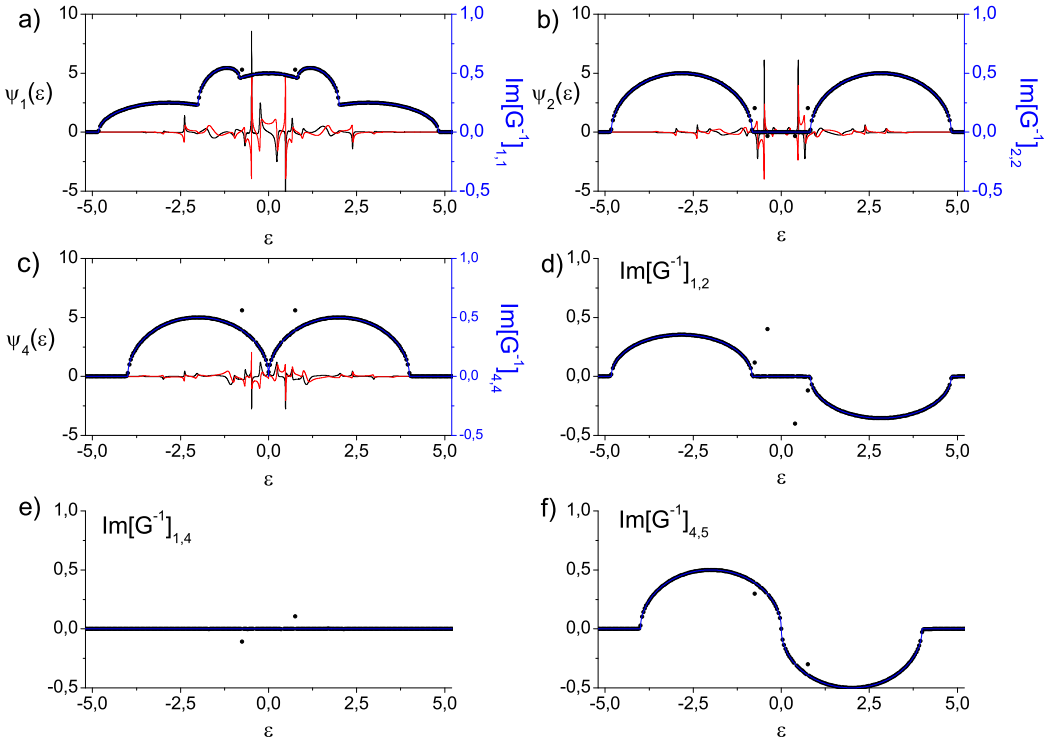

Figure 2.9: Representative elements of the PIF correcion: numerical in thick black points and analytical in thin blue line. Real and imaginary components of $\psi_s(\varepsilon)$ are shown for comparison.

The time-dependent response functions $G^R_{s',s}(t)$ between the transducers at the boundaries are then computed and a numerical Fourier transform is performed in order to obtain the 5×5 matrix $\mathbb{G}_{S,S}$. The analytical and numerical evaluations of Eq. (2.88) are depicted in Fig. 2.9 for representative elements of Im $\mathbb{G}^{-1}_{S,S}$, suggesting how the group velocities are mixed. Figures 2.9a, b and c show the diagonal elements and the Fourier transform of

[5]According to Fig. 2.8, the vertical hoppings were set as twice of the horizontal ones.

the detected signals for transducers 1,2 and 4 respectively. For the transducers 2 and 4, the correction becomes effective in the central region of the spectrum where the detected signals are still appreciable. In agreement with Eq. (2.88), Fig. 2.9e shows that no mixing exists between transducers belonging to different sides of the cavity. We can observe a little portion of points from the numerical results that does not fit with the analytical curves. These appear because of the finite registration time.

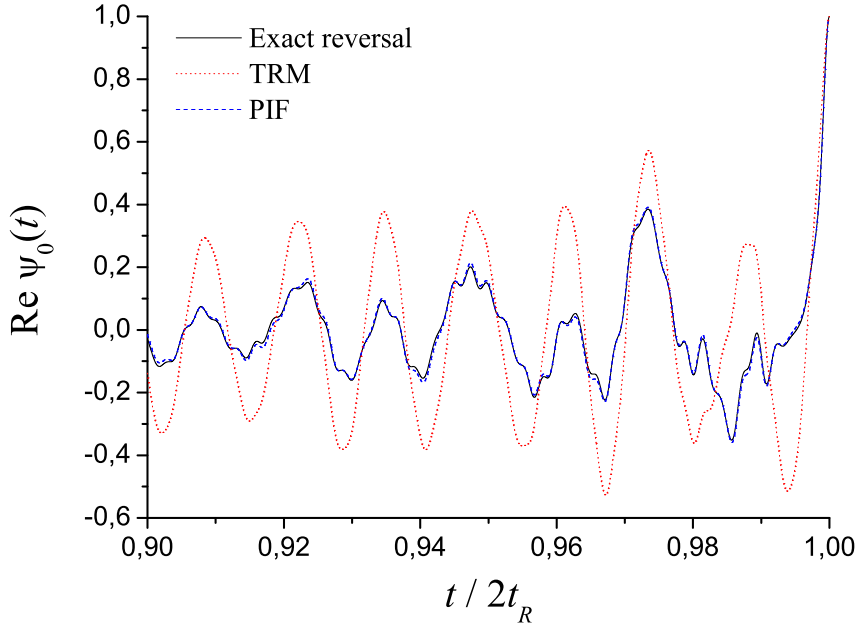

Figure 2.10: Recovering of the initial condition in the focal site x_0. The ideal reversed evolution is in black solid line and the both procedures, TRM (red dotted) and PIF (blue dashed), are contrasted.

Now that we have the corrected injection, we reverse the dynamics and compare it with the TRM case. Although the TRM achieves a reasonable quality in the spatial focalization, differences appear both for the time evolution at the focal site (see Fig. 2.10) and the spatial distribution (contrast) of the recovered signal at the focalization time, as shown in Fig. 2.11. On the other hand, notice that in the continuum limit where the self energies are close together and the band width becomes wider, the PIF correction reduces to a constant pre-factor, justifying the efficiency of the TRM.

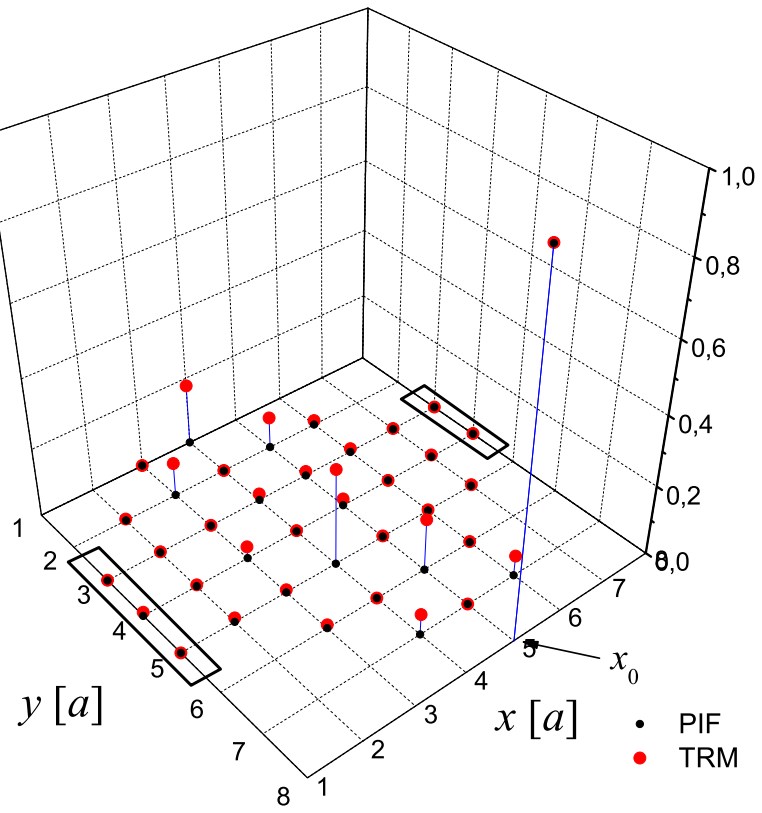

Figure 2.11: Normalized spatial distribution for the recovered initial excitation in the cavity. The location of the transducers is indicated by rectangles.

2.4 Comparison with other results

In addition to the TRM, Fink and collaborators proposed the spatiotemporal inverse filter (STIF) for acoustic waves as a focusing method that optimizes spatial contrast [TTF00]. It requires the inversion of the Fourier transform of the direct wave field propagator, *i.e.* the matrix built from the temporal response at the transducers to a Dirac delta function in each control point within the focal region. Unlike the TRM, the STIF injection acts as a highly invasive technique because it is necessary to measure the full propagator whereas the former only need to compute the row related to the focal point. Recently, an alternative proposal by Vignon et al. [VRA07], denoted minimally invasive STIF (miSTIF), achieved the same focusing quality than STIF. The idea behind this procedure is that all the information in the wave field propagator can be deduced from the backscattering signals of the transducer array at the boundaries and the technique results no more invasive than TRM. In this context, miSTIF and PIF result similar because they correct the TRM injection function using the propagator matrix in the reduced basis of the transducers.

It is interesting to show some similarities between PIF and the mentioned focusing procedures. We will consider a simple example with a single transducer at x_s and a focusing point located in x_0. The goal of STIF is to inject some signal at x_s that, at a later time, is able to form a spatiotemporal delta function in x_0. The strategy is to compute the inverse of the propagator $G_{s,0}(\varepsilon)$. Thus, the injection proposed could be interpreted as that which achieves the time reversal of an hypothetical pulse emitted by a source at x_0, *i.e.* $s_n(t) = \delta_{n,0}\delta(t)$, resulting

$$\chi_s^{\mathrm{STIF}}(\varepsilon) = G_{s,0}^{-1}(\varepsilon)\frac{s_0(\varepsilon)}{2V} \tag{2.90}$$

$$= \left[G_{s,0}^{*}(\varepsilon)G_{0,s}(\varepsilon)\right]^{-1} G_{s,0}^{*}(\varepsilon)\frac{s_0(\varepsilon)}{2V}. \tag{2.91}$$

Since the time reversal mirror injection is given by

$$\chi_s^{\mathrm{TRM}}(\varepsilon) = \frac{2V}{\hbar}\psi_s^{*}(\varepsilon), \tag{2.92}$$

and

$$\psi_s^{*}(\varepsilon) = -\mathrm{i}\hbar G_{s,0}^{*}(\varepsilon)s_0(\varepsilon), \tag{2.93}$$

we can rewrite the STIF as a filter

$$\chi_s^{\mathrm{STIF}}(\varepsilon) = \frac{1}{(2V)^2}\left[G_{s,0}^{*}(\varepsilon)G_{0,s}(\varepsilon)\right]^{-1}\chi_s^{\mathrm{TRM}}(\varepsilon). \tag{2.94}$$

Notice that this filter requires the determination of the non-local Green's function connecting the transducer and the focal point. Therefore, the miSTIF was developed as a procedure that replaces it in terms of the local Green's function at the transducer site. Such replacement is enabled by the optical theorem

$$\mathrm{Im}G_{s,s}(\varepsilon) = G_{s,0}(\varepsilon)\mathrm{Im}\Sigma_0^{-}G_{0,s}^{*}(\varepsilon) + G_{s,s}(\varepsilon)\mathrm{Im}\Sigma_s^{+}G_{s,s}^{*}(\varepsilon), \tag{2.95}$$

applied to an infinite chain where $x_s > x_0$. Here, Σ_0^{-} (Σ_s^{+}) is the self energy correction that accounts for the free propagation at the left (right) of the focal point (transducer) whose imaginary part is Γ_0^{-} (Γ_s^{+}). Since

$$\mathrm{Im}G_{s,s}(\varepsilon) \equiv G_{s,s}(\varepsilon)\mathrm{Im}[\Sigma_s^{+} + \Sigma_s^{-}]G_{s,s}^{*}(\varepsilon), \tag{2.96}$$

we may use that, in a homogeneous system, the escape at both sides has the same group velocities

$$\mathrm{Im}[\Sigma_s^{+} + \Sigma_s^{-}] = -2\Gamma_s. \tag{2.97}$$

In consequence, under this restricted condition, the optical theorem leads to

$$G_{s,0}^{*}(\varepsilon)G_{0,s}(\varepsilon) = -\frac{1}{2\Gamma_0}\mathrm{Im}G_{s,s}(\varepsilon), \tag{2.98}$$

from which the miSTIF prescription can be obtained as a broad-band approximation to Eq. (2.94) in which $\Gamma_0(\varepsilon) = \Gamma_s(\varepsilon) \sim V$, and finally

$$\chi_s^{\mathrm{miSTIF}}(\varepsilon) = \frac{1}{2V}\left[-\mathrm{Im}G_{s,s}(\varepsilon)\right]^{-1}\chi_s^{\mathrm{TRM}}(\varepsilon), \tag{2.99}$$

i.e. the minimally invasive spatiotemporal inverse filter consists of the inverse of the imaginary component of the Green's function at the site of the transducer. In a multi-transducer system, this miSTIF corrects the TRM in the reduced basis of the transducers.

A comparison between miSTIF and PIF shows that both coincide when the self-energy correction to the left and right sides of the chain are the same and

$$G_{s,s}(\varepsilon) = \frac{1}{\varepsilon - 2\Delta(\varepsilon) + \mathrm{i}2\Gamma(\varepsilon)} \tag{2.100a}$$

$$= -\frac{\mathrm{i}}{2\Gamma(\varepsilon)}, \qquad |\varepsilon - E_{\mathrm{o}}| < 2V \tag{2.100b}$$

and hence, in that particular case

$$\frac{1}{\mathrm{Im}G_{s,s}(\varepsilon)} = \mathrm{Im}\frac{-1}{G_{s,s}(\varepsilon)}, \tag{2.101}$$

and both injection prescriptions, PIF and miSTIF, become proportional.

In turn, since PIF is an exact procedure, it allows to test the efficiency of miSTIF in focusing the excitation to achieve a spatiotemporal delta function. This actually results as the back-propagation of the *original* pulse excitation. As such, in our one dimensional homogenous case, the amplitude at the focal point is not a delta function in the time domain but $J_0(2Vt/\hbar)$, a Bessel function of first kind. In the acoustic case, where the wave function normalization is not required, this may be conceived as an approximant to the delta function as $V \to \infty$.

2.5 Summary

In summary, we solved the Schrödinger equation with source boundary conditions and we obtained a general solution for the inverse time problem expressed in terms of the Green's function at the frontier of the cavity. This was achieved by the perfect inverse filter, a novel prescription that allows for the exact time reversal in the wave dynamics.

When one starts with a cavity empty of excitation, the resulting prescription filters the play-back of the signal (*i.e.* the TRM prescription) with the inverse of the Green's function that accounts for the feedback of the system. We tested both TRM and PIF prescriptions in the quantum bazooka device, where a good focalization quality was obtained. This is because the involved energies of the initial wave packet[6] were centered around a region

[6]The choice of the central energy of the wave packet was necessary in order to avoid a total reflection in the potential barrier of the cavity.

where the correction is almost constant. Furthermore, we found strong differences in the time reversal reconstruction of the initial excitation between the PIF and TRM in the case where the incoming an outgoing components of the wave packet are mixed. This situation would be an interesting implementation of the PIF in systems where the transducers are close to the inhomogeneities or in cases where one intends to separate the incoming and outgoing components of the wave.

On the other hand, we deduced the PIF prescription in the case where one starts with an excitation inside the cavity, either generated inside or arriving from a previous process. In this case, the PIF yields a much simpler prescription and contains an important result: the filter that corrects the TRM does not depend on the internal scattering, but only on the group velocities of the various propagating modes outside. Hence, this simple filter applies to two physically relevant situations:

1. When the excitation is actually originated in the interior of the cavity. In this case, one obtains a perfect reversal of the wave function for all the times after the source has been turned-off.

2. When one uses an external source in a situation that allows a clear separation between incoming and outgoing waves, one can use the recording of the outgoing wave to perfectly reverse the whole excursion of the excitation through the cavity. This condition is achieved when the boundaries are placed far enough from the reverberant region, as typically in the quantum and acoustic bazooka devices.

The obtained time reversed signal given by the TRM and PIF in a quantum bazooka has shown a small improvement of the PIF over the TRM in cases where the initial excitation is composed by states whose group velocity in the outgoing channel remains almost constant. However, we found in a multichannel system that such correction becomes effective when the initial local excitation involves the whole band of energies.

In general, the PIF correction constitutes a notable improvement over the TRM prescription in cases where the energy dependence has a non-linear dispersion relation, as described by the Schrödinger equation, when the escape velocity presents non trivial structures due to the presence of many simultaneously propagating channels or when collisions outside the cavity have a relevant contribution.

Chapter 3

Focusing of classical waves

In the previous chapter, we introduced the PIF procedure that achieves the exact time reversal in a working region of the system denoted as the cavity. The prescription was obtained by considering the propagation of quantum waves that results from the solution to the Schrödinger equation with a source in the boundaries of the cavity. Depending on the initial location of the wave packet, we found two main results:

1. When the original excitation comes from the outer region, the detected signal should be filtered through the inverse of the Green's function that accounts for the system feedback in the location of the transducer.

2. If the original wave packet is initially placed inside the cavity or the excitation results from a well resolved incoming wave (and we detect only the outgoing signal), the PIF filter no longer depends on the internal scattering and only consists of the group velocity of the propagating waves that cross towards the outer region.

The idea here is to extend the above description in classical systems taking advantage of the close correspondence between the Schrödinger and the classical wave equations. As before, our motivation comes from the fact that the PIF ensures the exact reversal and it can be used to assess the limitations of the TRM.

We will work in the discrete version of the classical wave equation since the detailed structure of the involved propagators is easily obtainable both analytically and numerically. Such situation can be faithfully reproduced by a chain of coupled harmonic oscillators. In particular, we will show that the detection and injection of either the positions or velocities of the oscillators at the frontiers of the cavity is enough to achieve the time reversal.

To begin, we introduce the harmonic chain as a discrete model of the classical wave equation and define the propagators resulting from the response to two kinds of forces: the *impulsive* force and the *displacive* force. Having established the analogy between both classical and quantum Green's functions, we deduce the internal PIF by following the same scheme of Chapter 2 and implement the prescription in a single-mode Helmholtz resonator, *i.e.* a heavy oscillating mass coupled to a one-dimensional waveguide formed by

a periodic arrangement of lighter oscillators. The generalization to a multi-dimensional system is implemented in a two-dimensional lattice where the propagating transversal modes are detected by an array of transducers.

In order to compute the dynamics of the system and to reproduce the PIF and TRM procedures numerically, we develop in Sec. 3.3 a numerical algorithm denoted as the Pair Partitioning method. As in the Trotter-Suzuki for quantum systems, it separates the Hamiltonian in pairs of coupled oscillators and applies the corresponding time evolution as a stroboscopic sequence. As we shall see, this method results perfectly reversible and the decay due to the escape in the outer region can be easily reproduced by using additional "friction" terms in the Hamiltonian. Through this method, we compare the time reversed focalizations obtained from the TRM and PIF procedures in the above mentioned examples.

3.1 Modeling the classical wave equation

In classical systems, the propagation of acoustic waves through a one-dimensional waveguide is usually described by the linear wave equation

$$\frac{\partial^2}{\partial t^2}u(x,t) = c^2\nabla_x^2 u(x,t), \tag{3.1}$$

where c is the speed of the wave and the scalar function $u(x,t)$ refers to the propagation of the wave. In its discrete version, this equation can be visualized as a chain of coupled harmonic oscillators where the coordinate x is replaced by the fixed points $x_j = ja$. Here, the j index indicates the equilibrium positions of the oscillators and a is the typical distance between them. The scalar function $u(x,t) \to u_j(t)$ accounts for the displacement on the j-oscillator with respect to its equilibrium position and the Laplacian can be approximated as the following finite difference

$$\nabla_x^2 u(x,t) \to \frac{1}{a^2}\left[u_{j+1}(t) + u_{j-1}(t) - 2u_j(t)\right]. \tag{3.2}$$

The Fourier transform on the displacement gives its representation in the frequency domain as

$$u_j(t) = \int_{-\infty}^{\infty} u_j(\omega)e^{-\mathrm{i}\omega t}\frac{\mathrm{d}\omega}{2\pi}, \tag{3.3}$$

and therefore the Eq. (3.1) writes as the set

$$\left(\omega^2 - 2\omega_{\mathrm{x}}^2\right)u_j(\omega) + \omega_{\mathrm{x}}^2\left[u_{j+1}(\omega) + u_{j-1}(\omega)\right] = 0, \tag{3.4}$$

where $\omega_{\mathrm{x}} = c/a$ represents the coupling between neighboring oscillators and, within the invoqued analogy between the oscillators and the tight-binding, it might be called *exchange* frequency. Notice that this frequency renormalizes the natural frequency of each oscillator with the value $2\omega_{\mathrm{x}}^2$, that indicate the potential energy due to interaction when

the neighbors are at equilibrium. In consequence, this can be interpreted as a mean-field or Hartree correction of the many-body problem.

In the present homogeneous case, the dispersion relation of the involved normal modes is obtained through the planar waves $u_j(\omega) = u_k \exp(-\mathrm{i}kja)$, yielding the usual solution for the acoustic modes

$$\omega_k = \pm 2\omega_\mathrm{x} \sin\left(\frac{ka}{2}\right). \tag{3.5}$$

As in the previous tight-binding model, this band structure is an inherent property of the discretization in the coordinate and it will play, again, an important rôle in the quality of the TRM. The group velocity for the free propagating waves is readily obtained as

$$v_g(\omega_k) = \frac{\mathrm{d}\omega_k}{\mathrm{d}k} = c\cos\left(\frac{ka}{2}\right), \tag{3.6}$$

$$v_g(\omega) = c\sqrt{1-\left(\frac{\omega}{2\omega_\mathrm{x}}\right)^2}, \tag{3.7}$$

and it tells us that the propagation beyond the limits of the band $\pm 2\omega_\mathrm{x}$ is forbidden. In the continuum limit where $a \to 0$, the band width tends to infinity and the relevant frequencies are kept within the range $\omega \ll 2\omega_\mathrm{x}$. Thus, the usual speed $v_g = c$ is recovered.

Additionally, we can generalize the above model by including different terms in Eq. (3.4). In the diagonal part, we account for the natural frequencies ω_i that are independent of the couplings between the masses. The exchange frequencies that appear as off-diagonal contributions may also vary depending on the masses and elastic constants of the oscillators. Hence, as pictured in Fig. 3.1, each oscillator with mass m_i and natural frequency ω_i moves in the vertical direction and is coupled to its nearest neighbors through springs whose elastic constants are $K_{i-1,i}$ at the left, and $K_{i,i+1}$ at the right. Since we seek for the exact correspondence with the longitudinal propagation of Eq. (3.1), the natural lenght of those springs are assumed to be zero. Beyond a constant term in the Hamiltonian, this restriction in the direction of movement yields a dynamics which is completely analogous to the propagation of Eq. (3.4), *i.e.* the longitudinal oscillations taking place in a one-dimensional waveguide.

The constant terms resulting from the equilibrium positions do not contribute in the dynamics and hence they can be neglected. Then, we describe the vertical displacements $u_i(t)$ through the classical Hamiltonian

$$H = \sum_i \left(\frac{p_i^2}{2m_i} + \frac{m_i\omega_i^2}{2}u_i^2\right) + \sum_i \frac{K_{i,i+1}}{2}\left(u_{i+1}-u_i\right)^2. \tag{3.8}$$

The resulting equations of motion yield

$$\dot{u}_i(t) = \frac{\partial H}{\partial p_i} = \frac{p_i}{m_i} = v_i(t), \tag{3.9}$$

$$\dot{v}_i(t) = -\frac{\partial H}{\partial u_i} = -\tilde{\omega}_i^2 u_i(t) + \frac{K_{i,i+1}}{m_i}u_{i+1}(t) + \frac{K_{i-1,i}}{m_i}u_{i-1}(t), \tag{3.10}$$

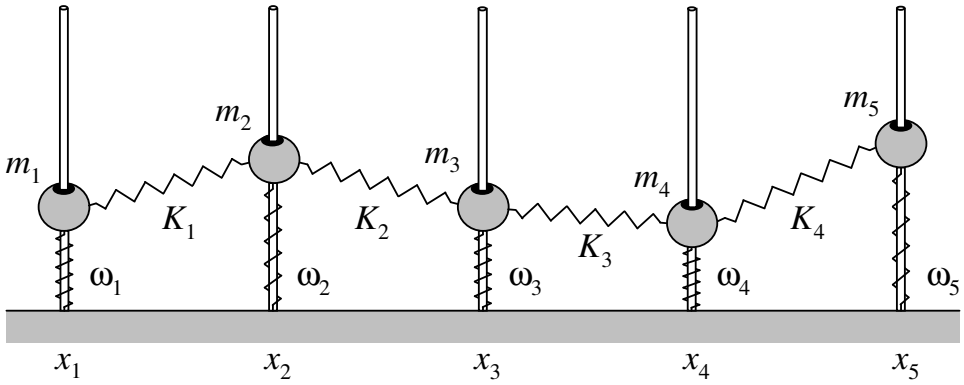

Figure 3.1: Scheme of the considered model: a one-dimensional chain of coupled oscillators. Every mass m_j with natural frequency ω_j is coupled to its first-neighbors through the springs $K_{j-1,j}$ to the left and $K_{j,j+1}$.to the right respectively.

where

$$\tilde{\omega}_i^2 = \omega_i^2 + \frac{K_{i,i+1}}{m_i} + \frac{K_{i-1,i}}{m_i}, \tag{3.11}$$

is the effective frequency that is obtained from the "static" correction due to the presence of the neighbors oscillators. The above equations are schematically depicted in Fig. 3.2. In agreement with this last, the displacements and velocities are connected through arrows pointing the origin of the time derivative. As we can see, there is no arrows connecting, in a direct way, two positions or velocities respectively. In the context of the time reversal procedures, the injection of the target signal through the modification of the oscillator's velocity will only affect to its corresponding position. This means that the recording and injection of either the displacement or velocity at the transducers is enough to perform the exact reversal.

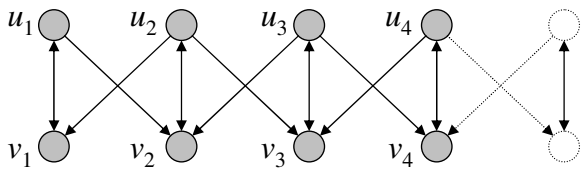

Figure 3.2: Schematics of the equations of motion for a one-dimensional chain of coupled oscillators.

In the frequency domain, these equations adopt the matrix form

$$\mathbb{D}^{-1}(\omega)\mathbf{u}(\omega) = \begin{pmatrix} \ddots & & & & \\ & \omega^2 - \tilde{\omega}_{i-1}^2 & \frac{K_{i-1,i}}{m_{i-1}} & 0 & \\ & \frac{K_{i-1,i}}{m_i} & \omega^2 - \tilde{\omega}_i^2 & \frac{K_{i,i+1}}{m_i} & \\ & 0 & \frac{K_{i,i+1}}{m_{i+1}} & \omega^2 - \tilde{\omega}_{i+1}^2 & \\ & & & & \ddots \end{pmatrix} \begin{pmatrix} \vdots \\ u_{i-1}(\omega) \\ u_i(\omega) \\ u_{i+1}(\omega) \\ \vdots \end{pmatrix} = 0, \quad (3.12)$$

where $\mathbb{D}(\omega) = \left(\omega^2\mathbb{I} - \mathbb{M}\right)^{-1}$ is the *resolvent* matrix described in the real basis and is associated to the dynamical matrix $\mathbb{M}$. Its element $D_{j,i}(t)$ denotes the position-momentum response that gives the j-th oscillator's displacement due to an instantaneous impulse in the i-th oscillator.

Thus, the resolvent provides the solutions to Eq. (3.12) as the propagation that results from a general force $F_i(t)$. Such propagation comes from the convolution in time between the applied force and the resulting response as

$$u_j(t) = \sum_i \int_0^t D_{j,i}(t-\tau)\frac{1}{m_i}F_i(\tau)\mathrm{d}\tau, \quad (3.13)$$

where $F_i(t) = f_i(t) + g_i(t)$ is applied at the i-th mass and accounts for two kinds of forces: the impulsive force and the displacive force. The impulsive force sets the initial momentum according to

$$f_i(t) = m_i\Delta\dot{u}_i(0)\delta(t), \quad (3.14)$$

and it may conceived as an instantaneous "kick" at the i-th oscillator. The displacive force is able to produce an instantaneous shift $\Delta u_j(0)$ in the position without changing its momentum. This would require that the first impulsive kick be followed by a compensating one according to

$$g_i(t) = m_i\Delta u_i(0)\lim_{\Delta t\to 0}\frac{1}{\Delta t}\left[\delta\left(t+\tfrac{1}{2}\Delta t\right) - \delta\left(t-\tfrac{1}{2}\Delta t\right)\right]. \quad (3.15)$$

If this instantaneous shift is applied at some time τ in-between of the interval $(0,t)$, the frequency dependence would read

$$g_i(\omega) = \mathrm{i}\omega m_i\Delta u_i(\tau)e^{\mathrm{i}\omega\tau}, \quad (3.16)$$

and therefore, the corresponding time-dependent displacement is

$$u_j(t) = \sum_i \int D_{j,i}(\omega)\mathrm{i}\omega\Delta u_i(\tau)e^{-\mathrm{i}\omega(t-\tau)}\frac{\mathrm{d}\omega}{2\pi} \quad (3.17)$$

$$= \sum_i G_{j,i}(t-\tau)\Delta u_i(\tau), \qquad t \geq \tau, \quad (3.18)$$

defining the position-position response, also known as the Green's function, which is related to the resolvent as

$$G_{j,i}(\omega) = \mathrm{i}\omega D_{j,i}(\omega). \tag{3.19}$$

On the other hand, we will use linearity to write the observed displacement in terms of $\delta u_i(t)$, defined as the forced position shift accumulated in the unit time according to

$$u_j(t) = \sum_i \int G_{j,i}(t-\tau)\delta u_i(\tau)\mathrm{d}\tau. \tag{3.20}$$

This quantity represents the injection function that one should correct in order to obtain the target wave excitation. We will use this function in the following section when describing the derivation of the classical prescription for exact time reversal.

3.2 Classical PIF

We are now ready to establish the PIF procedure for a classical wave equation. We will profit of the Green's function strategy developed in the previous chapter. In order to focus in a situation with a traditional interest for acoustics, we will consider a Helmholtz resonator coupled to an acoustic waveguide. We will model this situation as an inhomogeneity in the system of coupled oscillators [Rub63, CPa06]. Here, the lowest frequency ω_0 of the $\lambda/2$ mode in the resonator is represented by a single mass m_0 and its corresponding spring. The waveguide is modelled by a semi-infinite chain of identical masses $m = \alpha m_0$ placed at the equilibrium points $x_n = na$ and the nearest neighbor spring constant is $K = m\omega_{\mathrm{x}}^2$. This system can be faithfully represented as in Fig.3.3a, where we consider the longitudinal movement of the resonator and the masses of the waveguide. According to Eq. (3.12), the equations of motion for the corresponding displacements u_n are completely analogous to the vertical propagation considered before. These can be written in a matrix form which, in the frequency domain, reads:

$$\mathbb{D}^{-1}(\omega)\mathbf{u}(\omega) = \begin{pmatrix} \omega^2 - \tilde{\omega}_0^2 & \alpha\omega_{\mathrm{x}}^2 & \cdots \\ \omega_{\mathrm{x}}^2 & \omega^2 - 2\omega_{\mathrm{x}}^2 & \\ \vdots & & \ddots \end{pmatrix} \begin{pmatrix} u_0(\omega) \\ u_1(\omega) \\ \vdots \end{pmatrix} = 0, \tag{3.21}$$

where $\tilde{\omega}_0^2 = \omega_0^2 + \alpha\omega_{\mathrm{x}}^2$. Here, the diagonal elements of the resolvent have a simple expression in terms of continued fractions (see Appendix A). In particular, the response function for a single transducer placed at the site x_s on the waveguide is

$$D_{s,s}(\omega) = \frac{1}{\omega^2 - 2\omega_{\mathrm{x}}^2 - \Delta_{\mathrm{in}}(\omega) - [\Delta_{\mathrm{out}}(\omega) - \mathrm{i}\omega\eta(\omega)]}. \tag{3.22}$$

Here, the mean-field frequency $2\omega_{\mathrm{x}}^2$ appears shifted by the dynamical effect $\Delta(\omega)$ from the oscillators at both sides of x_s. The imaginary frequency shift indicates that different

components of excitation would eventually escape through the waveguide at the right with the different group velocities

$$v_g(\omega) = a\eta(\omega) = a\omega_{\mathrm{x}}\sqrt{1-\left(\frac{\omega}{2\omega_{\mathrm{x}}}\right)^2}, \tag{3.23}$$

in agreement with Eq. (3.7). The propagation of an excitation originated in the resonator at x_0 is detected at the transducer in the waveguide at x_s. The recorded signal presents a strong component in $\tilde{\omega}_0$, which is the "carrier" frequency as could be appreciated from the density of states at the resonator's site. The displacement at the transducer, resulting from an initial displacive force in the resonator, can be expressed as

$$u_s(t) = G_{s,0}(t)\Delta u_0, \qquad t \geq 0. \tag{3.24}$$

We seek the injection function $\delta u_s(t)$ that produces the exact reversion of the original wave within the control region. According to the external prescription discussed in Sec. 2.1 of the previous chapter, the perfect time reversal is possible whenever the dynamics starts and ends up without any excitation inside the cavity. Even when our system starts with an excited cavity, the lack of momentum ensures that the forward and backward evolutions[1] are symmetric respect to the focalization time. Once the decay signal is registered at the transducer for positive times, the subsequent propagation that takes place after the focalization is also known and we build the function to be corrected as

$$u_s^{\mathrm{rev}}(t) = \begin{cases} u_s(2t_R - t), & t_R \leq t \leq 2t_R \\ u_s(t - 2t_R), & t > 2t_R \end{cases}. \tag{3.25}$$

Thus, the injection that produces the desired reversion can be obtained from Eq. (3.20) as

$$\delta u_s^{\mathrm{PIF}}(\omega) = \frac{u_s^{\mathrm{rev}}(\omega)}{G_{s,s}(\omega)}. \tag{3.26}$$

Although such filter could be implemented through the direct construction of the complete evolution, we proceed as in the internal PIF (see Sec. 2.3) in order to test the relation with the group velocity. Thus, according to Eq. (2.45), the complete evolution writes in the frequency domain as

$$\begin{aligned} u_s^{\mathrm{rev}}(\omega) &= e^{\mathrm{i}\omega 2t_R}\left[u_s^*(\omega) + u_s(\omega)\right] && (3.27)\\ &= e^{\mathrm{i}\omega 2t_R}\left[G_{s,0}^*(\omega) + G_{s,0}(\omega)\right]\Delta u_0. && (3.28) \end{aligned}$$

Here again, the key tool is the use of a Dyson equation connecting the two subspaces delimited by the transducer. It allows us to relate the backward propagation given by $G_{s,0}(\omega)$ in terms of the detected wave that carries the conjugate $G_{s,0}^*(\omega)$

$$G_{s,0}(\omega) = \frac{G_{s,s}(\omega)}{G_{s,s}^*(\omega)} G_{s,0}^*(\omega), \tag{3.29}$$

[1] As in the direct time evolution, the forward propagation corresponds to the detected signal and the backward one consists on the remaining excitation after the focalization.

and the PIF injection rewrites

$$\delta u_s^{\mathrm{PIF}}(\omega) = e^{\mathrm{i}\omega 2t_R}\left[\frac{1}{G_{s,s}(\omega)} + \frac{1}{G^*_{s,s}(\omega)}\right] u_s^*(\omega) \tag{3.30}$$

$$= \frac{e^{\mathrm{i}\omega 2t_R}}{\mathrm{i}\omega}\left[\frac{1}{D_{s,s}(\omega)} - \frac{1}{D^*_{s,s}(\omega)}\right] u_s^*(\omega) \tag{3.31}$$

$$= e^{\mathrm{i}\omega 2t_R}\eta(\omega)u_s^*(\omega). \tag{3.32}$$

As in the quantum case, we denote by $2\omega_{\mathrm{x}}u_s^*(\omega)$ as the Fourier transform $\delta u_s^{\mathrm{TRM}}(\omega)$ of the injection function in the TRM protocol. In consequence, the perfect time reversal is obtained only once a further filter $v_g(\omega)/v_{\max}$ is applied. Hence, the PIF formula for internal source in the acoustic case is

$$\delta u_s^{\mathrm{PIF}}(\omega) = \frac{v_g(\omega)}{v_{\max}}\delta u_s^{\mathrm{TRM}}(\omega), \tag{3.33}$$

with $v_{\max} = a\omega_{\mathrm{x}}$ the group velocity in the center of the band and the focalization time is redefined as the origin of time.

This equation defines the perfect inverse filter for a classical wave, where the injection prescribed by the TRM procedure appears now corrected by the group velocity. Notably, the prescription remains exactly the same as that of the quantum version. This implies that the effectiveness of the filter will depend on the structure of the waveguide and the initial wave packet, regardless the details of the cavity. Notice that for cases in which the group velocity in the free space is constant[2], it results $\delta u_s^{\mathrm{PIF}}(\omega) = \delta u_s^{\mathrm{TRM}}(\omega)$.

The reconstruction of the initial excitation was numerically performed using the Pair Partitioning method, which yields the complete dynamics by alternating among the evolutions of pairs of coupled masses. We shall describe in detail the derivation of the method in Sec. 3.3. Since the recording time t_R is longer than the typical decay in the whole cavity, we can assume that all the masses in the control region have recovered their equilibrium positions once we start with the emission stage.

As we show in Fig. 3.3, the time reversal recovering is best depicted by analyzing the local energy

$$E_0(t) = \frac{p_0^2(t)}{2m_0} + \frac{m_0\tilde{\omega}_0^2}{2}u_0^2(t), \tag{3.34}$$

which avoids the fast fluctuations present in the displacement and momentum amplitudes. Here, the left panel shows (in a logarithmic scale) the recovering of the local energy in the resonator. As we can observe, the PIF coincides with the exact reversal over all the relevant times. Since in this model the waveguide has a cut-off frequency, as would be the case in a periodic waveguide, the PIF filter improves the TRM focusing when it comes to reproduce low intensity signals. This is particularly evident in the time reversed *survival collapse*: a sudden dip in the local energy resulting from the interference between the excitation surviving in the resonator and that returning from the waveguide. This

[2]That would be the case of a homogeneous waveguide where $v_g = c$.

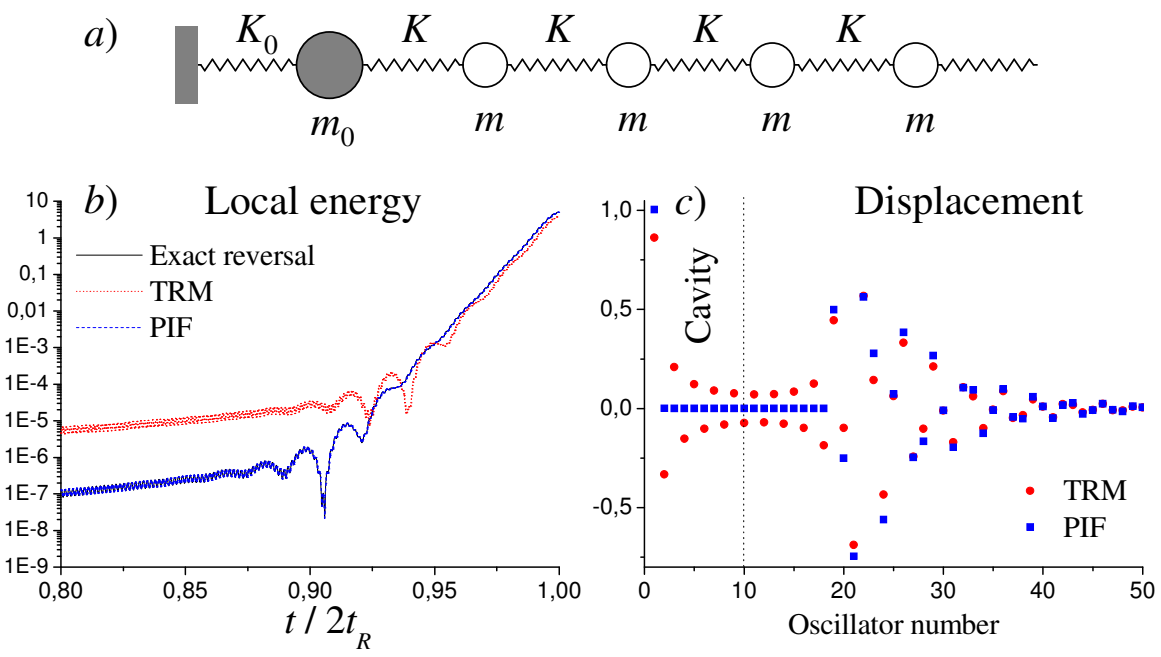

Figure 3.3: a) Harmonic model for a Helmholtz resonator coupled to a waveguide. b) Local energy recovered as function of time. Both methods, the TRM (red dotted) and PIF (blue dashed) are contrasted with the exact reversal (black solid). PIF and exact curves coincide for the whole period. c) Displacement distribution at the focalization time.

surprising phenomenon was originally described in the context of quantum spin channels [RFP06]. The perfect contrast of the time reversed signal provided by PIF is evidenced in the right panel by the exact cancellation of displacements except for the resonator. It is also interesting to notice that both procedures produce a phantom signal outside the "silence region". While the TRM has an evident imperfection in the localization of the signal, the PIF procedure yields this absolute cancellation even outside the cavity region defined by the far field transducer at x_s. The resulting localization, which corresponds to $\lambda/2$ of the carrier signal, was only enabled by filtering out the band edge components in the emitted signal. From this perspective, the PIF procedure constitutes a contribution to the goal of achieving the focusing energy beyond the diffraction limit [LRT07].

3.2.1 PIF in a two-dimensional membrane

The extension of the PIF procedure in multi-dimensional systems with a set of transducers constitutes a straightforward derivation of that described in the quantum case. We will work on the internal case where the initial excitation is already inside the cavity. For such purpose, one can write the detected displacements in the array of transducers as

that given by the general force

$$\mathbf{F}_A(t) = \mathbf{m}^{\mathbf{T}}\ \mathbb{I}\ \left[\Delta\mathbf{u}_A(0)\frac{\mathrm{d}}{\mathrm{d}t}\delta(t) + \Delta\dot{\mathbf{u}}_A(0)\delta(t)\right], \tag{3.35}$$

and hence, it may be expressed in terms of the resolvent operator

$$\mathbf{u}_S(t) = \mathbb{D}_{S,A}(t)\left[\mathrm{i}\omega\Delta\mathbf{u}_A(0) + \Delta\dot{\mathbf{u}}_A(0)\right],\ t \geq 0, \tag{3.36}$$

where, as always, S denotes the set of transducers at the equilibrium positions $\mathbf{s}_i$ and A refers to the cavity region. As we expect to reproduce the perfect reversal, the time evolution for the subsequent times would include the inversion of the velocities at the focalization time. Therefore, following the same arguments as before, the reversed evolution in the emission period $t_R \leq t \leq 2t_R$ reads

$$\mathbf{u}_S^{\mathrm{rev}}(t) = \int_0^t \mathrm{d}t'\mathbb{G}_{S,S}(t-t')\delta\mathbf{u}_S^{\mathrm{PIF}}(t') = \mathbf{u}_S(2t_R - t), \tag{3.37}$$

and the corresponding backward propagation that raise at the subsequent times $t > 2t_R$ is the evolution that follows the focalized excitation as

$$\begin{aligned}\mathbf{u}_S^{\mathrm{rev}}(t) &= \int_0^{2t_R} \mathrm{d}t'\mathbb{G}_{S,S}(t-t')\delta\mathbf{u}_S^{\mathrm{PIF}}(t') &(3.38)\\ &= \mathbb{D}_{S,A}(t-2t_R)\left[\mathrm{i}\omega\Delta\mathbf{u}_A(0) - \Delta\dot{\mathbf{u}}_A(0)\right], &(3.39)\end{aligned}$$

where the negative sign in $\Delta\dot{\mathbf{u}}_A(0)$ comes from the fact that the time reversal operation inverts the momenta of all the oscillators inside the cavity. In the frequency domain, the complete evolution resulting from the Fourier transform of the above evolutions yields

$$\mathbf{u}_S^{\mathrm{rev}}(\omega) = e^{\mathrm{i}\omega 2t_R}\left[\mathbb{D}_{S,A}(\omega) - \mathbb{D}_{S,A}^*(\omega)\right]\left[\mathrm{i}\omega\Delta\mathbf{u}_A(0) - \Delta\dot{\mathbf{u}}_A(0)\right], \tag{3.40}$$

where $\left[\mathbb{D}_{S,A}^*(\omega)\right]_{i,j} = D_{\mathbf{s}_i,\mathbf{a}_j}^*(\omega)$ is the complex conjugate without the transpose operation. Therefore, we use the Dyson recurrence by separating the space through a "perturbative" coupling between the outer region and the cavity. Again, if we assume that there is no damping processes that would include additional complex terms in the resolvent of the reduced basis A, the resolvent corresponding to the backward evolution can be replaced by

$$\mathbb{D}_{S,A}(\omega) = \mathbb{D}_{S,S}(\omega)\left[\mathbb{D}_{S,S}^{-1}(\omega)\right]^*\mathbb{D}_{S,A}^*(\omega), \tag{3.41}$$

and hence we obtain for the injection function

$$\delta\mathbf{u}_S^{\mathrm{PIF}}(\omega) = \frac{e^{\mathrm{i}\omega 2t_R}}{\mathrm{i}\omega}\mathbb{D}_{S,S}^{-1}(\omega)\mathbf{u}_S^{\mathrm{rev}}(\omega) = \frac{2e^{\mathrm{i}\omega 2t_R}}{\omega}\mathrm{Im}\mathbb{D}_{S,S}^{-1}(\omega)\mathbf{u}_S^*(\omega). \tag{3.42}$$

As we briefly mentioned before, it is interesting to note that only the detection and emission of either the displacement or velocity in the array of transducers is required.

Depending on what is the detected function and what is the emitted one, the above filter will change in a factor $\mathrm{i}\omega$ according to the following equations

$$\delta\mathbf{u}_S^{\mathrm{PIF}}(\omega) = \tfrac{2e^{\mathrm{i}\omega 2t_R}}{\omega}\mathrm{Im}\mathbb{D}_{S,S}^{-1}(\omega)\mathbf{u}_S^*(\omega), \tag{3.43}$$

$$\delta\mathbf{u}_S^{\mathrm{PIF}}(\omega) = \tfrac{2e^{\mathrm{i}\omega 2t_R}}{\mathrm{i}\omega^2}\mathrm{Im}\mathbb{D}_{S,S}^{-1}(\omega)\mathbf{v}_S^*(\omega), \tag{3.44}$$

$$\delta\mathbf{v}_S^{\mathrm{PIF}}(\omega) = -\mathrm{i}2e^{\mathrm{i}\omega 2t_R}\mathrm{Im}\mathbb{D}_{S,S}^{-1}(\omega)\mathbf{u}_S^*(\omega), \tag{3.45}$$

$$\delta\mathbf{v}_S^{\mathrm{PIF}}(\omega) = \tfrac{-2e^{\mathrm{i}\omega 2t_R}}{\omega}\mathrm{Im}\mathbb{D}_{S,S}^{-1}(\omega)\mathbf{v}_S^*(\omega). \tag{3.46}$$

The group velocities in the frontiers of the cavity play a significant role in the determination of the target function that enables for the exact reversal. If the outer region admits a decomposition in multi-channel waveguides, this dependence is easily obtained as in the quantum case, and the structure on the filter may imply an effective correction on the TRM procedure.

In the following numerical example we consider the PIF and TRM procedures in a two-dimensional lattice where the oscillations are allowed in the z direction as shown in the scheme of Fig. 3.4. The registration and emission is dealt by an array of $N_S = 4$ transducers pointed in the dotted rectangle of the scheme. Inside the cavity, an initial excitation (displacement and velocity) is set in the impurity with $m_0 = 4m$ and $\omega_0 = \omega_{\mathrm{x}}$. The corrective terms in Eq. (3.42) are obtained from the construction of the Green's function matrix in the time domain. For the j-th column in $\mathbb{G}_{S,S}(t)$ we register in all the transducers the resulting propagation that arrives from the initial displacement on the j transducer and so on. Thus, the inversion of the Green's function is performed in the frequency domain where

$$\frac{1}{\omega}\mathrm{Im}\mathbb{D}_{S,S}^{-1}(\omega) = \mathrm{Re}\mathbb{G}_{S,S}^{-1}(\omega). \tag{3.47}$$

Some illustrative elements of such inverse in Fig. 3.4 are presented and contrasted with their analytical expressions obtained from the same analysis given in Eq. (2.88). Here, the multi-channel decomposition writes

$$\mathrm{Re}\left[\mathbb{G}_{S,S}^{-1}\right]_{n,m} = \sum_{k=1}^{N_S} u_{nk}\eta(\omega^2 - \tilde{\omega}_k^2)u_{km}, \tag{3.48}$$

with

$$\tilde{\omega}_k^2 = 2\omega_{\mathrm{x}}^2 + 4\omega_{\mathrm{x}}^2\sin^2\left(\frac{k\pi/2}{N_S+1}\right), \tag{3.49}$$

the effective characteristic frequencies of the normal modes whose components are

$$u_{nk} = u_{kn} = \sqrt{\frac{2}{N_S+1}}\sin\left(\frac{nk\pi}{N_S+1}\right). \tag{3.50}$$

In the considered example, we found a gap in the correction terms between $-\omega_{\mathrm{x}}$ and ω_{x} due to the dimensionality of the lattice. In consequence, the filtered signal will not

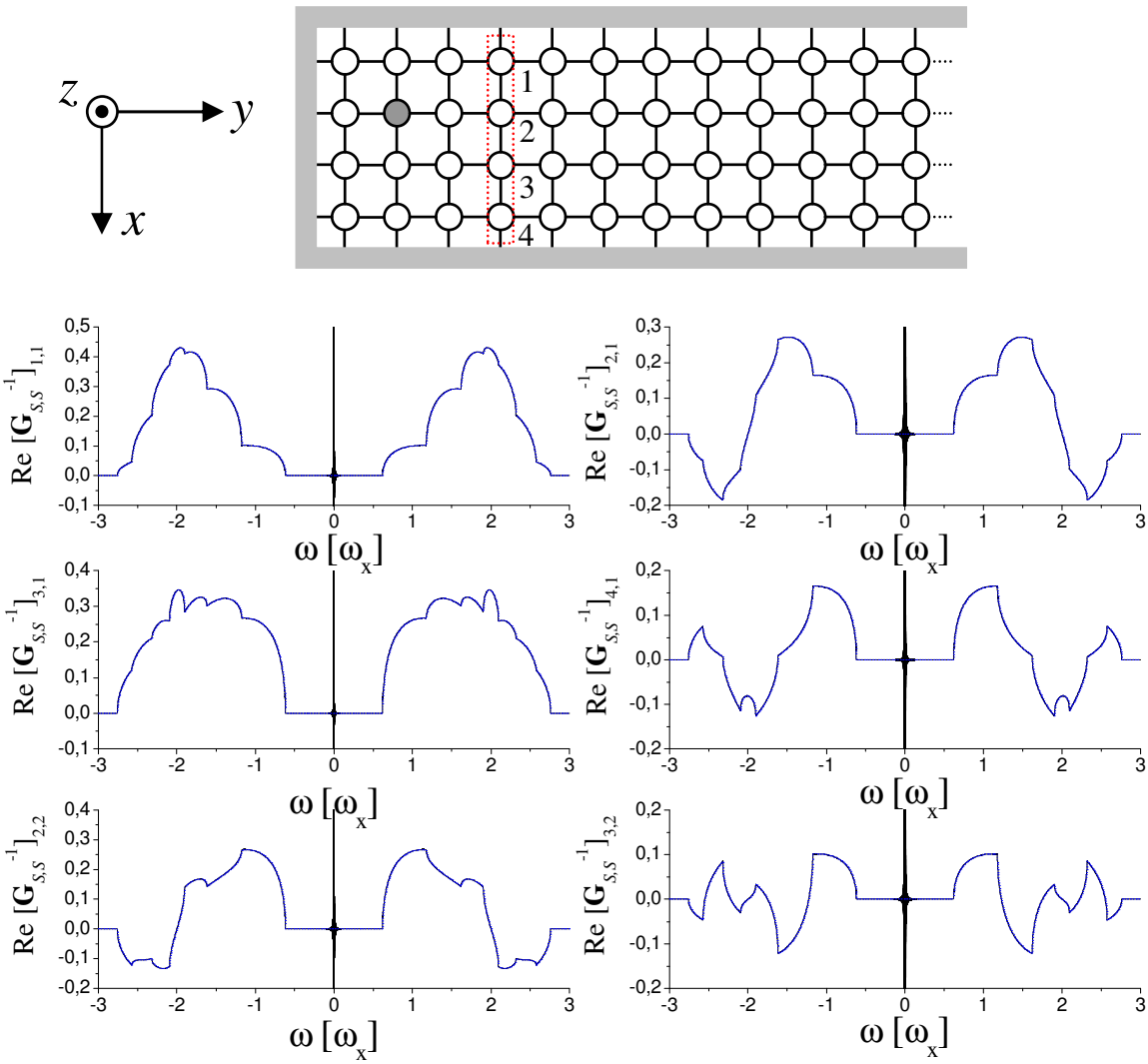

Figure 3.4: Top: scheme of the 2D harmonic lattice, the cavity, delimited by four transducers at the right, contains an impurity mass in the $(2, 2)$ site. Bottom: comparison between numerical (black solid) and analytical (blue dotted, superimposed) results on the PIF corrective terms.

contain these central energies as compared with the corresponding TRM injection. On the other hand, there is a mismatch between the numerical and analytical results near the center of the band $\omega \simeq 0$ due to the finite registration period. Since for long times the decay of the escaping waves follows a power law, it is hard to fully satisfy the condition $u_S(t_R) = 0$ in the direct calculus of the time evolution propagators and hence it appears as a localized component in the normal modes expansion.

The time reversed evolution (displacement and velocity) is computed for both procedures in the impurity mass and is shown in Fig. 3.5 for times close to the focalization

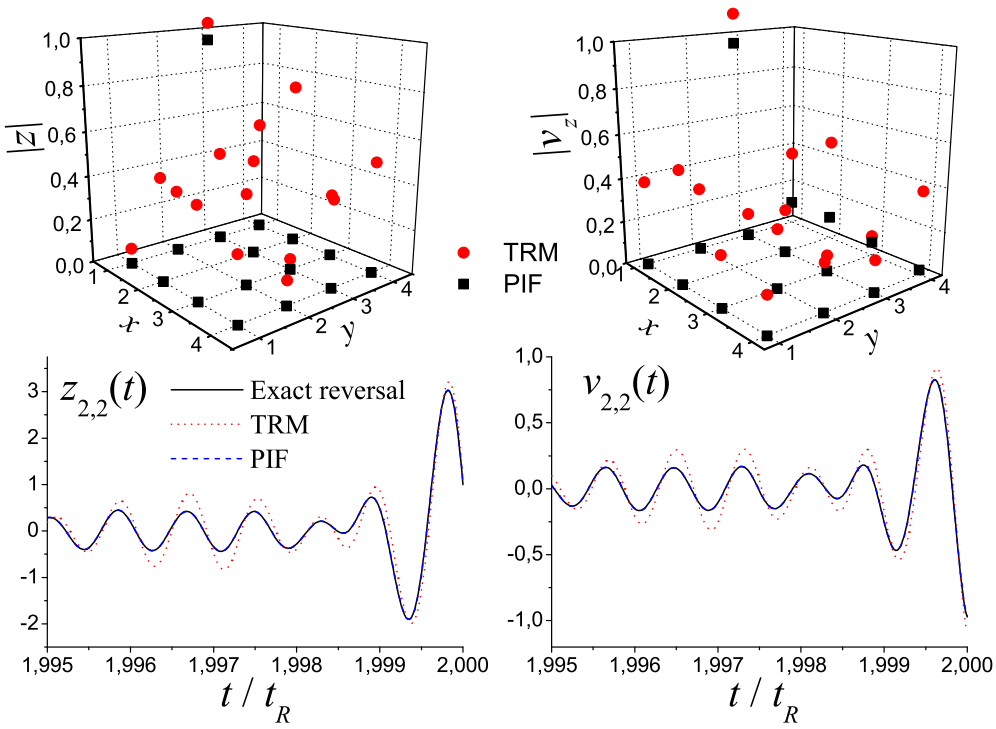

Figure 3.5: Recovering of the initial excitation. Top: spatial contrast in the focalized displacements (left) and velocities (right) for the TRM (red circles) and PIF (black squares) procedures. Bottom: time recovering of the displacement (left panel) and velocity (right) in the excited oscillator for the TRM (red dotted) and PIF (blue dashed). In black solid line we show the exact reversal for comparison.

(see bottom panels). Furthermore, the spatial contrast of the displacements and velocities inside the cavity is also computed in the top panels of the figure. As we can appreciate, the PIF coincides with the exact time reversed evolution and recovers the initial excitation. For the TRM, we observe strong differences with the ideal case in both the time and space reconstructions. The time reversed displacement and velocity maintain almost the same phase but present different oscillation amplitudes and, at the focalization time, all the oscillators are shifted from their equilibrium positions.

3.3 The Pair Partitioning method

The dynamical properties that concerns a discrete classical wave system can be obtained either through the diagonalization of the involved Hamiltonian or through the direct cal-

culation of the general propagator presented in Eq. (3.12). In this last case, one should compute the involved continued fractions in the frequency domain and then perform the corresponding inverse Fourier transform that yields the time dependence of the displacements and velocities of the oscillators. However, our focus here is to describe the time reversal operation as in the experimental procedures, *i.e.* we would like to obtain the wave amplitude as the signal that arrives to the transducer, and evaluate the Green's function as an emission and detection procedure. Because of this, we develop a numerical method, called the Pair Partitioning (PP), that enables a complete description of the dynamics within the time domain [CPa07]. Provided that the numerical integrator is stable and perfectly reversible, it represents a key issue in the evaluation the robustness of the reversal procedures. Additionally, we introduce a numerical recipe that approximates the solution of an infinite system through a finite one. For this last, a non-homogeneous fictitious "friction" term represents the diffusion of the excitation occurring in an unbounded system.

The considered system is that of Fig. 3.1: a one-dimensional harmonic chain where the i-th oscillator has a mass m_i and a natural frequency ω_i and is coupled to its nearest neighbors through the springs with elastic constants $K_{i-1,i}$ and $K_{i,i+1}$ respectively. This is a many-body problem not solvable analytically in a general context and which would involve a subtantial computational resources when doing a numerical solution. Besides, typical algorithms available, such as Runge-Kutta, do not warrant a perfect reversible dynamics. This last is a fundamental requirement if one seeks to test time reversibility. We may get inspiration from the Trotter method [Rae96] used in the quantum reversal procedures of the previous chapter. There, a good approximation to the overall dynamics was obtained by composing the analytical time reversible solutions of the equations of motion for each pair of coupled degrees of freedom in a time step τ. Now the idea would be to solve the coupled motion of pairs of particles. With this purpose we could rewrite the Hamiltonian of Eq. (3.8) in terms of each coupling by separating it as a sum of non-interacting terms including either even pairs or odd pairs as

$$H = H_1 + H_2 = H_{1,2} + H_{3,4} + \dots H_{2,3} + H_{4,5} + \dots . \tag{3.51}$$

Here, each elemental Hamiltonian takes the form

$$H_{i,i+1} = \frac{p_i^2}{2\tilde{m}_i} + \frac{\tilde{m}_i\tilde{\omega}_i^2}{2}u_i^2 + \frac{p_{i+1}^2}{2\tilde{m}_{i+1}} + \frac{\tilde{m}_{i+1}\tilde{\omega}_{i+1}^2}{2}u_{i+1}^2 + \frac{K_{i,i+1}}{2}\left(u_{i+1}-u_i\right)^2, \tag{3.52}$$

where the effective masses and natural frequencies satisfy

$$\tilde{m}_1 = m_1, \qquad \tilde{\omega}_1 = \omega_1, \qquad \tilde{m}_N = m_N, \qquad \tilde{\omega}_N = \omega_N, \tag{3.53}$$

$$\tilde{m}_i = 2m_i, \qquad \tilde{\omega}_i = \omega_i/2, \qquad i = 2, \dots, N-1. \tag{3.54}$$

Therefore, the equations of motion corresponding to the pair described in $H_{i,i+1}$ are

$$\ddot{u}_i = -\left(\tilde{\omega}_i^2 + \frac{K_{i,i+1}}{\tilde{m}_i}\right)u_i + \frac{K_{i,i+1}}{\tilde{m}_i}u_{i+1}, \tag{3.55}$$

$$\ddot{u}_{i+1} = -\left(\tilde{\omega}_{i+1}^2 + \frac{K_{i,i+1}}{\tilde{m}_{i+1}}\right)u_{i+1} + \frac{K_{i,i+1}}{\tilde{m}_{i+1}}u_i. \tag{3.56}$$

Since the equations of motion are solved separately, we can consider the system of two coupled oscillators, *e.g.*

$$\ddot{u}_1 = -\omega_1^2 u_1 + \omega_{12}^2 u_2, \ddot{u}_2 = -\omega_2^2 u_2 + \omega_{21}^2 u_1. \tag{3.57}$$

For this system, the corresponding time evolution operator $\mathbb{U}_{12}(\tau)$ relating the displacements and velocities in the basis $\{u_1, u_2, v_1, v_2\}$ is readily obtained as

$$\begin{pmatrix} \mathbf{u}(t+\tau) \\ \mathbf{v}(t+\tau) \end{pmatrix} = \begin{pmatrix} \mathbb{U}_u(\tau) & \mathbb{U}_v(\tau) \\ \mathbb{V}_u(\tau) & \mathbb{V}_v(\tau) \end{pmatrix} \begin{pmatrix} \mathbf{u}(t) \\ \mathbf{v}(t) \end{pmatrix} \tag{3.58}$$

with

$$\mathbb{U}_u(\tau) = \mathbb{V}_v(\tau) = \begin{pmatrix} \frac{\Omega_+^2 \cos(\tau_-) - \Omega_-^2 \cos(\tau_+)}{\Delta\omega^2} & \frac{\omega_{12}^2[\cos(\tau_-) - \cos(\tau_+)]}{\Delta\omega^2} \\ \frac{\omega_{21}^2[\cos(\tau_-) - \cos(\tau_+)]}{\Delta\omega^2} & \frac{\Omega_+^2 \cos(\tau_+) - \Omega_-^2 \cos(\tau_-)}{\Delta\omega^2} \end{pmatrix}, \tag{3.59}$$

$$\mathbb{U}_v(\tau) = \begin{pmatrix} \frac{\Omega_+^2 \omega_-^{-1} \sin(\tau_-) - \Omega_-^2 \omega_+^{-1} \sin(\tau_+)}{\Delta\omega^2} & \frac{\omega_{12}^2\left[\omega_-^{-1} \sin(\tau_-) - \omega_+^{-1} \sin(\tau_+)\right]}{\Delta\omega^2} \\ \frac{\omega_{21}^2\left[\omega_-^{-1} \sin(\tau_-) - \omega_+^{-1} \sin(\tau_+)\right]}{\Delta\omega^2} & \frac{\Omega_+^2 \omega_+^1 \sin(\tau_+) - \Omega_-^2 \omega_-^{-1} \sin(\tau_-)}{\Delta\omega^2} \end{pmatrix}, \tag{3.60}$$

$$\mathbb{V}_u(\tau) = \begin{pmatrix} \frac{\Omega_-^2 \omega_+ \sin(\tau_+) - \Omega_+^2 \omega_- \sin(\tau_-)}{\Delta\omega^2} & \frac{\omega_{12}^2[\omega_+ \sin(\tau_+) - \omega_- \sin(\tau_-)]}{\Delta\omega^2} \\ \frac{\omega_{21}^2[\omega_+ \sin(\tau_+) - \omega_- \sin(\tau_-)]}{\Delta\omega^2} & \frac{\Omega_-^2 \omega_- \sin(\tau_-) - \Omega_+^2 \omega_+ \sin(\tau_+)}{\Delta\omega^2} \end{pmatrix}. \tag{3.61}$$

Here, $\omega_\pm^2$ are the characteristic frequencies

$$\omega_\pm^2 = \frac{\omega_1^2 + \omega_2^2}{2} \pm \sqrt{\left(\frac{\omega_1^2 - \omega_2^2}{2}\right)^2 + \omega_{12}^2 \omega_{21}^2}, \tag{3.62}$$

and

$$\tau_\pm = \omega_\pm \tau, \qquad \Omega_\pm^2 = \omega_\pm^2 - \omega_1^2, \qquad \Delta\omega^2 = \omega_+^2 - \omega_-^2. \tag{3.63}$$

At each small time step $\tau \ll \omega_{\mathrm{x}}^{-1}$, the evolution for the even couplings is obtained and the resulting displacements and velocities are used as the initial conditions for the odd couplings and so on. This gives the complete time step operator as

$$\mathbb{U}_{\mathrm{PP}}(\tau) = \mathbb{U}_2(\tau)\mathbb{U}_1(\tau), \tag{3.64}$$

and can be summarized in the Pair Partitioning algorithm:

1. Determine all the masses and natural frequencies of the partitioned system $\tilde{m}_n, \tilde{\omega}_n$.
2. Calculate the corresponding characteristic frequencies $\omega_\pm$ and compute the 4×4 evolution operator for every coupling on the system.
3. According to the initial displacements and velocities $\{u_i(0), v_i(0)\}$, calculate the time step evolution in the odd couplings through the operators $\mathbb{U}_{12}(\tau), \mathbb{U}_{23}(\tau), \ldots$.

4. Use the obtained values $\{\tilde{u}_i(\tau), \tilde{v}_i(\tau)\}$ as the initial displacements and velocities in the time step calculation for the even couplings and compute $\{u_i(\tau), \dot{u}_i(\tau)\}$.

5. Return to the step 3 with $\{u_i(\tau), \dot{u}_i(\tau)\}$.

Therefore, by applying the PP algorithm n times we solve the displacements and velocities for all oscillators in the whole period $0 < t < n\tau$.

As an example, we consider the homogeneous system where the N oscillators have identical masses and the surface oscillators are coupled to fixed points yielding the natural frequencies $\omega_1 = \omega_N = \omega_x = \sqrt{K/m}$. The displacement amplitude of the i-th oscillator due to an initial displacement in the j-th oscillator can be calculated analytically as

$$u_{i\leftarrow j}(t) = \frac{2}{N+1}\sum_{k=1}^{N} \sin\left(\frac{ik\pi}{N+1}\right)\sin\left(\frac{jk\pi}{N+1}\right)\cos(\omega_k t)u_j(0), \tag{3.65}$$

with

$$\omega_k = 2\omega_x \sin\left(\frac{k\pi}{2(N+1)}\right), \tag{3.66}$$

the characteristic frequency for the k-th normal mode.

We can test the accuracy of the method by considering an initial situation in which all the oscillators are in their equilibrium positions except for the first one. If $u_1(0) = u_0$ is the initial displacement, the relative error

$$\varepsilon(t) = \frac{\left|u_1(t) - u_1^{\mathrm{PP}}(t)\right|}{u_0}, \tag{3.67}$$

accounts for the difference between the analytical and numerical evolutions of the displacement of the first oscillator. We use a chain of $N = 200$ oscillators for several values of the time step going from $\tau = 0.001\omega_x^{-1}$ until $\tau = 0.01\omega_x^{-1}$ and take the maximum value of the above error.

As we can see from Fig. 3.6, the error drops as the temporal step τ diminishes. We observe also a quadratic dependence $\max\ \varepsilon(t) = \alpha\tau^2$ in complete analogy with the Trotter method. In the particular case of the homogeneous system, the obtained coefficient results $\alpha \simeq 0.0445$. Furthermore, we taken N enough large such that no mesoscopics echoes [PLU95] appear in the interval of time shown in the inset.

Note that here, as a consequence of the separation in the Hamiltonian, the total energy is not exactly conserved but fluctuates with an amplitude ΔE around the ideal conserved value. Since ΔE is proportional to τ^2, it becomes negligible for typical cases where $\tau \simeq 0.01\omega_x^{-1}$.

3.3.1 Unbounded systems as damped oscillations

The solution of wave dynamics in an infinite medium remains as a delicate issue. In such case, the initially localized excitation spreads away through the system. If one

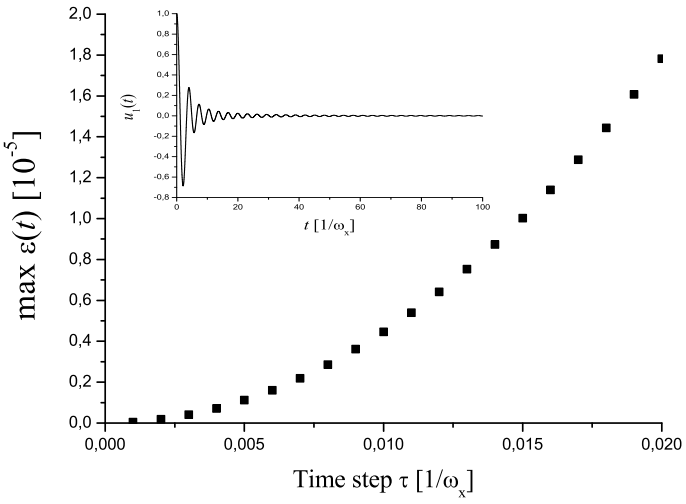

Figure 3.6: Relative errors in the PP method for different time step values. Inset: analytical evolution of the surface oscillator displacement.

measures the amount of remaing energy in a given region of the space, one would see that it decays with a power law that depends on the dimensionality of the system. In a local perspective, this decay resembles what happens in presence of friction, where energy decays exponentially. In contrast, finite conservative systems present periodic revivals, known as mesoscopic echoes, manifesting the fact that the energy remains in the system. In a practical computational set up one needs to restrict the calculations to a finite number of oscillators and still one would like to describe a form of "escape" or energy loss that gets rid of the mesoscopic echoes. With this purpose we add a fictitious "damping" region where frictional forces grow from zero to very strong values as the oscillators approach to the boundaries. The friction coefficients η_i can be included between the third and fourth steps of the PP algorithm by imposing an exponential decay of the displacement amplitude as

$$u_i(t) \leftarrow u_i(t) \exp(-\eta_i \tau). \tag{3.68}$$

As occurs in an underdamped oscillator in the limit $\eta/\omega_{\mathrm{x}} \ll 1$, the effective frequency remains almost the same. Hence, we choose a progressive increasing in the damping terms as a linear function of the position

$$\eta_i = \alpha \frac{i - x_R}{N - x_R}, \qquad i = x_R, \ldots, N. \tag{3.69}$$

It is clear that the determination of these values constitutes by itself a subtle operation. This is because one wants to avoid, in addition to the mesoscopic echoes, the reflections due to mismatching inside the damping zone. Therefore, the value of the slope $\alpha(N - x_R)^{-1}$

has to be small as compared with ω_x in order to ensure adiabaticity. On the other hand, final damping has to be important, say a fraction of ω_x, so the surface effects can not propagate to the interior region. In this last case the localization length $\xi = a/\sinh^{-1}[\alpha/\omega_x]$ extends for a few lattice constants a.

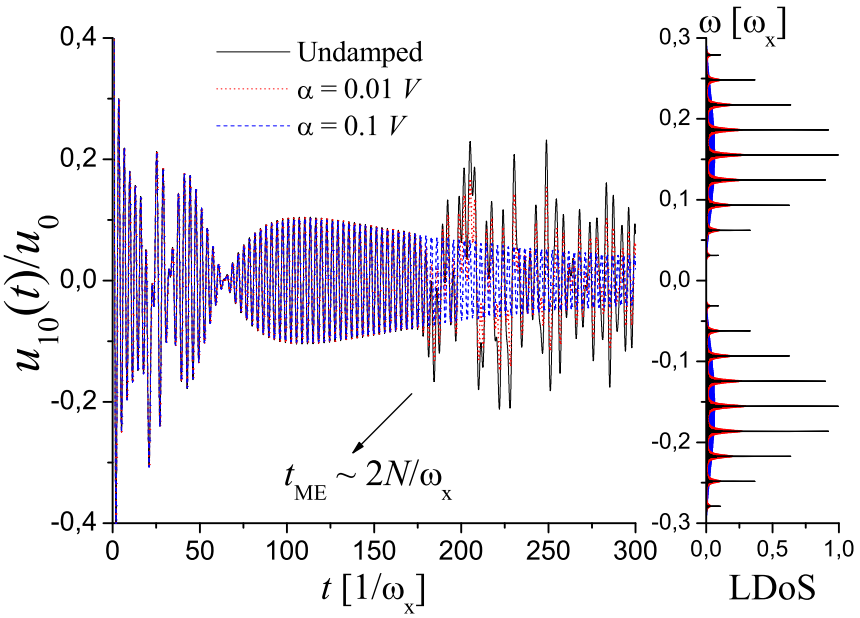

Figure 3.7: Left panel: comparison between the undamped (black solid) and the damped evolutions with $\alpha = 0.01$ (red dotted) and $\alpha = 0.1$ (blue dashed). Right panel: corresponding local density of states for the mentioned systems. For a better visualization, the area under the curve is plotted.

For the previous homogeneous system with $N = 200$ oscillators we will assume that the cavity ends at the site $x_R = 10$. We compare the displacement amplitude in x_R for the undamped case with two dampings $\alpha = 0.01$ and $\alpha = 0.1$. In the left panel of Fig. 3.7 is shown the dynamics in the undamped system (black solid) presenting the mesoscopic echo around the time $t_M \simeq 2N\omega_x^{-1}$. For the damped systems, we observe that the echo still survives for $\alpha = 0.01$ (red dotted) and finally vanishes for $\alpha = 0.1$ (blue dashed). In the right panel are displayed the real parts of the Green's functions as indicative of the local density of states in x_R

$$J_R(\omega) = -\frac{1}{\pi}\omega \text{ Im } D_{R,R}(\omega) \tag{3.70}$$

$$= -\frac{1}{\pi}\text{Re } G_{R,R}(\omega) \tag{3.71}$$

Here, we can see how the structure associated to the system without friction is lost as we increase the value of α and, finally, the typical density of the infinite system is recovered.

3.4 Summary

To sum up, we designed a novel procedure that achieves the exact reversal in the classical wave dynamics. This was achieved in the discrete form of the classical wave equation, modeled through a harmonic chain of coupled oscillators. Here, the displacements and velocities of the oscillators were obtained as a solution to the equation of motion that arises from the discrete wave equation. The solution to this equation was expressed as the position-momentum response of the oscillators to an instantaneous impulsive force that sets the initial momentum. The corresponding position-position response was then deduced through a displacive force that yields the initial position and both responses (*i.e.* the classical Green's functions) were related. This allowed us to solve the time reversal dynamics by following the same scheme of Chapter 2 and derive the classical PIF.

In the internal source case, where the internal excitation is either created inside the cavity or results from a well resolved incoming wave, we found as in the quantum PIF, that the prescription corrects the TRM through factors containing the group velocities in the transducers, regardless the internal feedback of the cavity. In this classical case where the propagation obeys a linear dispersion, the group velocity is essentially the speed of sound. Therefore, the resulting PIF filter remains as a constant prefactor and the TRM achieves the exact reversal. However, periodicity or scattering due to inhomogeneities in the outer region would give a nontrivial structure in the frequency dependence of such velocities. For these cases, the PIF correction will improve the TRM procedure and may constitute a powerful tool in the focalization of classical waves. In particular, the PIF correction could provide a direct improvement over the experiments done in the focusing of elastic waves [MPN07, CBB08].

Additionally, we developed a novel numerical technique, the pair partitioning method, that faithfully reproduces the propagation of acoustic waves in harmonic lattices. The method showed to be perfectly reversible and the propagation in boundless systems, required for the PIF prescription, can be easily reproduced in terms of finite systems where the oscillators near the boundaries carry damping processes.

Chapter 4

Semiclassical time reversal focusing

As we have shown in the last two chapters, the PIF prescription corrects the TRM in order to ensure an exact reversed dynamics. This result was obtained in both quantum and classical discrete systems, that enabled a clear separation between the cavity and the outside regions. Now that we have a formal prescription that achieves the perfect reversal, we seek for the stability of the TRM procedure in cases where the conditions for exact reversal are not completely fulfilled. As an example of such situation, consider the TRM experiments in closed chaotic cavities where the excitations persist over time without decaying. Here, a single transducer is enough to perform the desired time reversal [DFi97]. A prominent feature is that, the refocusing improves with the chaoticity of the cavity. While various analytical techniques were employed to attempt a description of these experiments, one may safely say that a conceptual explanation is still lacking. As antecedents we may mention an analysis of wave fields in the momentum-space representation (Wigner's transform) that has been used to understand how multiple scattering enhances the spatial resolution of the refocused signal [BRy03]. Diagrammatic perturbation theory has been able to account for the symmetry-induced interference enhancements in the refocalization observed in disordered media [RTD04]. The strategies proper of control theory are natural but do not contribute much to the understanding [BFi02]. Finally, the contrasting stability properties of TRM with wave and particle propagation through a multiple scattering medium has been addressed in Ref. [SSc98], without reaching a definite conclusion.

In this chapter, we present a detailed calculation of the focalization amplitude that is obtained through the TRM procedure for times close to the expected refocusing and positions near the source point where the recovering takes place. We use the semiclassical approach to quantify the quality of the reconstructed signal in terms of temporal and spatial extensions. Besides, we obtain the scaling of the focalization amplitude with the temporal emission interval in order to compare with the experimental and numerical results for the time reversal of elastic waves [DFi97].

We start by introducing the propagators that are involved in the calculus of the focalization amplitude as an expansion in their related classical trajectories according to the semiclassical approximation. Thus, by a detailed evaluation of the weights of each

trajectory, we integrate over all possible paths and obtain the scaling of the resulting focalization amplitude with the recording/emission interval. We begins with the most simple case where the original excitation has no initial momentum and evaluates the maximum of the focalization in the focal point, *i.e.* the center of the original wave packet, at the refocusing time. The spatial and temporal extensions of this focalization follows a straightforward algebra and yield the resulting reversed propagation. Moreover, we re-obtain the scaling of the focalization through an alternative strategy that assumes an ergodic cavity and performs an average over the phase-space. Finally, we validate our analytical results confronting them numerically in a two-dimensional chaotic stadium.

4.1 Semiclassical expansion of the quantum TRM

A time reversal mirror experiment starts with a high frequency signal emitted at $t = 0$ at the position $\mathbf{r}_0$ inside the cavity. Such excitation can be interpreted within the ray picture as an initial wave packet $\psi_{\mathbf{p}_0}(\mathbf{r}) = \langle \mathbf{r} | \, \psi_{\mathbf{p}_0}(t = 0) \rangle$ centered around $\mathbf{r}_0$ and with momentum $\mathbf{p}_0$ that evolves and is recorded by a transducer (or an array of them) at position(s) $\mathbf{r}_i$ $(i = 1, 2, \ldots, N)$ for times within the interval (t_1, t_2). Then, the signal detected by the transducer for times $t > t_1$ is

$$\psi(\mathbf{r}_i, t) = \int_{\mathcal{A}} \mathrm{d}\mathbf{r}' K(\mathbf{r}_i, \mathbf{r}', t) \psi_{\mathbf{p}_0}(\mathbf{r}'), \tag{4.1}$$

with $\mathcal{A}$ the area (volume) of the cavity and

$$K(\mathbf{r}_i, \mathbf{r}', t) = \mathrm{i}\hbar G(\mathbf{r}_i, \mathbf{r}', t) = \langle \mathbf{r}_i | \, e^{-\mathrm{i}\mathbf{H}t/\hbar} \, | \mathbf{r}' \rangle \,, \tag{4.2}$$

is the quantum propagator describing the time evolution of the wave from $\mathbf{r}'$ to $\mathbf{r}_i$ in the time $t > 0$. The recording process takes a period ΔT and finally ends up at the time $t_2 = t_1 + \Delta T$. Thus, after a waiting time $t_R > t_2$, the recorded signal is reversed and emitted during the subsequent interval between $t_2' = 2t_R - t_2$ and $t_1' = 2t_R - t_1$. The injected wave propagates from the transducer and interferes constructively in the focal region, giving rise to the refocusing of the original excitation. Once the emission has finished $(t > t_1')$, the signal detected in the source region, defined as the focalization amplitude, can be computed as

$$\begin{aligned} \mathcal{F}_{\mathbf{p}_0}(\mathbf{r}, t) &= \int_{t_2'}^{t_1'} \mathrm{d}\tau K(\mathbf{r}, \mathbf{r}_i, t - \tau) \chi^{\mathrm{TRM}}(\mathbf{r}_i, \tau) & (4.3) \\ &= \int_{t_2'}^{t_1'} \mathrm{d}\tau K(\mathbf{r}, \mathbf{r}_i, t - \tau) \int_{\mathcal{A}} \mathrm{d}\mathbf{r}' K^*(\mathbf{r}_i, \mathbf{r}', 2t_R - \tau) \psi^*_{\mathbf{p}_0}(\mathbf{r}'), & (4.4) \end{aligned}$$

where the TRM injection is the time reversal of the detected signal. In order to get a focalization that scales as a wave function, the injection should account for an additional constant factor like the $2V/\hbar$ used in the second chapter. The focusing is expected at

$2t_R$, which is redefined as the time origin [DFi97], and is schematically shown in Fig. 4.1. Performing the change in the integration variable as $\tau \to 2t_R - \tau$, we obtain [TSo07]

$$\mathcal{F}_{\mathbf{p}_0}(\mathbf{r}, t) = \int_{t_1}^{t_2} \mathrm{d}\tau K(\mathbf{r}, \mathbf{r}_i, t + \tau) \int_{\mathcal{A}} \mathrm{d}\mathbf{r}' K^*(\mathbf{r}_i, \mathbf{r}', \tau) \psi^*_{\mathbf{p}_0}(\mathbf{r}'). \tag{4.5}$$

The propagator $K(\mathbf{r}, \mathbf{r}_i, t + \tau)$ corresponds to the re-emitted signal, which is obtained by time reversing the evolution of the initial state with the propagator $K^*(\mathbf{r}_i, \mathbf{r}', \tau)$. We do not write the initial temporal arguments of the propagators, as they are taken to be 0.

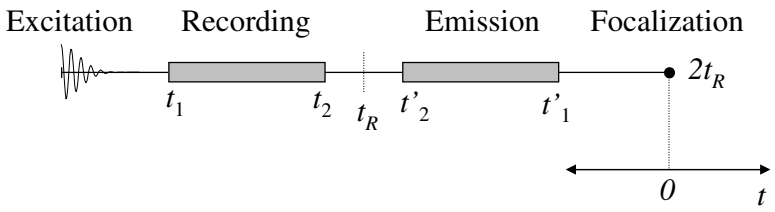

Figure 4.1: Scheme of the involved times in the TRM sequence.

Working in two-dimensional systems, the initial excitation can be faithfully represented by a Gaussian wave packet

$$\psi_{\mathbf{p}_0}(\mathbf{r}') = \frac{1}{\sqrt{\pi}\sigma} \exp\left[\frac{\mathrm{i}}{\hbar}\mathbf{p}_0 \cdot (\mathbf{r}' - \mathbf{r}_0) - \frac{(\mathbf{r}' - \mathbf{r}_0)^2}{2\sigma^2}\right], \tag{4.6}$$

centered around $\mathbf{r}_0$ and with dispersion σ. The initial momentum $\mathbf{p}_0$ gives the main energy and direction of the excitation. In the semiclassical approximation, the propagator can be expanded as a sum over classical trajectories $s(\mathbf{r}', \mathbf{r}, \tau)$ linking the points $\mathbf{r}'$ and $\mathbf{r}$ in a time τ [BBh97],

$$K(\mathbf{r}, \mathbf{r}', \tau) \simeq \sum_{s(\mathbf{r}', \mathbf{r}, \tau)} K_s(\mathbf{r}, \mathbf{r}', \tau), \tag{4.7}$$

according to the Van Vleck's formula[1]

$$K_s(\mathbf{r}, \mathbf{r}', \tau) = \frac{1}{2\pi\mathrm{i}\hbar} C_s^{1/2} \exp\left[\frac{\mathrm{i}}{\hbar} S_s(\mathbf{r}, \mathbf{r}', \tau) - \frac{\mathrm{i}}{2}\pi\mu_s\right]. \tag{4.8}$$

Here, $S_s(\mathbf{r}, \mathbf{r}', \tau)$ denotes the action as the time integral of the Lagrangian $\mathcal{L}$

$$S_s(\mathbf{r}, \mathbf{r}', \tau) = \int_0^\tau \mathrm{d}t \; \mathcal{L}_s(\mathbf{r}_s(t), \dot{\mathbf{r}}_s(t); t), \tag{4.9}$$

over the classical path s. The Maslov index μ_s accounts for the number of conjugates points along s. In the diagonal approximation taken here, this factor vanishes since it

[1] Actually, it was Gutzwiller who later added the Maslov index μ_s [HTS92].

appears in both propagators and hence we can neglect it. The Jacobian $C_s = |\det(\mathbb{B}_s)|$ acts as the stability factor that sets the weight of the s-th trajectory with

$$[\mathbb{B}_s]_{n,m} = -\frac{\partial^2 S_s}{\partial \mathbf{r}_n \partial \mathbf{r}'_m}, \tag{4.10}$$

the derivatives of the action with respect to the components of the initial and final positions.

Since we assume a highly localized initial wave packet in the source point $\mathbf{r}_0$, we can expand the action integral in terms of those slightly modified trajectories $\tilde{s}$ departing from the center of the wave packet and reaching $\mathbf{r}_i$ in a time τ as

$$\begin{aligned} S_s(\mathbf{r}_i, \mathbf{r}', \tau) &\simeq S_{\tilde{s}}(\mathbf{r}_i, \mathbf{r}_0, \tau) + \frac{\partial}{\partial \mathbf{r}'} S_s(\mathbf{r}_i, \mathbf{r}', \tau)\Big|_{\mathbf{r}'=\mathbf{r}_0} \cdot (\mathbf{r}' - \mathbf{r}_0), & (4.11)\\ &= S_{\tilde{s}}(\mathbf{r}_i, \mathbf{r}_0, \tau) - \mathbf{p}_{\tilde{s}} \cdot (\mathbf{r}' - \mathbf{r}_0), & (4.12) \end{aligned}$$

with $\mathbf{p}_{\tilde{s}}$ the initial momentum of the trajectory $\tilde{s}$. Therefore, the detected signal at the transducer point takes the form [JPa01, GWR08]

$$\psi(\mathbf{r}_i, \tau) = \left(4\pi\sigma^2\right)^{1/2} \sum_{s(\mathbf{r}_0, \mathbf{r}_i, \tau)} K_s(\mathbf{r}_i, \mathbf{r}_0, \tau) \exp\left[-\frac{\sigma^2}{2\hbar^2} \left(\mathbf{p}_s - \mathbf{p}_0\right)^2\right]. \tag{4.13}$$

In general, we evaluate the focalization amplitude for times t close to the refocusing and positions $\mathbf{r}$ near $\mathbf{r}_0$. Thus, the action integral in the propagator of the returning waves can be expanded both in space and time according to

$$S_{s'}(\mathbf{r}, \mathbf{r}_i, t + \tau) \simeq S_{\tilde{s}}(\mathbf{r}_i, \mathbf{r}_0, \tau) - E_{\tilde{s}}\ t + \mathbf{p}_{\tilde{s}} \cdot (\mathbf{r} - \mathbf{r}_0). \tag{4.14}$$

Since we are dealing with those trajectories that arrive to $\mathbf{r}_0$ from the transducer, the starting and ending points are exchanged. Here we assume reciprocity in the semiclassical propagators, provided that the action integrals $S_{\tilde{s}}(\mathbf{r}_i, \mathbf{r}_0, \tau)$ and $S_{\tilde{s}}(\mathbf{r}_0, \mathbf{r}_i, \tau)$ are the same when traveled from $\mathbf{r}_i$ to $\mathbf{r}_0$ and back. Hence, the sign of the momentum results opposite as compared to that of Eq. (4.12). Furthermore, the expansion around the focalization time gives an additional term accounting for the energy of the trajectory

$$E_s = -\frac{\mathrm{d}}{\mathrm{d}t}\ S_s(\mathbf{r}, \mathbf{r}_i, \tau + t)|_{t=0}\,. \tag{4.15}$$

Therefore, the focalization signal writes as a double sum involving trajectories going from $\mathbf{r}_0$ to $\mathbf{r}_i$ according to

$$\begin{aligned} \mathcal{F}_{\mathbf{p}_0}(\mathbf{r}, t) &= \frac{\sigma}{2\pi^{3/2}\hbar^2} \int_{t_1}^{t_2} \mathrm{d}\tau \sum_{\tilde{s}(\mathbf{r}_0, \mathbf{r}_i, \tau)} \sum_{s(\mathbf{r}_0, \mathbf{r}_i, \tau)} \sqrt{C_s C_{s'}} \exp\left\{-\frac{\sigma^2}{2\hbar^2} \left(\mathbf{p}_s - \mathbf{p}_0\right)^2 + \right.\\ &+ \left. \frac{\mathrm{i}}{\hbar} \left[S_{\tilde{s}}(\mathbf{r}_i, \mathbf{r}_0, \tau) - S_s(\mathbf{r}_i, \mathbf{r}_0, \tau) - E_{\tilde{s}}\ t + \mathbf{p}_{\tilde{s}} \cdot (\mathbf{r} - \mathbf{r}_0)\right]\right\}. \end{aligned} \tag{4.16}$$

For different trajectories, the resulting fast oscillations in the action integral yield a small correction that can be neglected[2]. In the present work, we will consider only the main contribution given by the *diagonal approximation*, in which the same trajectories are kept ($s = s'$) and this leads to a focalization signal

$$\mathcal{F}_{\mathbf{p}_0}(\mathbf{r},t) = \tfrac{\sigma}{2\pi^{3/2}\hbar^2}\int_{t_1}^{t_2} \mathrm{d}\tau \sum_{s(\mathbf{r}_0,\mathbf{r}_i,\tau)} C_s \exp\left[-\tfrac{\sigma^2}{2\hbar^2}\left(\mathbf{p}_s-\mathbf{p}_0\right)^2 + \tfrac{\mathrm{i}}{\hbar}\left[\mathbf{p}_s\cdot(\mathbf{r}-\mathbf{r}_0) - E_s t\right]\right]. \tag{4.17}$$

In billiards, the same geometrical path $\hat{s}(\mathbf{r}_0,\mathbf{r}_i)$ can correspond to different traveling times that depend on the magnitude of the momentum. The energy and momentum can be expressed in terms of the length $L_{\hat{s}}$ and the traveling time τ as $E_s = \mathrm{p}_s^2/2m$ and $\mathrm{p}_s = mL_{\hat{s}}/\tau$ respectively. Furthermore, the stability factor C_s decreases for long times as $\exp(-\lambda_s\tau)$, with λ_s the largest Lyapunov exponent, whereas for the short time limit, it presents a ballistic behavior [CPJ04]. Assuming a uniformly hyperbolic dynamics [GWR08], and using $\lambda_s\tau = \hat{\lambda}L_{\hat{s}}$ (with $\hat{\lambda}$ an inverse length), we write

$$C_s = \frac{2m^2\hat{\lambda}L_{\hat{s}}}{\tau^2}\exp(-\hat{\lambda}L_{\hat{s}}). \tag{4.18}$$

The sum over trajectories can be converted into an integral over lengths by introducing the density [Sie99]

$$\frac{\mathrm{d}N(L)}{\mathrm{d}L} = \frac{\pi}{\hat{\lambda}\mathcal{A}}\exp(hL). \tag{4.19}$$

For closed systems $h = \hat{\lambda}$, and the long paths linking $\mathbf{r}_0$ to the transducer can be considered uniformly distributed along all directions. Hence, the sum over trajectories can then be replaced by a double integral over lengths and initial angles leading to the general expression of the focalization amplitude as

$$\begin{aligned}\mathcal{F}_{\mathbf{p}_0}(\mathbf{r},t) &= \frac{m^2\sigma}{\sqrt{\pi}\hbar^2\mathcal{A}}\int_{t_1}^{t_2}\frac{\mathrm{d}\tau}{\tau^2}\int_0^{2\pi}\frac{\mathrm{d}\varphi}{2\pi}\int_{L_\mathrm{d}}^{\infty}\mathrm{d}L\; L\exp\left[-\frac{\sigma^2}{2\hbar^2}\left(\frac{mL}{\tau}\mathbf{e}(\varphi)-\mathbf{p}_0\right)^2\right.\\ &+ \left.\frac{\mathrm{i}}{\hbar}\frac{mL}{\tau}\mathbf{e}(\varphi)\cdot(\mathbf{r}-\mathbf{r}_0) - \frac{\mathrm{i}}{\hbar}\frac{mL^2}{2\tau^2}t\right],\end{aligned} \tag{4.20}$$

where $\mathbf{e}(\varphi)$ is the unitary vector that refers to the direction of the trajectory with respect to the initial momentum and L_d is the typical length of the shortest trajectory linking $\mathbf{r}_0$ and $\mathbf{r}_i$. Throughout this chapter we evaluate this formula by including the extensions of the parameters $\mathbf{p}_0$, t and $\mathbf{r}$ respectively.

4.2 Focalization in the optimal condition

As a first step in the evaluation of the focalization, we start with the simplest form by setting $\mathbf{p}_0 = 0$ and the optimal conditions $t = 0$ and $\mathbf{r} = \mathbf{r}_0$. We use this condition in order

[2]Higher order contributions might be included by accounting for correlations between specific pairs of trajectories as in Ref. [GWK09].

to readily obtain the scaling of the focalization with the temporal width $\Delta T = t_2 - t_1$ that, as we shall see, it maintains the same form as that with a finite momentum configuration. From the general form of Eq. (4.20), the surviving term in the exponential yields the maximum refocusing $\mathcal{F}_{\max} = \mathcal{F}_0(\mathbf{r}_0, 0)$ as the integral

$$\mathcal{F}_{\max} = \frac{m^2\sigma}{\pi^{3/2}\hbar^2\mathcal{A}} \int_{t_1}^{t_2} \frac{\mathrm{d}\tau}{\tau^2} \int_{L_\mathrm{d}}^{\infty} \mathrm{d}L \; L \exp\left[-\left(\frac{L}{\nu\tau}\right)^2 \right], \tag{4.21}$$

where $\nu = \sqrt{2}\hbar/m\sigma$ is the "mean spread" velocity of the wave packet. Denoting $L_j = \nu t_j$ as the typical traveled lengths of the wave packet at the beginning ($j = 1$) and the end ($j = 2$) of the recording stage, we perform the time integration and obtain

$$\mathcal{F}_{\max} = \frac{(t_2 - t_1)}{\sigma\mathcal{A}} \left\{ \int_{L_\mathrm{d}/L_2}^{\infty} \mathrm{d}l \;\; [1 - \mathrm{erf}(l)] + t_1 \int_{L_\mathrm{d}/L_2}^{L_\mathrm{d}/L_1} \mathrm{d}l \;\; [1 - \mathrm{erf}\,(l)] \right\}, \tag{4.22}$$

where

$$\mathrm{erf}(x) = \frac{2}{\sqrt{\pi}} \int_0^x e^{-z^2} \mathrm{d}z, \tag{4.23}$$

stands for the error function. The assumptions made on C_s and $\mathrm{d}N(L)/\mathrm{d}L$ are valid for lengths a few times larger than L_d. However, our approximation is appropriate since we assume that we start recording at times t_1 larger than the corresponding Ehrenfest time of the system, *i.e.* the typical contributing trajectories "feel" the chaotic nature of the dynamics. Therefore, we work under the hypothesis $L_\mathrm{d} \ll L_1 < L_2$, that also allows us to neglect the last integral, leading to

$$\mathcal{F}_{\max} = \frac{1}{\sqrt{\pi}\sigma\mathcal{A}} \Delta T. \tag{4.24}$$

The scaling of the refocused signal with the injection interval ΔT is a quite natural result, experimentally observed in Ref. [DFi97]. On the other hand, the scaling with $\mathcal{A}$ has not been systematically tested so far. This scaling arises for the elemental area $\mathcal{A}_0$ (here $\mathcal{A}_0 = 1$) corresponding to a single transducer and may read as $\mathcal{A}_0/\mathcal{A}$. In the case where there is an array with N transducers, we simply have to integrate this last result over the involved "injection area" $\mathcal{A}_N$, but the surprising fact that just one detector is enough stems from Eq. (4.24). Additionally, the same normalization factor of the original excitation appears as indicative of the recovered state. In the following chapter we will describe this in more detail within the scheme of the Loschmidt echo where the overlap between the recovered and original states is taken.

In order to test this result, we performed a numerical evolution in a quarter of the Bunimovich billiard (see Fig. 4.2), which is a paradigm of classical chaotic dynamics. In a tight-binding model of the system, we calculate the evolution through a second order Trotter-Suzuki algorithm as in the quantum examples shown in chapter 2. We start with a Gaussian wave packet with $\sigma = 10a$ (a is the lattice constant) and $\mathbf{p}_0 = 0$, and

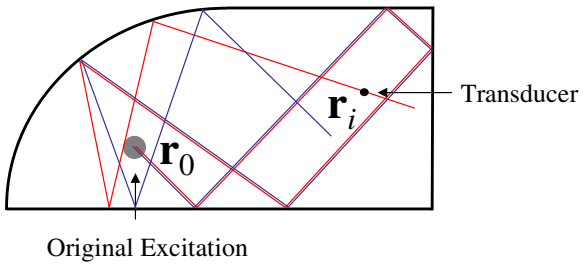

Figure 4.2: Schematics of the Bunimovich stadium. The original wave packet is centered around $\mathbf{r}_0$ and we use a single transducer placed in $\mathbf{r}_i$.

compute the evolution in a single point of the lattice. In the emission process, we assume an empty cavity since the remaining signals have already decayed at the level of noise. Alternatively, we may assume a decay due to absorption processes taking place at time scales much longer than t_2 in order to remain the registered dynamics unaffected.

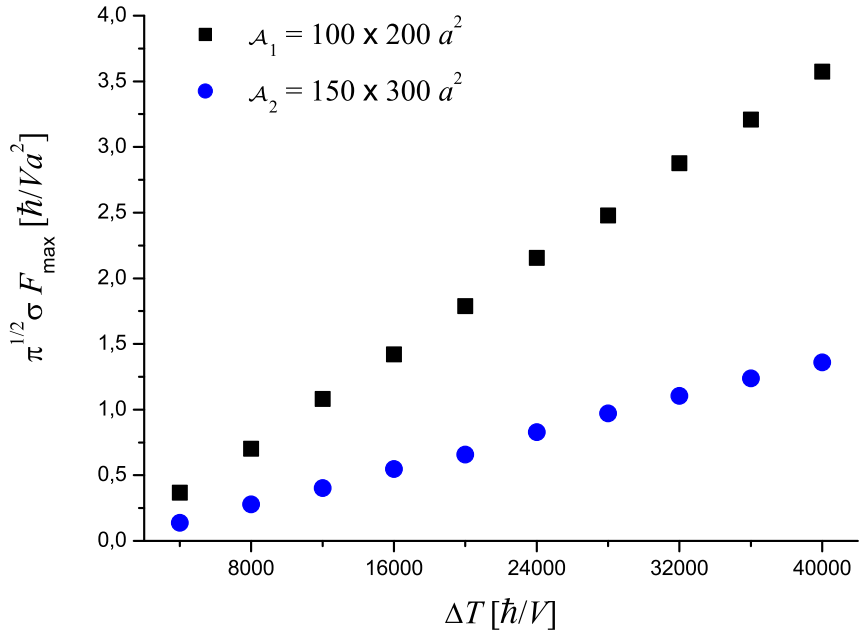

Figure 4.3: Numerical scaling with the temporal emission window ΔT for the areas $\mathcal{A}_1$ (black dots) and $\mathcal{A}_2$ (blue dots) respectively.

As shown in Fig. 4.3, the maximum values of the focalization amplitude are plotted for several periods ΔT increasing by steps of 4000 $\hbar/V$ and for two different areas. In the

example, we take $\mathcal{A}_1 = 100 \times 200\ a^2$ and $\mathcal{A}_2 = 150 \times 300\ a^2$ maintaining the same width of the Gaussian. As we can observe, there is a linear dependence with the emission period as described by Eq. 4.24. Although the slope a_i decreases with the area of the system, the obtained ratio $a_1/a_2 \simeq 2.6$ differs from our analytical findings where

$$\frac{a_1}{a_2} = \frac{\mathcal{A}_2}{\mathcal{A}_1} = 2.25. \tag{4.25}$$

This may be because the semiclassical limit works properly when $a \ll \sigma \ll L_\mathrm{b}$, with L_b the size of the billiard, and this is not completely fulfilled numerically. Hence, it may appear other effects related with the discreteness of the system or higher order corrections to the diagonal approximation.

4.2.1 Momentum contribution

Here we extend the above result for an initial Gaussian state with finite momentum and considering the optimal conditions $r = \mathbf{r}_0$ and $t = 0$. Defining φ as the subtended angle between the trajectory departing from $\mathbf{r}_0$ and the initial momentum, we have $\mathbf{e}(\varphi) \cdot \mathbf{p}_0 = \mathrm{p}_0 \cos\varphi$ and the argument in the exponential of Eq. (4.20) can be rewritten as

$$-\frac{\sigma^2}{2\hbar^2}\left(\mathrm{p}_0^2 \sin^2\varphi + \left(\frac{mL}{\tau} - \mathrm{p}_0\cos\varphi\right)^2\right). \tag{4.26}$$

Hence, we proceed with the corresponding time integral as

$$\mathcal{I}_1(L,\varphi) = \int_{t_1}^{t_2} \frac{\mathrm{d}\tau}{\tau^2} \exp\left[-\frac{\sigma^2}{2\hbar^2}\left(\frac{mL}{\tau} - \mathrm{p}_0\cos\varphi\right)^2\right] \tag{4.27}$$

$$= \frac{\sqrt{\pi}\hbar}{\sqrt{2}m\sigma L}\left[\mathrm{erf}(\eta_1) - \mathrm{erf}(\eta_2)\right], \tag{4.28}$$

where we have taken the replacement

$$\eta_i = \frac{L}{\nu t_i} - \frac{\mathrm{p}_0}{m\nu}\cos\varphi. \tag{4.29}$$

The next step is to calculate the integral over lengths given by

$$\mathcal{I}_2(\varphi) = \int_{L_\mathrm{d}}^{\infty} \mathrm{d}L\ L\ \mathcal{I}_1(L,\varphi), \tag{4.30}$$

and we perform the following definitions

$$l_i = L/\nu t_i, \qquad \text{and} \qquad l_\varphi = \frac{\mathrm{p}_0}{m\nu}\cos\varphi. \tag{4.31}$$

As in Eq. (4.21), the terms in the above integral are regrouped according to

$$\mathcal{I}_2(\varphi) = \frac{\sqrt{\pi}\hbar^2}{(m\sigma)^2}\left\{\Delta T\int_{L_\mathrm{d}/L_2}^{\infty}\mathrm{d}l\ \left[1-\mathrm{erf}(l-l_\varphi)\right] - t_1\int_{L_\mathrm{d}/L_2}^{L_\mathrm{d}/L_1}\mathrm{d}l\ \left[1-\mathrm{erf}(l-l_\varphi)\right]\right\}. \quad (4.32)$$

Again, the recording process is assumed to start once the wave packed has been spread out throughout the cavity. It may result important to note that this spreading corresponds to two different mechanisms:

1. As in the zero momentum case, the free evolution of the original wave packet presents "quantum diffusion" that yields a time dependent width

$$\sigma_t = \sqrt{\sigma^2 + \frac{(\nu t)^2}{2}}, \quad (4.33)$$

   and it allows the whole incursion at least in the real space.

2. On the other hand, if the wave packet starts with a large momentum ($\mathrm{p}_0 \gg m\nu$), the involved classical trajectories starting around the initial condition $(\mathbf{r}_0, \mathbf{p}_0)$ will separate exponentially with a rate given by the corresponding Lyapunov exponent. Hence, the phase space is completely explored once we start with the registration.

We will return to this point in Sec. 4.5 when tackling the differences in the recovered signal between chaotic and regular systems. Regardless of the involved mechanism, the lengths that are related to the recording signal satisfy $L_\mathrm{d} \ll L_1 < L_2$ and hence the last integral can be approximated as

$$\mathcal{I}_2(\varphi) \simeq \frac{\sqrt{\pi}\hbar^2\Delta T}{(m\sigma)^2}\int_0^{\infty}\mathrm{d}l\,\left[1-\mathrm{erf}(l-l_\varphi)\right], \quad (4.34)$$

$$\simeq \frac{\sqrt{\pi}\hbar^2\Delta T}{(m\sigma)^2}\left[\frac{\exp(-l_\varphi^2)}{\sqrt{\pi}} + l_\varphi\left[1+\mathrm{erf}(l_\varphi)\right]\right]. \quad (4.35)$$

Therefore, the optimal focalization writes

$$\mathcal{F}_{\mathbf{p}_0}(\mathbf{r}_0,0) = \frac{\Delta T}{\sigma\mathcal{A}}e^{-\sigma^2\mathrm{p}_0^2/2\hbar^2}\left\{\frac{1}{\sqrt{\pi}} + \int_0^{2\pi}\frac{\mathrm{d}\varphi}{2\pi}K\cos\varphi\ e^{K^2\cos^2\varphi}\left[1+\mathrm{erf}\left(K\cos\varphi\right)\right]\right\}, \quad (4.36)$$

where $K = \mathrm{p}_0/m\nu$. Because of the periodicity in the arguments in the range $(0, 2\pi)$, the first integral vanishes. By expanding the exponential and the error function and integrating term by term, we show in the Appendix C that

$$\mathcal{I}_3 = \int_0^{2\pi}\frac{\mathrm{d}\varphi}{2\pi}K\cos\varphi e^{K^2\cos^2\varphi}\mathrm{erf}\left(K\cos\varphi\right) = \frac{e^{K^2}-1}{\sqrt{\pi}}, \quad (4.37)$$

and hence,

$$\mathcal{F}_{\mathbf{p}_0}(\mathbf{r}_0,0) = \mathcal{F}_{\max} = \frac{1}{\sqrt{\pi}\sigma\mathcal{A}}\Delta T, \quad (4.38)$$

resulting in the same maximum focalization than that of Eq. (4.24) obtained for an initial state with zero momentum. The independence in the scaling with the momentum coincides with the expected recovering of the initial state evaluated in $\mathbf{r}_0$. However, as we shall see in the following section, the inversed momentum appears once we evaluate the time extension of the reversed signal.

4.3 Spatial and temporal resolutions

In addition to the focalization in the optimal condition, the experiments have shown that the same scaling is also observed in the temporal and spatial extends of the reconstructed signal. In order to evaluate the complete focalization, we work in the general situation presented in Eq. (4.20). In this case, the argument in the exponential is rearranged by completing squares and it can be rewritten as

$$-\frac{\sigma^2}{2\hbar^2}\left[\left(\mathrm{p}_0^2-\frac{(\mathrm{p}_0'\cos\varphi)^2}{\gamma}\right)+\gamma\left(\frac{mL}{\tau}-\frac{\mathrm{p}_0'\cos\varphi}{\gamma}\right)^2\right], \tag{4.39}$$

where we made the replacements

$$\gamma=1+\mathrm{i}\frac{\hbar t}{m\sigma^2},\qquad \mathbf{p}_0'=\mathbf{p}_0+\mathrm{i}\frac{\hbar}{\sigma^2}(\mathbf{r}-\mathbf{r}_0), \tag{4.40}$$

and $\mathbf{e}(\varphi)\cdot\mathbf{p}_0'=\mathrm{p}_0'\cos\varphi$ with

$$\mathrm{p}_0'^2=\mathrm{p}_0^2+2\mathrm{i}\frac{\hbar}{\sigma^2}\mathbf{p}_0\cdot(\mathbf{r}-\mathbf{r}_0)-\frac{\hbar^2}{\sigma^4}(\mathbf{r}-\mathbf{r}_0)^2. \tag{4.41}$$

The focalization amplitude takes the form

$$\mathcal{F}_{\mathbf{p}_0}(\mathbf{r},t)=\frac{m^2\sigma e^{-\sigma^2\mathrm{p}_0^2/2\hbar^2}}{\sqrt{\pi}\hbar^2\mathcal{A}}\int_0^{2\pi}\frac{\mathrm{d}\varphi}{2\pi}\exp\left[\frac{\sigma^2}{2\hbar^2\gamma}\left(\mathrm{p}_0'\cos\varphi\right)^2\right]\int_{L_\mathrm{d}}^{\infty}\mathrm{d}L\;L\;\mathcal{I}_1(L,\varphi), \tag{4.42}$$

with the time integral

$$\mathcal{I}_1(L,\varphi)=\int_{t_1}^{t_2}\frac{\mathrm{d}\tau}{\tau^2}\exp\left[-\frac{\sigma^2}{2\hbar^2}\gamma\left(\frac{mL}{\tau}-\frac{\mathrm{p}_0'\cos\varphi}{\gamma}\right)^2\right]. \tag{4.43}$$

Note here that the only difference with the previous case of Eq. (4.27) is the argument p_0' that not only accounts for the initial momentum but also has been extended into the complex domain through the mean spread velocity. By labeling α as the phase in $\gamma=e^{\mathrm{i}\alpha}\,|\gamma|$ and performing the replacements

$$\eta_i=\frac{\sigma e^{\mathrm{i}\alpha/2}}{\sqrt{2}\hbar}\,|\gamma|^{1/2}\left(\frac{mL}{t_i}-\frac{\mathrm{p}_0'\cos\varphi}{\gamma}\right), \tag{4.44}$$

we obtain the following expression for the time integral

$$\mathcal{I}_1(L,\varphi) = \frac{\sqrt{\pi}\nu}{2L}\frac{e^{-\mathrm{i}\alpha/2}}{|\gamma|^{1/2}}\left[\mathrm{erf}(\eta_1) - \mathrm{erf}(\eta_2)\right]. \tag{4.45}$$

In analogy with Eq. (4.30), the integral over lengths can be written according to

$$\begin{aligned}\mathcal{I}_2(\varphi) &= \int_{L_\mathrm{d}}^{\infty} \mathrm{d}L\ L\ \mathcal{I}_1(L,\varphi) &(4.46)\\ &= \frac{\sqrt{\pi}\nu}{2}\frac{e^{-\mathrm{i}\alpha/2}}{|\gamma|^{1/2}}\int_{L_\mathrm{d}}^{\infty}\mathrm{d}L\ \left[\mathrm{erf}(\eta_1) - \mathrm{erf}(\eta_2)\right]. &(4.47)\end{aligned}$$

Thus, defining $l_i = L/\nu' t_i$, and $l_\varphi = \mathrm{p}_0' \cos\varphi/(m\nu'\gamma)$ with

$$\nu' = \frac{\sqrt{2}\hbar}{m\sigma\,|\gamma|^{1/2}}, \tag{4.48}$$

the integral reads

$$\begin{aligned}\mathcal{I}_2(\varphi) &= \tfrac{\nu^2\sqrt{\pi}e^{-\mathrm{i}\alpha/2}}{|\gamma|}\left\{\Delta T\int_{L_\mathrm{d}/L_2}^{\infty}\left[1-\mathrm{erf}\left(e^{\mathrm{i}\alpha/2}(l-l_\varphi)\right)\right]\mathrm{d}l + \right. &(4.49)\\ &+ \left. t_1\int_{L_\mathrm{d}/L_2}^{L_\mathrm{d}/L_1}\left[1-\mathrm{erf}\left(e^{\mathrm{i}\alpha/2}(l-l_\varphi)\right)\right]\mathrm{d}l\right\}. &(4.50)\end{aligned}$$

Again, the assumption $L_\mathrm{d} \ll L_1 < L_2$ provides that the first term, proportional to ΔT, dominates over the second one and yields

$$\mathcal{I}_2(\varphi) = \left(\frac{\hbar}{m\sigma}\right)^2\frac{\sqrt{\pi}e^{-\mathrm{i}\alpha/2}}{|\gamma|}\Delta T\left[\frac{e^{-\mathrm{i}\alpha/2}}{\sqrt{\pi}}\exp(-e^{\mathrm{i}\alpha}l_\varphi^2) + l_\varphi\left[1+\mathrm{erf}\left(e^{\mathrm{i}\alpha/2}l_\varphi\right)\right]\right]. \tag{4.51}$$

Therefore, the general focalization amplitude writes

$$\mathcal{F}_{\mathbf{p}_0}(\mathbf{r},t) = \frac{e^{-\sigma^2\mathrm{p}_0^2/2\hbar^2}}{\gamma\sigma\mathcal{A}}\Delta T\left(\frac{1}{\sqrt{\pi}} + \mathcal{I}_4\right), \tag{4.52}$$

where $\mathcal{I}_4$ is the following integral over angles

$$\mathcal{I}_4 = \int_0^{2\pi}\frac{\mathrm{d}\varphi}{2\pi}e^{\mathrm{i}\alpha/2}l_\varphi\exp\left(e^{\mathrm{i}\alpha}l_\varphi^2\right)\left[1+\mathrm{erf}\left(e^{\mathrm{i}\alpha/2}l_\varphi\right)\right]. \tag{4.53}$$

By taking the replacement

$$e^{\mathrm{i}\alpha/2}l_\varphi = \frac{e^{-\mathrm{i}\alpha/2}}{|\gamma|^{1/2}}\frac{\sigma}{\sqrt{2}\hbar}\mathrm{p}_0'\cos\varphi = K\cos\varphi, \tag{4.54}$$

and noticing that the integration over the first term vanishes regardless the value of α, we found $\mathcal{I}_4 = \mathcal{I}_3$ and the recovered signal writes

$$\mathcal{F}_{\mathbf{p}_0}(\mathbf{r}, t) = \frac{e^{-\sigma^2 \mathrm{p}_0^2/2\hbar^2}}{\sqrt{\pi}\gamma\sigma\mathcal{A}} \Delta T \exp\left(\frac{\sigma^2}{2\hbar^2}\frac{\mathrm{p}_0'^2}{\gamma}\right). \tag{4.55}$$

This focalization then becomes

$$\mathcal{F}_{\mathbf{p}_0}(\mathbf{r}, t) = \frac{\mathcal{F}_{\max} e^{\mathrm{i}\alpha}}{\sqrt{1 + (\hbar t/m\sigma^2)^2}} \exp\left[-\frac{(\mathbf{r} - \mathbf{r}_0)^2}{2\sigma^2\gamma} + \frac{\mathrm{i}}{\hbar}\frac{\mathbf{p}_0}{\gamma} \cdot \left[\frac{\mathbf{p}_0 t}{2m} + (\mathbf{r} - \mathbf{r}_0)\right]\right], \tag{4.56}$$

which has the form of a reversed wave respect to the original one. The magnitude of the focalization amplitude is thus given by

$$|\mathcal{F}_{\mathbf{p}_0}(\mathbf{r}, t)| = \frac{\Delta T}{\sqrt{\pi}\sigma_t\mathcal{A}} \exp\left[-\frac{(\mathbf{r} - \mathbf{r}_0 + \mathbf{p}_0 t/m)^2}{2\sigma_t^2}\right], \tag{4.57}$$

where σ_t obeys Eq. (4.33). As we can see, the obtained recovering corresponds to the perfect reversal of the wave packet for times close to the focalization and in the focal region. From a slightly different point of view, the scaling factor $\Delta T/\mathcal{A}$ appears as a consequence of the "redundancies" in the detected signal. For instance, if the emission is taken over a series of small temporal windows $\Delta T/N_t$ as

$$t_1^n = t_1^0 + \frac{\Delta T}{N_t} n, \tag{4.58}$$

$$t_2^n = t_1^n + \frac{\Delta T}{N_t} \tag{4.59}$$

the signals arising in each interval will only interfere constructively in the focal region with the same contribution $|\mathcal{F}_{\mathbf{p}_0}(\mathbf{r}, t)|/N_t$.

As we will show in the following section, this result is also obtained using the ergodic approach [Arg96] of trading the actual dynamics by averaging in the phase space. The procedure presented in this section is more laborious than the ergodic approach, but allows to establish the necessary conditions for the refocalization and it has the advantage of being generalizable to the case where we introduce perturbations between the recording and injection phases.

4.3.1 Ergodic approach

Here we look at the problem from a different perspective and introduce the ergodicity hypothesis in order to treat the general case. The ergodic approach not only provides a second, and more economical, way of obtaining the general result without using a detailed knowledge of the dynamics, but also sheds some light into the necessary conditions for achieving the refocalization condition.

We start with the diagonal approximation for the focalization amplitude given by Eq. (4.17) and rewrite it according to

$$\mathcal{F}_{\mathbf{p}_0}(\mathbf{r},t) = \frac{\sigma}{2\pi^{3/2}\hbar^2}\int_{t_1}^{t_2} \mathrm{d}\tau\ F_{\mathbf{p}_0}(\mathbf{r}_0,\mathbf{r}_i,\mathbf{r},\tau), \tag{4.60}$$

$$F_{\mathbf{p}_0}(\mathbf{r}',\mathbf{r}'',\mathbf{r},\tau) = \sum_{s(\mathbf{r}',\mathbf{r}'',\tau)} C_s\ f_{\mathbf{p}_0}(\mathbf{r}',\mathbf{r},\mathbf{r}'',\mathbf{p}'), \tag{4.61}$$

$$f_{\mathbf{p}_0}(\mathbf{r}',\mathbf{r}'',\mathbf{r},\mathbf{p}') = \exp\left[-\tfrac{\sigma^2}{2\hbar^2}(\mathbf{p}'-\mathbf{p}_0)^2 - \tfrac{\mathrm{i}}{\hbar}E_s t + \tfrac{\mathrm{i}}{\hbar}\mathbf{p}'\cdot(\mathbf{r}-\mathbf{r}')\right]. \tag{4.62}$$

The basics of the ergodic approach is to calculate quantities like $F_{\mathbf{p}_0}(\mathbf{r}',\mathbf{r}'',\mathbf{r},\tau)$ through the average over the phase space [Arg96]. By denoting as $\mathbf{r}_\tau = \mathbf{r}_\tau(\mathbf{r}',\mathbf{p}')$ and $\mathbf{p}_\tau = \mathbf{p}_\tau(\mathbf{r}',\mathbf{p}')$ the position and momentum at certain time τ of a particle starting with $\mathbf{r}'$ and $\mathbf{p}'$ at the origin $t=0$, we have

$$F_{\mathbf{p}_0}(\mathbf{r}',\mathbf{r}'',\mathbf{r},\tau) = \int \mathrm{d}\mathbf{p}' \int \mathrm{d}\mathbf{p}'' \delta\left(\mathbf{r}_\tau - \mathbf{r}''\right)\delta\left(\mathbf{p}_\tau - \mathbf{p}''\right) f_{\mathbf{p}_0}(\mathbf{r}',\mathbf{r}'',\mathbf{r},\mathbf{p}'). \tag{4.63}$$

The double delta function represents the distribution of classical trajectories. An average over small ranges of the initial and final conditions gives a smooth distribution which describes the evolution in a statistical sense. For sufficiently long times such a distribution is τ independent, and uniformly distributed on the hyper-surface of constant energy (which for two dimensional billiards has a volume $\Omega = 2\pi m\mathcal{A}$ in the phase space). We therefore have

$$F_{\mathbf{p}_0}(\mathbf{r}',\mathbf{r}'',\mathbf{r},\tau) = \frac{1}{2\pi m\mathcal{A}}\int \mathrm{d}\mathbf{p}' \int \mathrm{d}\mathbf{p}'' \delta\left(\mathrm{p}'^2 - \mathrm{p}''^2\right) f_{\mathbf{p}_0}(\mathbf{r}',\mathbf{r}'',\mathbf{r},\mathbf{p}') \tag{4.64}$$

$$= \frac{1}{\mathcal{A}}\int \mathrm{d}\mathbf{p}'\ f_{\mathbf{p}_0}(\mathbf{r}',\mathbf{r}'',\mathbf{r},\mathbf{p}'). \tag{4.65}$$

Applying this general procedure to the function $f_{\mathbf{p}_0}$ we obtain

$$\mathcal{F}_{\mathbf{p}_0}(\mathbf{r},t) = \frac{\sigma\Delta T}{2\pi^{3/2}\hbar^2\mathcal{A}}\int \mathrm{d}\mathbf{p}' \exp\left[-\tfrac{\sigma^2}{2\hbar^2}(\mathbf{p}'-\mathbf{p}_0)^2 + \tfrac{\mathrm{i}}{\hbar}\mathbf{p}'\cdot(\mathbf{r}-\mathbf{r}_0) - \tfrac{\mathrm{i}}{\hbar}\frac{\mathrm{p}'^2}{2m}t\right], \tag{4.66}$$

since the integral over τ is now trivial. Performing the Gaussian integral over $\mathbf{p}'$ we recover the wave packet of Eq. (4.57) that re-focalizes with the same shape of the original one, but with momentum $-\mathbf{p}_0$.

4.4 Evaluating the focusing: The Trotter-Suzuki strategy

Numerical calculations of time reversal focalization have been performed in Ref. [DFi97] for a two-dimensional elastic cavity with the shape of a sliced disk. The signal reconstruction could be visualized and a qualitative agreement with the experimental results

was found. Since we dispose now of a quantitative semiclassical theory of refocusing it is important to test our predictions. As before, we calculate the time evolution of the wave packet through a second order Trotter-Suzuki algorithm for a discrete Schrödinger equation. Lattice effects are minimized by considering $a \ll \lambda_B \ll \sigma \ll L_b$, where λ_B the de Broglie wavelength associated with $\mathbf{p}_0$.

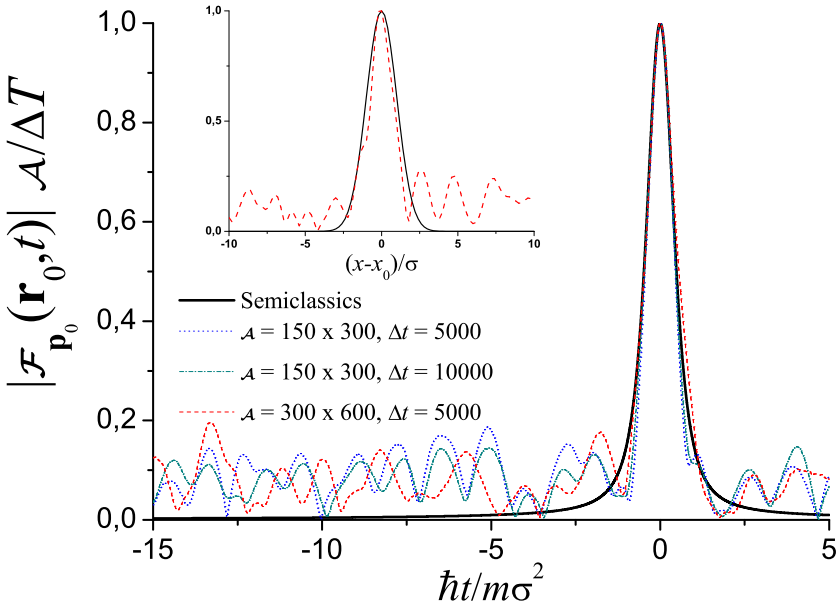

Figure 4.4: Reconstructed signal scaled with $\mathcal{A}/\Delta T$ at the emission point $\mathbf{r}_0$, close to the refocusing time $t = 0$. The thick black solid line is the semiclassical prediction. Numerical simulations for various ΔT $[\hbar/V]$ and $\mathcal{A}$: 5000 and 150×300 (blue dotted), 10000 and 150×300 (dark cyan dash-dotted), and 5000 and 300×600 (red dashed). Inset: reconstructed signal at $t = 0$ close to $\mathbf{r}_0$ from the semiclassical prediction (black solid) and simulation (red dashed) with $\Delta T = 5000$ and $\mathcal{A} = 300 \times 600$.

In Fig. 4.4 we show the numerical results for the time dependence on the reconstructed signal at $\mathbf{r}_0$. The normalized $\mathcal{F}_{\mathbf{p}_0}(\mathbf{r}_0, t)\mathcal{A}/\Delta T$ are well described by the semiclassical prediction (thick black solid) confirming the scaling with ΔT and $\mathcal{A}$ of Eq. (4.57). The normalizing factor for the numerical results is approximately 1.4 times the semiclassical one. As before, such a difference may be due to our discretization of the quantum problem as well as the difficulties of the diagonal approximation to recover exact numerical values. The signal-to-noise ratio does not change appreciably when the recording time is doubled, while it is slightly improved by increasing $\mathcal{A}$. In the inset we show the spatial reconstruction of the wave packet around $\mathbf{r}_0$ at the focusing time $t = 0$. We see that the

semiclassical prediction (black solid) provides the proper scaling behavior and, up to the normalization factor, a quantitative description of the TRM results.

4.5 Focalization in regular systems

The implementation of the TRM for integrable geometries represents a different mechanism as that presented throughout the chapter for ergodic systems. The semiclassical approach allows to understand *qualitatively* this important difference between chaotic and integrable systems, since in this last case we cannot use the mentioned hypothesis in order to get a general description of the stability factors or a precise sum rule accounting for the exponential proliferation of the trajectories. In such situation, the periodic orbits that take place in a regular cavity plays a central rôle in the semiclassical expansion of the propagators and should not be disregarded.

According to the discussion presented in Sec. 4.2.1 about the dispersion of the wave packet, we consider that the initial momentum is large as compared with the mean spread velocity, *i.e.* $\mathrm{p}_0 >> m\nu$. However, the relevance of the mentioned mechanisms will depend on the size of the system and the involved recording and emission times. The idea here is to separate the dispersion processes in order to get a clear distinction between chaotic and regular systems. Therefore, we start our analysis considering the case of a wave packet bouncing through the walls of a chaotic cavity. Here, the ergodic time is reached once the wave packet has spread in the whole system and can be assumed as the time that it takes to get a few bounces. Hence, if L_b is the typical longitude the billiard, we could estimate the recording times as

$$t_1 \simeq n_1 \, \frac{mL_\mathrm{b}}{\mathrm{p}_0}, \qquad t_2 \simeq n_2 \, \frac{mL_\mathrm{b}}{\mathrm{p}_0}, \tag{4.67}$$

where n_1 and n_2 are the number of bounces of the central trajectory, *i.e.* the classical path starting in $\mathbf{r}_0$ with the direction of $\mathbf{p}_0$. On the other hand, the "self-dispersion" of the wave packet given by the time dependent width σ_t can be estimated for the end of the registration and takes the form

$$\sigma_{t_2} = \sigma \sqrt{1 + \left(\frac{m\nu}{\mathrm{p}_0} \frac{nL_\mathrm{b}}{\sqrt{2}\sigma} \right)^2}. \tag{4.68}$$

This last states that for a particular choice of parameters of the initial wave packet, we can always increase the momentum according to

$$\mathrm{p}_0 > \sqrt{\frac{n}{2}} \frac{m\nu}{\sqrt{1 - (\sigma/L_\mathrm{b})^2}}, \tag{4.69}$$

in order to maintain the width of the wave packet smaller than L_b. In consequence, we get a ray picture of the dynamics in which the trajectories diverge only because their bounces with the walls.

In contrast, for regular systems, the above equation tell us that the involved trajectories will follow almost the same periodic orbit during the registration, maintaining the original shape of the wave packet. This yield a serious consequence when evaluating the refocusing after the emission period, resulting in a signal that strongly depends on the position of the transducers and results, at best, hardly distinguishable from the background.

4.6 Evaluating the Loschmidt Echo: The Lanczos-Trotter method

In this section we introduce the Lanczos method and its application to the calculation of the TRM focalization procedure. As we shall see, the technique constitute a powerful numerical tool that subtantially reduces the size of the basis required to compute the relevant dynamics. Here, the calculation of the time evolution operator is performed through the Trotter-Suzuki algorithm as before, but with the advantage that we work with a much smaller tight-binding basis set, where truncation enhances the computing time of the protocol. In addition, the Trotter-Suzuki represents by itself an ideal method in the evaluation of the time reversal procedures. Besides of the unitarity property, which is essential for the TRM, the method reproduces the injection of the detected signal without resorting beforehand to the propagator linking the transducer and the initial wave packet.

In the Lanczos algorithm, the real basis given by the tight-binding model is transformed according to the repeated application of the Hamiltonian over the initial state $|\psi_0\rangle$. If we denote by $\{|\varphi_i\rangle\}$ as the orthonormal Lanczos basis, their elements are obtained according to the following recurrences

$$
\begin{aligned}
|\varphi_0\rangle &= |\psi_0\rangle\,, && (4.70)\\
V_1\,|\varphi_1\rangle &= \mathbb{H}\,|\varphi_0\rangle - E_0\,|\varphi_0\rangle\,, && (4.71)\\
V_2\,|\varphi_2\rangle &= \mathbb{H}\,|\varphi_1\rangle - E_1\,|\varphi_1\rangle - V_1\,|\varphi_0\rangle\,, && (4.72)\\
&\vdots &&\\
V_n\,|\varphi_n\rangle &= \mathbb{H}\,|\varphi_{n-1}\rangle - E_{n-1}\,|\varphi_{n-1}\rangle - V_{n-1}\,|\varphi_{n-2}\rangle\,, && (4.73)
\end{aligned}
$$

where $E_n = \langle\varphi_n|\,\mathbb{H}\,|\varphi_n\rangle$ can be seen as the site energies and V_n the hopping amplitudes in the new Lanczos basis that redefines the old Hamiltonian. Hence, this new tridiagonal Hamiltonian can be interpreted as an effective one-dimensional tight-binding system. As shown in the scheme of Fig. 4.5, it is interesting to note here that the above equations represent, in some sense, the "propagation" of the initial state on the cavity.

In addition to the repeated application of the Hamiltonian, the resulting states in the Lanczos basis are built from the orthonormalization that yields the subtraction of the two last states according to the term $E_{n-1}\,|\varphi_{n-1}\rangle + V_{n-1}\,|\varphi_{n-2}\rangle$.

The central property of the Lanczos procedure is that every recursion step collects information from a new layer of nodes. Therefore, it rapidly reaches the frontiers of

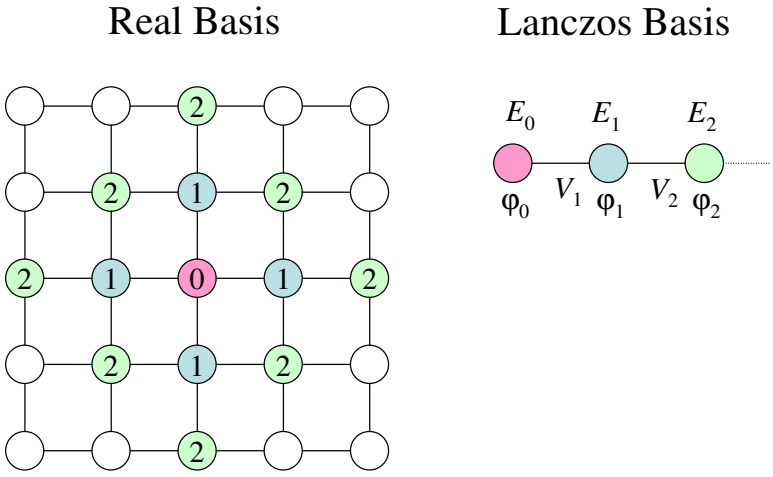

Figure 4.5: Scheme of the Lanczos algorithm. The initial state $|0\rangle$ "propagates" throughout the system as the novel basis is redefined.

the system and starts including multiple "reflections". The idea is that the dynamics calculated in this new basis collects information of all the system even now when a much smaller number of states are included.

For the TRM procedure, we should compute the wave function that arrives to the transducer from the initial excitation according to

$$\psi(\mathbf{r}_S, t) = \langle \mathbf{r}_S | \exp\left(-\mathrm{i}\mathbb{H}t/\hbar\right) |\psi_0\rangle \,. \tag{4.74}$$

As we can see, this may represent a difficult task since we should take the projections over $|\mathbf{r}_S\rangle$ from the basis states that come from the initial wave packet. In fact, such calculation involves the evaluation of the complete Lanczos basis and the efficiency of the method could be lost. In order to obtain a suitable basis where the state of the transducer $|\mathbf{r}_S\rangle$ is well represented, we can perform the Lanczos algorithm for two different initial states $\{|+\rangle, |-\rangle\}$ that correspond to the linear combination between the initial wave packet and a local excitation at the site of the transducer, *i.e.*

$$|+\rangle = \frac{|\psi_0\rangle + |\mathbf{r}_S\rangle}{\sqrt{2}}, \tag{4.75}$$

$$|-\rangle = \frac{|\psi_0\rangle - |\mathbf{r}_S\rangle}{\sqrt{2}}. \tag{4.76}$$

For each one of these initial states, we apply the recurrence formulae and define two independent Lanczos bases that yield the Hamiltonians $\mathbb{H}^+$ and $\mathbb{H}^-$ respectively. Thus, the dynamics of the corresponding surface states is

$$\psi_+(t) = \langle + | \exp\left(-\mathrm{i}\mathbb{H}^+ t/\hbar\right) |+\rangle \,, \tag{4.77}$$

$$\psi_-(t) = \langle - | \exp\left(-\mathrm{i}\mathbb{H}^- t/\hbar\right) |-\rangle \,, \tag{4.78}$$

that can be obtained through the usual Trotter-Suzuki algorithm. Finally, the detected wave function at the transducer location is computed according to

$$\begin{aligned}\psi(\mathbf{r}_S,t) &= \frac{1}{2}\left[\langle+|\exp\left(-\mathrm{i}\mathbb{H}^+t/\hbar\right)|+\rangle - \langle-|\exp\left(-\mathrm{i}\mathbb{H}^-t/\hbar\right)|-\rangle\right. &(4.79)\\ &+ \left.\langle+|\exp\left(-\mathrm{i}\mathbb{H}t/\hbar\right)|-\rangle - \langle-|\exp\left(-\mathrm{i}\mathbb{H}t/\hbar\right)|+\rangle\right], &(4.80)\end{aligned}$$

For systems with time-reversal symmetry, one is sure that the exchange term satisfies a reciprocity relation

$$\langle+|\exp\left(-\mathrm{i}\mathbb{H}t/\hbar\right)|-\rangle = \langle-|\exp\left(-\mathrm{i}\mathbb{H}t/\hbar\right)|+\rangle\,. \tag{4.81}$$

Therefore, the calculation of the wave function reaching the transducer reduces to the evaluation of the survival amplitudes of the "surface" states $|+\rangle$ and $|-\rangle$.

Now that we have the registered signal at the transducer, the reversion in the dynamics can be obtained through the injection of $\psi^*(\mathbf{r}_S, 2t_R - t)$ during a period ΔT. This injection is performed for the both Hamiltonians $\mathbb{H}^+$ and $\mathbb{H}^-$ and the focalization is calculated as the difference of both resulting propagations

$$\begin{aligned}\psi_0(t) &= \int_{t_R}^{t} \mathrm{d}t'\,\langle\psi_0|\,e^{-\mathrm{i}\mathbb{H}(t-t')/\hbar}\,|\mathbf{r}_S\rangle\,\psi^*(\mathbf{r}_S, 2t_R - t'), &(4.82)\\ &= \int_{t_R}^{t} \mathrm{d}t'\,\left[\langle+|\,e^{-\mathrm{i}\mathbb{H}^+(t-t')/\hbar}\,|+\rangle - \langle-|\,e^{-\mathrm{i}\mathbb{H}^-(t-t')/\hbar}\,|-\rangle\right]\psi^*(\mathbf{r}_S, 2t_R - t'). &(4.83)\end{aligned}$$

In consequence, the obtained focalization corresponds to the overlap between the recovered signal and the original wavepacket.

In Fig. 4.6 we compare the propagation of a Gaussian wave packet in a closed cavity calculated through the direct Trotter-Suzuki method and the Lanczos method for two truncated bases with $N_L = 700$ and 1000 sites respectively. The considered times are those related with the registration of the signal and that given by the truncated basis obtained from the Lanczos method. In the TRM procedure, the registration begins once the system reaches the ergodic time, that can be assumed as a few times the mesoscopic echo. Hence,

$$t_1 = n\; t_{\mathrm{ME}} \simeq 2N\frac{\hbar}{V}n, \tag{4.84}$$

where N is the number of sites along one direction in the system. Therefore, the Lanczos-Trotter will reproduce faithfully the dynamics whenever the registration ends up for times scales smaller than the "Lanczos mesoscopic echo" time t_L that result from the truncation of the complete Lanczos basis. In this sense, we can take $t_2 = m\; t_{\mathrm{ME}}$, with $m > n$ maintaining $t_L > t_2$.

It is important to note that, unlike the direct Trotter-Suzuki dynamics, this method obtains the focalization directly as the overlap between the recovered signal and the initial wave packet. This excludes the evaluation of the focalization contrast for different positions. Meanwhile, we differ the numerical results until the next chapter, where it will be used extensively, and further discussion is still in order.

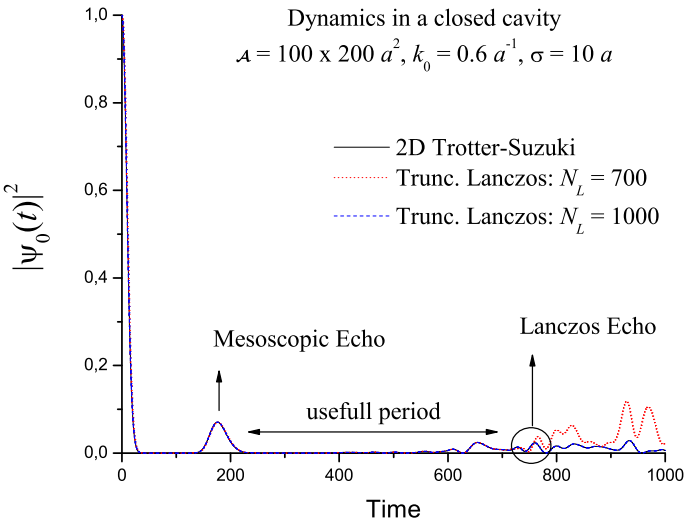

Figure 4.6: Involved times in the wave packet propagation. The almost exact (black solid) is contrasted with the truncated basis composed by $N_L = 700$ (red dotted) and $N_L = 1000$ (blue dashed) sites respectively.

As we can observe, the relevance of the method lies with the fact that obtains the time evolution in a system composed by $N \times N$ states through the numerical computation of $\sim N$ states, reducing significatively the computing time.

4.7 Summary

In conclusion, we have presented detailed semiclassical calculations of the focalization signal for the time reversal mirror procedure where the chaotic nature of the underlying classical dynamics appears as a necessary condition for the reconstruction. As pointed out in Eq. (4.57), the injection of the detected propagation through a single transducer during a finite emission interval ΔT is enough to recover the original dynamics and hence the compression of the signal at the focusing time. Throughout the chapter, we worked under the diagonal approximation where the involved forward and backward classical trajectories were assumed to be the same. We observed that the focalization at the optimal condition ($\mathbf{r} = \mathbf{r}_0$, $t = 0$) scales linearly with the emission interval. Furthermore, we showed that the spatial and temporal extensions of the focalization maintained this scaling in agreement with the experimental results on elastic waves propagating in a monocrystalline silicon wafer [DFi97]. In addition to these findings, the scaling showed to be proportional to the number of transducers, defining the "injection area" $\mathcal{A}_N$ used in the protocol and inversely proportional to the total area $\mathcal{A}$ of the system. Interestingly,

this scaling appears as a central result in this thesis since it may be interpreted as the fact that there is no dependence on the location of the transducers, provided by the ergodic property of the considered system. As we shall see in the next chapter, this constitutes the starting point in the evaluation of the focalization in terms of the Loschmidt echo scheme.

Although these calculations cannot be directly applied to integrable geometries, they may provide a ray picture where the experiments show a poorer signal reconstruction with lower signal compression, the appearance of focalization satellites, and a strong sensitivity with respect to the position of the transducers. As we pointed out in Sec. 4.5, the exponential proliferation of trajectories that occur in chaotic systems allows to encode the information at all times, while in the latter the registered signal would strongly depends on whether or not the source and the transducer are connected by a stable trajectory.

The evaluation of the focalization may be performed through a novel numerical strategy based on the combination of two well known methods: the Trotter and the Lanczos algorithms. In a two-dimensional system composed by $N \times N$ states, the Lanczos strategy reduces the complete basis in an effective one that scales linearly with N and hence, it enhances the computing time as compared with the usual Trotter method. This last is achieved through the repeated application of the Hamiltonian over the initial state that allows the collection of the relevant energies that concerns the propagation. Through a linear combination between the initial wave packet and the basis state of the transducer, we obtained a way to compute the recording and injection of the signal in the transducer. This enabled us to evaluate the focalization in terms of the overlap between the recovered excitation and the original wave packet.

Chapter 5

Irreversible processes and the time reversal focusing

In the previous chapter, we analyzed the recovering of an initial state that is recorded and emitted by a single transducer following the TRM procedure in a closed chaotic cavity. Under the semiclassical approximation, we showed that the focalization is proportional to the emission interval and inversely proportional to the area of the cavity. In general, the ergodic hypothesis, *i.e.* there are infinite ways to reach any point in a given time, is a prominent condition for the appearance of such refocusing and enabled its analytical evaluation. This hypothesis provided for the redundancy implicitly required for the time and space reconstructions. We found that the position of the transducer becomes irrelevant and the focalization is proportional to the number of involved transducers. Throughout the chapter, we evaluate the TRM procedure in two different situations:

1. We analyze the stability of the focalization in **open cavities**, where the chaotic cavity is connected, through a small opening, to a waveguide or boundless propagating medium. This also can be seen as the simplest example of a dissipative perturbation or damping process leading to $\mathrm{Im}\,\Sigma = -\Gamma$. In consequence, the focalization intensity may be related with the *nonescape probability* [GMM95] of the internal excitation.

2. For **closed chaotic cavities** we introduce an external perturbation Σ ($\mathrm{Im}\,\Sigma = 0$), between the recording and emission stages. In this situation, we stress the similarities with the related case of the *Loschmidt echo amplitude*

$$m(t) = \langle\psi_0| \exp(\mathrm{i}(H+\Sigma)t/\hbar) \exp(-\mathrm{i}Ht/\hbar) |\psi_0\rangle\,, \tag{5.1}$$

   where the reconstruction of an initially localized quantum state is obtained by the inversion of the dynamics after some propagation time t, and where the involved classical dynamics was shown to play an important rôle [JPa01].

In both cases, we readapt the expression of the focalization signal as the overlap between the wave at the time of focusing, produced by the TRM procedure, and the

original wave packet according to

$$m(t_1,t_2)=\int_{\mathcal{A}}\mathrm{d}\mathbf{r}\ \psi_{\mathbf{p}_0}(\mathbf{r})\mathcal{F}_{\mathbf{p}_0}(\mathbf{r},0). \tag{5.2}$$

We calculate this overlap through the semiclassical expansion of the involved propagators by following a strategy [WGG08] which is a slight modification of the one used in Chapter 4. As before, we will consider only the leading contributions that come from the diagonal approximation.

5.1 Focalization in open systems

To start, we consider the focalization signal that takes place in the focusing time according to the general expression of Eq. (4.5)

$$\mathcal{F}_{\mathbf{p}_0}(\mathbf{r},0)=\int_{\mathcal{A}}\mathrm{d}\mathbf{r}''\ g(\mathbf{r}'')\int_{t_1}^{t_2}\mathrm{d}t\int_{\mathcal{A}}\mathrm{d}r' K(\mathbf{r},\mathbf{r}'',t)K^*(\mathbf{r}'',\mathbf{r}',t)\psi^*_{\mathbf{p}_0}(\mathbf{r}'). \tag{5.3}$$

Here, the detection and emission is performed by an array of N transducers that are distributed along the cavity. The term $g(\mathbf{r}'')$ represents the distribution that yields the "injection area" of the signal such that

$$\int_{\mathcal{A}}\mathrm{d}\mathbf{r}''\ g(\mathbf{r}'')=\mathcal{A}_N. \tag{5.4}$$

Instead of solving such focalization, which was the subject of study in the previous chapter, we analyze the overlap given by Eq. (5.2) of the resulting reversed wave with the initial state

$$m(t_1,t_2)=\int_{\mathcal{A}}\mathrm{d}\mathbf{r}''\ g(\mathbf{r}'')\int_{t_1}^{t_2}\mathrm{d}t\int_{\mathcal{A}}\mathrm{d}\mathbf{r}'\mathrm{d}\mathbf{r}\ \psi_{\mathbf{p}_0}(\mathbf{r})K(\mathbf{r},\mathbf{r}'',t)K^*(\mathbf{r}'',\mathbf{r}',t)\psi^*_{\mathbf{p}_0}(\mathbf{r}'). \tag{5.5}$$

In ergodic systems, we assumed before that the recording process starts once the available phase space has been fully explored, *i.e.* $t_1 > t_E$ with t_E the corresponding Ehrenfest time. As a consequence of such ergodicity, the resulting focalization becomes independent of the position of the transducers and will only account for the number of them. Hence, the $\mathbf{r}''$ integral yields

$$m(t_1,t_2)\simeq\mathcal{A}_N\int_{t_1}^{t_2}\mathrm{d}t\ \psi_{\mathbf{p}_0}(\mathbf{r}_i,t)\psi^*_{\mathbf{p}_0}(\mathbf{r}_i,t), \tag{5.6}$$

where we assumed reciprocity in the backward propagation and $\mathbf{r}_i$ stands for the (arbitrary) position of one of the transducers. As the focalization does not change with $\mathbf{r}_i$, we can take the integral over all the cavity and hence

$$m(t_1,t_2)\simeq\frac{\mathcal{A}_N}{\mathcal{A}}\int_{t_1}^{t_2}\mathrm{d}t\ P(t), \tag{5.7}$$

with

$$P(t) = \int_{\mathcal{A}} \mathrm{d}\mathbf{r}_i \; \psi(\mathbf{r}_i, t)\psi^*(\mathbf{r}_i, t), \tag{5.8}$$

the nonescape probability of finding a particle still confined in the cavity [GMM95]. For closed systems, it gives the norm of the state $P(t) = 1$ and therefore the time integral trivially results

$$m(t_1, t_2) = \frac{\mathcal{A}_N}{\mathcal{A}} \Delta T, \tag{5.9}$$

that is, the same scaling as that of Eq. (4.57) is obtained.

For open systems, we consider an initially localized wave packet inside the cavity. A small opening of size w is performed at the boundaries of the cavity and the norm inside no longer conserves. Hence, the nonescape probability will decay in time due to the escape towards the outside region, consisting of a boundless system or a waveguide. Under the semiclassical approximation, we expand the propagators that are present in the nonescape probability according to Eq.(4.8)

$$P(t) = \tfrac{1}{(2\pi\hbar)^2} \int_{\mathcal{A}} \mathrm{d}\mathbf{r}_i \mathrm{d}\mathbf{r}' \mathrm{d}\mathbf{r}'' \; \psi_{\mathbf{p}_0}(\mathbf{r}')\psi^*_{\mathbf{p}_0}(\mathbf{r}'') \sum_{\substack{s(\mathbf{r}', \mathbf{r}_i, t) \\ s'(\mathbf{r}'', \mathbf{r}_i, t)}} \sqrt{C_s C_{s'}} e^{\frac{\mathrm{i}}{\hbar}(S_s - S_{s'})}. \tag{5.10}$$

The action integrals are then expressed in terms of those trajectories that depart from a common point $\bar{\mathbf{r}} = (\mathbf{r}' + \mathbf{r}'')/2$ and arrive to $\mathbf{r}_i$ in a time t according to the usual linear terms

$$S_s(\mathbf{r}_i, \mathbf{r}', t) \simeq S_s(\mathbf{r}_i, \bar{\mathbf{r}}, t) - \frac{1}{2}\mathbf{q} \cdot \mathbf{p}_s, \tag{5.11}$$

$$S_{s'}(\mathbf{r}_i, \mathbf{r}'', t) \simeq S_{s'}(\mathbf{r}_i, \bar{\mathbf{r}}, t) + \frac{1}{2}\mathbf{q} \cdot \mathbf{p}_{s'}, \tag{5.12}$$

where $\mathbf{q} = \mathbf{r}' - \mathbf{r}''$ and $\mathbf{p}_s$ ($\mathbf{p}_{s'}$) is the initial momentum related to the trajectory s (s'). If we work under the diagonal approximation ($s = s'$), the above replacements yield

$$P(t) = \frac{1}{(2\pi\hbar)^2} \int_{\mathcal{A}} \mathrm{d}\mathbf{r}_i \mathrm{d}\bar{\mathbf{r}} \sum_{s(\bar{\mathbf{r}}, \mathbf{r}_i, t)} C_s \; \rho_W(\bar{\mathbf{r}}, \mathbf{p}_s), \tag{5.13}$$

with

$$\rho_W(\bar{\mathbf{r}}, \mathbf{p}_s) = \int \mathrm{d}\mathbf{q} \; \psi_{\mathbf{p}_0}\left(\bar{\mathbf{r}} + \frac{\mathbf{q}}{2}\right) \psi^*_{\mathbf{p}_0}\left(\bar{\mathbf{r}} - \frac{\mathbf{q}}{2}\right) e^{-\frac{\mathrm{i}}{\hbar}\mathbf{p}_s \cdot \mathbf{q}}, \tag{5.14}$$

the Wigner function of $\psi_{\mathbf{p}_0}(\bar{\mathbf{r}})$. For the initial state, we consider an excitation with a well-defined energy that can be faithfully represented through a Gaussian wave packet centered around $\mathbf{r}_0$ and with momentum $\mathbf{p}_0$ as in Eq. (4.6) and the Wigner function takes the form

$$\rho_W(\bar{\mathbf{r}}, \mathbf{p}_s) = 4 \exp\left[-\frac{(\bar{\mathbf{r}} - \mathbf{r}_0)^2}{\sigma^2} - \frac{\sigma^2}{\hbar}(\mathbf{p}_s - \mathbf{p}_0)^2\right]. \tag{5.15}$$

Here, we use the ergodic hypothesis assuming that the focalization does not depend on the transducer's location and the integration over positions $\bar{\mathbf{r}}$ is taken over the Wigner function assuming that the trajectories start at the center of the wave packet. Therefore, the integrations over the initial and final points $\bar{\mathbf{r}}$ and $\mathbf{r}_i$ yield the following nonescape probability

$$P(t) = \frac{\sigma^2 \mathcal{A}}{\pi \hbar^2} \sum_{s(\mathbf{r}_0, \mathbf{r}_i, t)} C_s \ \exp\left[-\frac{\sigma^2}{\hbar^2} (\mathbf{p}_s - \mathbf{p}_0)^2 \right], \tag{5.16}$$

where the classical trajectories only account for the involved lenghts L_s. Again, we recall to Eqs. (4.19) and (4.18) in order to describe the detailed form of the stability factor and the sum rule for the involved classical trajectories. Hence, the nonescape probability contains the additional factor $e^{-(\hat{\lambda}-h)L}$ that accounts for the opening. As before, we assume, for simplicity, an initial state with $\mathrm{p}_0 = 0$ and obtain

$$P(t) = \frac{2}{(\nu t)^2} \int_{L_\mathrm{d}}^{\infty} \mathrm{d}L \ L \ e^{-\xi L} \exp\left[-\left(\frac{L}{\nu t} \right)^2 \right], \tag{5.17}$$

with $\nu = \hbar / m\sigma$ and $\xi = \hat{\lambda} - h$. For closed systems we have $\xi = 0$ and the integral over lenghts can be assumed as starting from 0 since, as always, the lenght νt of the involved trajectories are longer than the typical size of the system. The resulting integral yields the norm conservation $\rho(t) = 1$ and recovers the usual scaling of Eq. (5.9).

On the other hand, when considering the case $\xi \neq 0$ we assume a small opening in order to remain unaffected the ergodic property of the corresponding closed system. In such case, the nonescape probability decays according to

$$P(t) = 1 - \sqrt{\pi} \frac{\nu \xi}{2} t \left[1 - \mathrm{erf}\left(\frac{\nu t}{2} \xi \right) \right] \exp\left[\left(\frac{\nu t}{2} \xi \right)^2 \right]. \tag{5.18}$$

The time integral can be calculated through the expansion of the above exponentials and integrating term by term in a similar way as that presented in the Appendix C for the scaling of the focalization. Hence, the focalization obeys

$$m(t_1, t_2) = \frac{\mathcal{A}_N}{\mathcal{A}} \frac{\sqrt{\pi}}{\nu \xi} \left[e^{(\nu t_1 \xi / 2)^2} \mathrm{erfc}\left(\tfrac{\nu t_1 \xi}{2} \right) - e^{(\nu t_2 \xi / 2)^2} \mathrm{erfc}\left(\tfrac{\nu t_2 \xi}{2} \right) \right], \tag{5.19}$$

with $\mathrm{erfc}(x) = 1 - \mathrm{erf}(x)$. We call this expression as the cumulative semiclassical (CSc) and shows a steady growth until a stationary value which is reached asymptotically in a time characterized by the decay of the wave packet. When the recording interval is small enough so the number of contributing trajectories remain unaffected by the opening, *i.e.* $\nu \Delta T << \xi^{-1}$, we can approximate the above result in terms of the characteristic decay time. Here, the nonescape probability presents an exponential decay that can be seen as a form of a Fermi golden rule

$$P(t) \simeq e^{-t/\tau_d}, \tag{5.20}$$

with $1/\tau_d = \nu w/\pi\mathcal{A}$ the classical escape rate at the central energy of the wave packet [GWK09][1] and w the size of the opening such that $w = \pi^{3/2}\mathcal{A}\xi/2$. Therefore, if we take $\bar{t} = (t_1 + t_2)/2$ as the center of the recording interval, the focalization reads

$$m(t_1, t_2) = \frac{\mathcal{A}_N}{\mathcal{A}} \int_{\bar{t}-\frac{\Delta T}{2}}^{\bar{t}+\frac{\Delta T}{2}} e^{-t/\tau_d} \mathrm{d}t \tag{5.21}$$

$$= \frac{\mathcal{A}_N}{\mathcal{A}} 2\tau_d e^{-\bar{t}/\tau_d} \sinh\left(\frac{\Delta T}{2\tau_d}\right). \tag{5.22}$$

In addition to the usual scaling, there is an exponential attenuation that depends on where is the center of the recording interval as compared to the decay. By increasing the value of $\bar{t}$, the above result is no longer valid and we should remit to the CSs of Eq. (5.19) for a more accurate description of the focalization.

In order to test these results, we reproduced numerically the time evolution of a wave packet in a stadium billiard with a small opening. In the tight-binding system employed, the infinite waveguide which extend along the x axis and is connected to the billiard at $x = 0$. This can be modeled through a finite rectangular system composed by complex site energies that ensures the irreversible escape of the excitation. These grow linearly according to

$$\Gamma(\mathbf{r}) = -\mathrm{i}\eta \frac{x}{L_x}, \tag{5.23}$$

with L_x the horizontal length of the outer region and $0 < x \leq L_x$. In the Trotter-Suzuki propagation of the evolution operator, these diagonal terms yield a damping of the wave packet due to the escape to the outer region according to

$$\psi(\mathbf{r}, t) \leftarrow \exp\left[-\mathrm{i}\Gamma(\mathbf{r})\tau/\hbar\right] \psi(\mathbf{r}, t), \tag{5.24}$$

where τ is the time step of the algorithm. As in the harmonic oscillators of the Chapter 3, no more mesoscopic echoes appear and the decay is faithfully reproduced. Hence, since the full propagator may be computed, we calculate the nonescape probability of Eq. (5.8) and evaluate its corresponding time integral.

In Fig. 5.1 we show the rescaled focalization $\mathcal{A}\, m(t_1, t_2)/\mathcal{A}_N$ for two different sizes of the opening. Here, the center and width of the emission window are increased simultaneously with $t_1 = 0$ and $t_2 = t$. As we can see, the diagonal approximation provides a good description of the numerical results when $t \ll \tau_d$. However, for times comparable to the characteristic time decay, the nonescape probability exceeds the predicted value. We observe that the obtained focalization grows faster than the FGR since the decay in the nonescape probability is attenuated. There are two physical effects that might contribute to enhance the survival. One is because there are waves that return to the cavity from the environment. These provide a higher nonescape probability than that evaluated from the FGR and, for long times, it yields a power law in the decay [RFP06]. Additionally, the

[1] As compared with the resulting decay of Ref. [GWK09], we include the average over time once we compute the focalization as in Eq. 5.7.

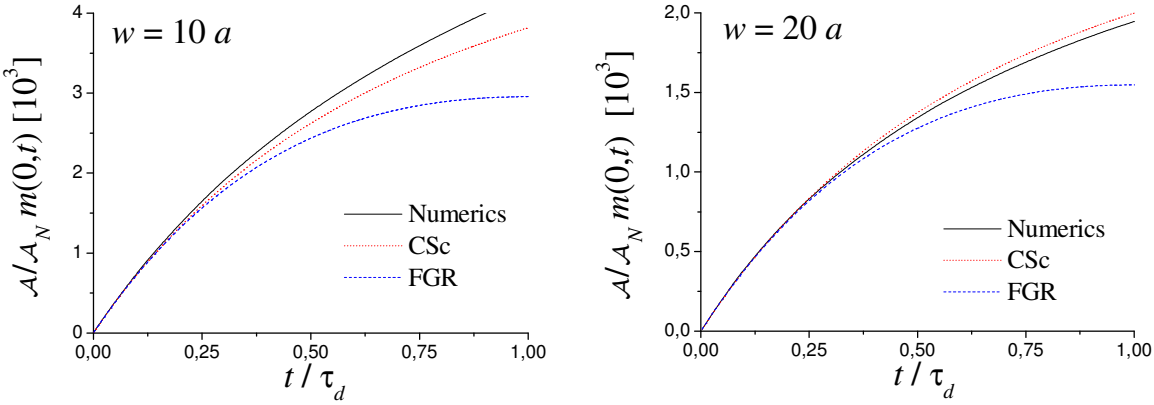

Figure 5.1: Rescaled focalization in an open chaotic cavity for the sizes $w = 10\ a$ (left) and $w = 20\ a$ (right). The numerical solution (black solid) is contrasted with the cumulative semiclassical regime of Eq. (5.19) (red dotted) and the FGR (blue dashed).

weak localization corrections [GWK09] yield a smaller diffusion constant than that resulting from the FGR or Random Phase Approximation. In this sense, further work would be necessary to determine which of the two is more important it the observed increase of the nonescape probability.

5.2 Focalization and the Loschmidt Echo

Experimentally, the TRM procedure has shown to be robust against local and global perturbations introduced between the recording and injection periods [DRF95]. Even in the absence of these perturbations, it is natural to expect that any TRM setup contains some uncontrollable evolution of the environment and therefore unavoidable errors in the reversal protocol. Furthermore, intentional changes in the setup between the recording and emission stages may be used in the assessment of the stability of the procedure. In the spirit of the Loschmidt echo studies [JPa01], we can visualize the effect of a generic perturbation by writing the reconstructed signal as

$$\mathcal{F}_{\mathbf{p}_0}(\mathbf{r},t) = \int_{\mathcal{A}} \mathrm{d}\mathbf{r}_i\ g(\mathbf{r}_i) \int_{t_1}^{t_2} \mathrm{d}\tau \tilde{K}(\mathbf{r},\mathbf{r}_i,t+\tau) \int_{\mathcal{A}} \mathrm{d}\mathbf{r}' K^*(\mathbf{r}_i,\mathbf{r}',\tau)\psi^*_{\mathbf{p}_0}(\mathbf{r}'), \tag{5.25}$$

where $\tilde{K}(\mathbf{r},\mathbf{r}_i,t+\tau)$ refers to the propagator in the perturbed system. For this focalization, we take the overlap with the initial state as

$$m(t_1,t_2) = \int_{\mathcal{A}} \mathrm{d}\mathbf{r}\ \psi_{\mathbf{p}_0}(\mathbf{r})\mathcal{F}_{\mathbf{p}_0}(\mathbf{r},0) = \int_{t_1}^{t_2} \mathrm{d}\tau \int_{\mathcal{A}} \mathrm{d}\mathbf{r}_i\ g(\mathbf{r}_i)\varphi(\mathbf{r}_i,\tau)\psi^*(\mathbf{r}_i,\tau).$$

Here, we use the ergodic hypothesis in order to perform the integral over $\mathbf{r}_i$ and obtain

$$m(t_1,t_2) \simeq \frac{\mathcal{A}_N}{\mathcal{A}} \int_{t_1}^{t_2} \mathrm{d}\tau\ m(\tau), \tag{5.26}$$

where, as before, we assumed reciprocity in the backward propagator and

$$m(\tau) = \int_{\mathcal{A}} \mathrm{d}\mathbf{r}_i \; \varphi(\mathbf{r}_i, \tau)\psi^*(\mathbf{r}_i, \tau), \tag{5.27}$$

is the Loschmidt echo amplitude that describes the overlap between the evolution $\psi(\mathbf{r}_i, \tau)$ in the recording stage, governed by a Hamiltonian H, and the emission

$$\varphi(\mathbf{r}_i, \tau) = \int_{\mathcal{A}} \mathrm{d}\mathbf{r}' \tilde{K}(\mathbf{r}_i, \mathbf{r}', \tau)\psi_{\mathbf{p}_0}(\mathbf{r}'), \tag{5.28}$$

that takes place in a slightly different Hamiltonian $\tilde{H}$.

Within the semiclassical perspective, the effect of the perturbation $\tilde{H} - H$ can be accounted by affecting the contribution of each trajectory s with an additional factor $\langle \exp\left[\mathrm{i}\Delta S_s/\hbar\right]\rangle$, where ΔS_s represents the action difference for traveling along s under each of the Hamiltonians. The angular brackets represent an average over the perturbation. Taking the accumulated action as a Gaussian random variable, the previous average can be expressed as

$$\langle \exp\left[\mathrm{i}\Delta S_s/\hbar\right]\rangle = \exp\left[-\left\langle \Delta S_s^2 \right\rangle /2\hbar^2\right] = \exp[-L_{\hat{s}}/2\tilde{l}], \tag{5.29}$$

with $\tilde{l}$ the effective elastic mean-free-path, *i.e.* the characteristic length traveled for the particle without feel the perturbation

$$\tilde{l} = \hbar^2 \mathrm{v}_0^2 \left(\int_{\mathcal{A}} \mathrm{d}\mathbf{q} C(\mathbf{q}) \right)^{-1}. \tag{5.30}$$

Here, v_0 is the the mean velocity and $C(\mathbf{q})$ the correlation function describing the disorder that depends on the kind of perturbation chosen. A particular choice is the *quenched disorder* model [JPa01] of N fictitious static impurities placed at positions $\mathbf{R}_\alpha$ and characterized by the correlation lenght ξ as

$$V(\mathbf{r}) = \sum_{\alpha=1}^{N} \frac{u_\alpha}{2\pi\xi^2} \exp\left[-\frac{1}{2\xi^2}(\mathbf{r} - \mathbf{R}_\alpha)^2 \right]. \tag{5.31}$$

The strenght u_α obeys $\langle u_\alpha u_\beta \rangle = u^2 \delta_{\alpha\beta}$ and for this case, the correlation function reads

$$C(|\mathbf{r} - \mathbf{r}'|) = \sum_{\alpha=1}^{N} \frac{u^2}{4\pi\xi^2} \exp\left[-\frac{1}{4\xi^2}(\mathbf{r} - \mathbf{R}_\alpha)^2 \right]. \tag{5.32}$$

It is important to note here that the chosen perturbation presents a null trace, *i.e.* no net energy is added to the unperturbed Hamiltonian. Therefore, the average writes

$$\exp[-L_{\hat{s}}/2\tilde{l}] = \exp[-\gamma\tau^2/L_{\hat{s}}], \tag{5.33}$$

where

$$\gamma = \frac{1}{2\hbar^2}\int_{\mathcal{A}} \mathrm{d}\mathbf{q} C(\mathbf{q}), \tag{5.34}$$

sets the strength of the perturbation and results independent of the trajectory.

By following the same arguments of Sec. 4.2, the diagonal approximation for the LE amplitude leads

$$m(\tau) = \frac{1}{(2\pi\hbar)^2}\int_{\mathcal{A}} \mathrm{d}\mathbf{r}_i \mathrm{d}\bar{\mathbf{r}} \sum_{s(\bar{\mathbf{r}},\mathbf{r}_i,\tau)} C_s \left\langle e^{\frac{\mathrm{i}}{\hbar}\Delta S_s}\right\rangle \rho_W(\bar{\mathbf{r}},\mathbf{p}_s). \tag{5.35}$$

Here, we consider an initial Gaussian wave packet centered in $\mathbf{r}_0$ and calculate the corresponding Wigner function as in Eq. (5.15). Furthermore, we take the stability factors and the sum rule for a close system where $\xi = 0$ and perform the $\mathbf{r}_i$ and $\bar{\mathbf{r}}$ integrals under the ergodic approach as in the previous section. Finally, the obtained amplitude writes as the integral over lenghts

$$m(\tau) = \frac{2}{(\nu\tau)^2}\int_{L_\mathrm{d}}^{\infty} \mathrm{d}L\ L\ \exp\left[-\left(\frac{L}{\nu\tau}\right)^2 - \frac{\gamma\tau^2}{L}\right], \tag{5.36}$$

where $\nu = \hbar/m\sigma$ and the second term in the exponential comes from the average over the perturbation. As a first approximation, since $L_\mathrm{d}/\nu t_1 \ll 1$ we can neglect the τ-dependence in the lower limit of the integral and thus

$$\begin{aligned} m(t_1,t_2) &= 2\frac{\mathcal{A}_N}{\mathcal{A}}\int_0^\infty \mathrm{d}\eta\ \eta \exp\left(-\eta^2\right)\int_{t_1}^{t_2}\mathrm{d}\tau \exp\left(-\frac{\gamma\tau}{\nu\eta}\right) &(5.37)\\ &= \frac{\mathcal{A}_N}{\mathcal{A}}\frac{2\nu}{\gamma}\int_0^\infty \mathrm{d}\eta\ \eta^2 \exp\left(-\eta^2\right)\left[\exp\left(-\frac{\gamma t_1}{\nu\eta}\right) - \exp\left(-\frac{\gamma t_2}{\nu\eta}\right)\right], &(5.38)\end{aligned}$$

where we replaced $\eta = L/\nu\tau$ and exchanged the order of the L and τ integrals as compared with the employed strategy of the unperturbed cases.

In the limit of $\gamma \to 0$ we trivially recover the unpertubed focalization of Eq. (4.24). The characteristic time defined by the perturbation is $\tilde{\tau} = \nu/\sqrt{\pi}\gamma$. For very weak perturbations such a time is larger than the maximum recording time, and we can expand the exponentials as

$$\exp\left(-\frac{\gamma L_i}{\nu^2\eta}\right) \simeq 1 - \frac{t_i}{\nu\eta}\gamma + \frac{1}{2!}\left(\frac{t_i}{\nu\eta}\right)^2\gamma^2, \tag{5.39}$$

and readily obtain

$$m(t_1,t_2) = \frac{\mathcal{A}_N}{\mathcal{A}}\Delta T\left(1 - \frac{\bar{t}}{\tilde{\tau}}\right) \qquad \text{for } t_2 \ll \tilde{\tau}. \tag{5.40}$$

The previous approximation is no longer valid for larger perturbations, but if we stay in the regime where the emission interval is small compared with $\tilde{\tau}$, we can assume that the

contributions of all trajectories are affected by almost the same reduction factor. Hence, we arrive to a Fermi golden rule regime where

$$m(t_1, t_2) = \frac{\mathcal{A}_N}{\mathcal{A}} \Delta T \exp\left(-\bar{t}/\tilde{\tau}\right) \qquad \text{for } \Delta T \ll \tilde{\tau}. \tag{5.41}$$

When the perturbation is strong enough to differentiate trajectories in the recording interval, the focalization will be dominated by the smallest time t_1, and we lose the proportionality between the refocused signal and the emission interval. Writing $\exp\left[-\gamma t_1/\eta\nu\right]$ as a Gaussian integral over the auxiliar variable ρ, we can cast the t_1-dependent contribution in the last term of Eq. (5.38) and follow the notes on the Appendix C that give a focalization that can also be seen as a cumulative semiclassical regime

$$m(t_1, t_2) = \frac{\mathcal{A}_N}{\mathcal{A}} \tilde{\tau}\ c_1 \exp\left(-c_2 \frac{t_1}{\tilde{\tau}}\right) \qquad \text{for } t_2 > \tilde{\tau}, \tag{5.42}$$

where the numerical constants take the values $c_1 \simeq 1.47$ and $c_2 \simeq 0.46$.

For current experimental setups, the FGR regime of Eq. (5.41) is the most relevant one. In this case, the exponential suppression of the focalized signal appears as a stringent limitation. Depending on the model chosen for the perturbation, the characteristic time $\tilde{\tau}$ might be quite different. In a Lorentz gas [CPW02, CPJ04] one might choose a perturbation represented by a *mass distortion.* In this case, the x and y components in the mass tensor of the particle is slightly modified according to

$$m_{xx} \to m(1+\alpha), \qquad m_{yy} \to \frac{m}{1+\alpha}. \tag{5.43}$$

This perturbation acts on the kinetic part of the Hamiltonian

$$\Sigma(\alpha) = \frac{\alpha}{2m}\left(\mathrm{p}_y^2 - \mathrm{p}_x^2\right), \tag{5.44}$$

and, as the quenched disorder model, also presents a null trace. Because this perturbation is nonrandom, this condition is essential so that the effect of the perturbation averages to zero by the underlying chaotic dynamics. The resulting fluctuation in the phase determines the perturbation mean-free-path

$$\tilde{l} = \frac{4\hbar^2}{m^2 \mathrm{v}_0^2 l} \frac{1}{\alpha^2}, \tag{5.45}$$

where $l \propto \lambda^{-1}$ is the elastic mean-free-path given by the unperturbed Hamiltonian and decreases as we increase the Lyapunov exponent of the system. Here, the characteristic decay given by the Fermi golden rule results

$$\frac{1}{\tilde{\tau}} = \alpha^2 \left(\frac{m\mathrm{v}_0^2}{2\hbar}\right)^2 \tau_0. \tag{5.46}$$

with $\tau_0 = l/\mathrm{v}_0$ the time between collisions (bounces) in the unperturbed system and hence $\tilde{\tau} \propto \lambda$. In this case, one could imagine this as a form of the Quantum Zeno effect, where the phase difference produced by the perturbation only accumulates along the trajectory between two collisions. Hence, more chaos implies shorter collision times and the characteristic decay decreases. This counterintuitive result states that the focalization stability increases with the degree of chaos.

In the numerical evaluation of the focalization signal in terms of the Loschmidt echo amplitude (LE), we compute both the forward and backward evolutions of the whole system during a period t_R. By considering the initial time fixed at the origin ($t_1 = 0$) and taking $t_2 = t$, the focalization $m(0,t)$ is then calculated as the integral between 0 and t of the overlap between both evolutions, *i.e.* the time integral of the LE. We compare this with the corresponding focalization obtained from the Lanczos-Trotter method of Sec. 4.6, where the detected wave at the transducer site is injected during the emission interval $\Delta T = t - 0$.

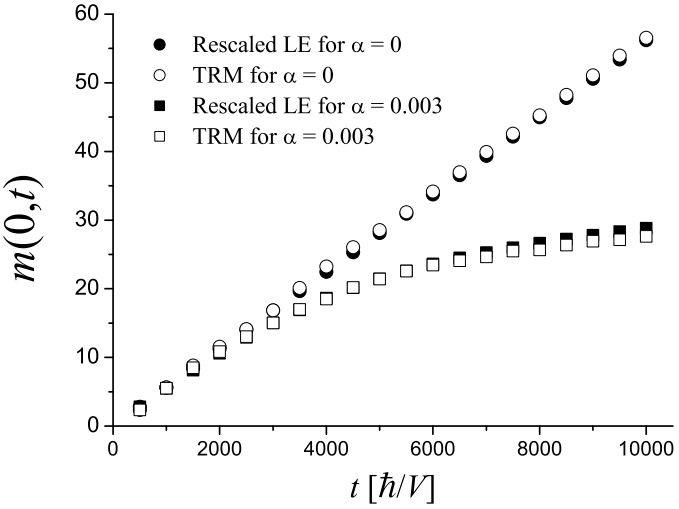

Figure 5.2: Focalization functions (circles) and the rescaled Loschmidt echo (squares) amplitude as a function of time for two different values of the perturbation.

As we show in Fig. 5.2, the focalization signal and the rescaled time integral of the LE (see Eq. (5.26)) are contrasted for several values of t. Here, the system consists of a quarter of Bunimovich stadium and the chosen perturbation is a distortion on the mass tensor. For the unperturbed case, the focalization (open circles) and the LE (black circles) manifest the expected linear scaling with ΔT of Eq. (4.24). For the perturbed case with $\alpha = 0.003$, the focalization (open squares) and the LE (black squares) no longer grow linearly and follow the time regimes discussed above. In both cases, the agreement between this two quantities highlights that the focalization does not depend on the transducer location and

can be faithfully reproduced through the time integral LE.

As pointed out in Ref. [CLP06], the fluctuations that occur in the action integral along a classical trajectory can be assumed as self-averaged due to the ergodic nature of the unperturbed Hamiltonian. Hence, the generic properties of the LE amplitude does not change significatively with the kind of perturbation and we can get a qualitative estimation of the time regimes in the focalization.

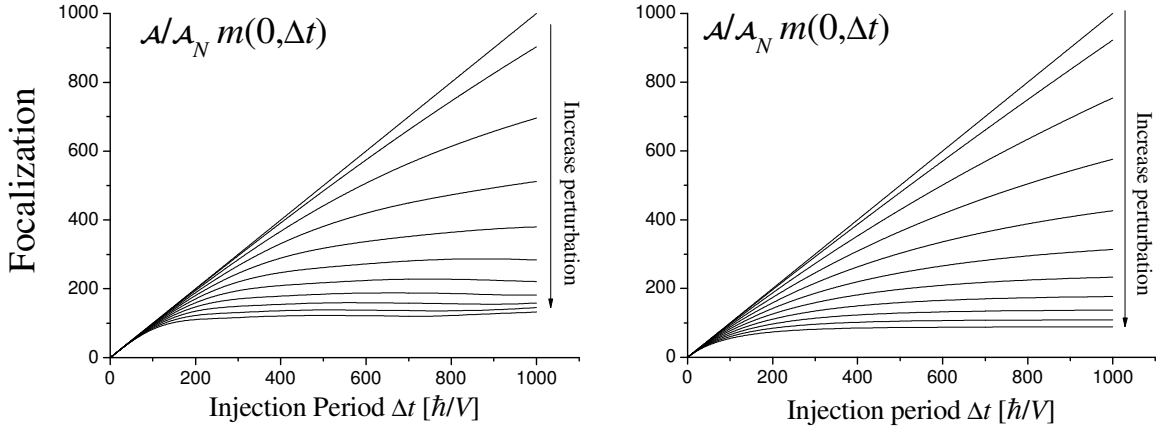

Figure 5.3: Rescaled focalization as a function of the recording interval for different strenghts in the perturbation. Left panel: numerical results for α from 0 to 0.01 in steps of $\Delta\alpha = 0.001$. Right panel: numerical integration of Eq. (5.38) for some representative values of γ.

In Fig. 5.3 we show the resulting focalization for several values of the perturbation. The distortion in the mass tensor, and consequently the variation in the kinetic energy of the particle, can be numerically represented by a smooth modification between the verticals and horizontal hoppings. In this example, we use as initial state a Gaussian wave packet centered at some arbitrary point $\mathbf{r}_0$, whose momentum p_0 points in all possible directions according to

$$\psi_{\mathrm{p}_0}(\mathbf{r}) = \frac{1}{\sqrt{\pi}\sigma} \exp\left[-\frac{(\mathbf{r}-\mathbf{r}_0)^2}{2\sigma^2}\right] \int_0^{2\pi} \frac{\mathrm{d}\varphi}{2\pi} \exp\left[\frac{\mathrm{i}}{\hbar}\mathrm{p}_0\,|\mathbf{r}-\mathbf{r}_0|\cos\varphi\right]. \tag{5.47}$$

By using the Jacobi-Anger expansion

$$e^{\mathrm{i}z\cos\varphi} = J_0(z) + 2\sum_{n=1}^{\infty} i^n J_n(z)\cos(n\varphi), \tag{5.48}$$

with $J_n(z)$ the n-th order Bessel function, the above integral over angles yields

$$\psi_{\mathrm{p}_0}(\mathbf{r}) = \frac{1}{\sqrt{\pi}\sigma} \exp\left[-\frac{(\mathbf{r}-\mathbf{r}_0)^2}{2\sigma^2}\right]\; J_0\left(\frac{\mathrm{p}_0\,|\mathbf{r}-\mathbf{r}_0|}{\hbar}\right). \tag{5.49}$$

This last may be an interesting choice since this initial state preserves the time-reversal symmetry and, simultaneously, it contains finite value in the momentum.

According to the left panel of the figure, the focalization grows almost linearly in a time scale that is very small as compared with $\tilde{\tau}$. Afterwards, there is a clear attenuation that follows the FGR of Eq. (5.41) and it finally arrives to a "fluctuating" region around a mean value that depends on the strenght of the perturbation. The analogous focalization is depicted in the right panel for some representative values of γ through the numerical evaluation of Eq. (5.38). Of course, the comparison between the numerical results (left panel) and Eq. (5.38) (right panel) is only qualitative since the considered perturbation is not the same . In turn, when considering strong perturbations, the diagonal approximation may no longer fit and higher order corrections should be included.

5.3 Summary

In summary, we evaluated the stability of the focalization signal against irreversibility processes for two different situations: the open chaotic cavity, where the decay in the nonescape probability may be interpreted as that produced by a non Hermitian perturbation; and the closed chaotic system, where the emission stage was performed in a slightly perturbed Hamiltonian with respect to that of the registration stage.

When considering an open cavity, the focalization constitutes a time integral of the nonescape probability, that appears as the key tool in the assesment of the decaying excitations. Working under the semiclassical approach, we evaluated such quantity in the diagonal approximation leading to a form of Fermi golden rule. This probability shown to decay exponentially with the classical escape rate $1/\tau_d$, limiting the focalization intensity. Numerical results showed a good agreement with the theory for those times in the registration and emission stages where the norm of the wave packet remains almost constant. For larger times, additional terms in the semiclassical expansion should be included in order to describe the attenuation in the decay. Among them, we recall to those waves returning to the cavity from the environment as well weak-localization type mechanisms related to pairs of correlated trajectories not included in the diagonal approximation.

On the other hand, we studied the stability in the focalization following the strategy popularized by the Loschmidt echo (hasty daemon), *i.e.* considering that the recording and emission phases are governed by slightly different Hamiltonians. As perturbation we choose the quenched disorder model, consisting of a null trace potential of impurities randomly located around the cavity. For this case, the focalization showed two time regimes depending on the strength of the perturbation and the center of the emission interval. For weak perturbations and periods of emission short enough so that the contributing trajectories are affected for the same reduction factor (*i.e.* $\Delta T \ll \tilde{\tau}$, with $\tilde{\tau}$ the characteristic time of the perturbation), it appears a Fermi golden rule that yields the attenuation in the focalization. As shown in Eq. (5.41), the FGR maintains the scaling of the focalization with the emission interval as in the unpertubed cases of Chapter 4. When the perturbation is strong enough to differentiate trajectories in the emission interval, the last regime

is lost and the focalization will only depend on the initial recording time. Among these regimes, the FGR regime appears as the one related with the typical TRM experiments. In particular, previous work on the subject has shown that this regime also describes the LE amplitude (and hence the focalization) in a perturbation consisting of a distortion of the mass tensor [CLP06]. As a consequence, we obtained an increasing stability in the focalization against the perturbation with the degree of chaos in the system. This counterintuitive result may represent a key point in the experimental applications of the TRM in chaotic or inhomogeneous systems.

Chapter 6

Conclusions

In this thesis we addressed, in a completely new perspective, the time reversal mirror (TRM) procedure, where escaping waves are recorded as they cross the frontier between the cavity and a propagating region and then re-emitted to achieve time reversal. This consists in proposing the time reversed function inside the cavity as the target function of the injection process. This inverse time scattering approach led to the development of the perfect inverse filter (PIF), a prescription for processing the recorded information that compensates any feedback and ensures the exact time reversal of the dynamics of acoustic and quantum waves. We have also developed a novel strategy, based in the wave-particle duality intrisic in a linear wave equation, to analyze the dynamical stability of the TRM against imperfections in the protocol and perturbations in the evolution operator.

In the first part of the thesis, we developed the PIF procedure for quantum waves in the discrete form of the Schrödinger equation. This particular choice of the system gave us a natural separation between the region where one attempts to perform the reversal (the cavity) and the "uncontrolled" outer region that acts as a sort of environment. At the same time, the discrete representation of the Dyson equation yields a non-perturbative connection between the independent solutions in both regions. This provides the precise injection function that produces the targeted dynamics inside the cavity. The PIF prescription appears as a filter applied to the TRM that accounts for the available information on the dynamics. On the one hand, when the initial excitation arrives from the outer region and one is able to detect the complete propagation of the wave packet as it goes in and out through the boundaries of the system, the PIF filter accounts for the feedback of the system. The PIF is accomplished in the energy/frequency representation through the multiplication by the inverse of the Green's function at the location of the transducer. On the other hand, if the recording starts when the excitation is already inside the cavity, we obtained a simpler prescription. In this case, the PIF became independent from the internal scattering and only accounts for the group velocity of the waves that escape towards the outer region. The key in this last case is that one can separate the incoming and outgoing components of the wave packet. Since this is often the situation in linear systems, this result is very promisory. It can also hold for situations when the separation cannot be fulfilled exactly. The PIF prescription could be used as an analytical tool to design

the generation of specific wave packet like excitations, thus providing another strategy for coherent control. In particular, it could be applied for the development of quantum bazookas shutting wave packet excitations. Fields of prospective implementation include the local generation [ZME92] of target spin-wave packets in chains of interacting spins [MBS97]. In nanoelectromechanical structures [ABS02, SRo05], where a vibrational wave is created by coupling the nanocantilever to a Cooper-pair box, the PIF prescription could allow the design of particular superposition states in the resonator. Also, in Bose-Einstein condensates, where the atoms are confined in an optical lattice [Chu02], the well-defined set of quantum states might be described by a tight-binding model. Thus, the control of macroscopic wavefunctions would benefit from a simple and consistent PIF prescription for the local generation of any targeted excitation.

In Chapter 3, we developed the PIF protocol for acoustic waves. Again, this was possible because we resorted to the discrete form of the wave equation represented by an harmonic lattice of coupled oscillators. Through a detailed analysis of the propagators describing the response of the system due to impulsive and displacive forces, we found the connection between the quantum and classical Green's functions. This enabled us to inject instantaneous increments in either the displacements or velocities of the oscillators at the frontier, obtaining the targeted evolution inside the cavity. After that, the classical PIF was deduced through the Dyson equation connecting the two subspaces delimited by the transducer. Notably, the prescription resulted the same as that in the quantum case, *i.e.* just determined by the group velocity. When the outer region, usually a waveguide, presents periodicity or scattering due to impurities, the PIF improves the TRM because in both cases the group velocity is non-constant. In particular, the prescription suggests that, in the continuum limit, the usual TRM experimental set-up reaches the exact reversal whenever the outer region is free of inhomogeneities. Inspired by the Trotter method implemented in the evaluation of the quantum PIF, we developed a novel numerical method, the Pair Partitioning, that generates the time evolution propagator by alternating the perfectly reversible evolution of pairs of coupled oscillators. We also added a modification that enabled the description of the evolution in open systems through the use of frictional forces near the boundaries of a finite system. We expect that the computing power of the Pair Partitioning in multi-dimensional systems could be further improved by applying this method in conjunction with the Lanczos algorithm (see Sec. 4.6).

In general, the PIF results valid for the reversal of any scalar wave as long as they satisfy a linear equation where different propagators can be described by the Green's functions. The basic ingredients apply to elastic or electromagnetic waves [MBB00] extending the range of applicability of the concepts introduced here.

Although the implementation of a TRM in a quantum system is not a simple task, at least some of the steps in our protocol could be implemented in pulsed NMR. This technique already has the tools that enable to inject and detect locally a polarization wave [MBS97]. In an ensemble of linear molecules, the interactions between nuclear spins can be manipulated to obtain a polarization assimilable to the square modulus of a single-particle wave function [PLU95] and constitutes a pseudo-pure state [DPL04]. Detection at

each time involves repeated experiments where the polarization and its phase are obtained from an ensemble measurement. In order to generate a local source/detector one resorts to the interaction between different nuclei, which can be engineered at will, *e.g.* a ^{13}C acts as such probe for a labeled ^{1}H [ZME92]. In fact, the group of Levstein and Pastawski have been able to inject a wave packet in a ^{1}H ring and to follow its dynamics detecting simultaneously the amplitude and relative phase at the labeled ^{1}H [LUP98]. This is a double-slit like experiment that allows interferometry in the time domain [PUL96]. If most of the polarization stays in the ^{13}C, the small portion transferred to the proton system is the one described by the theory above.

While a full implementation of the quantum TRM or PIF requires setting many important experimental details, every step towards that goal would have potential use in spectral edition and quantum information processing. More immediately, classical wave systems could benefit from our procedures which can be incorporated in a straightforward manner.

In the second part of this thesis, we evaluated the TRM procedure in a closed chaotic cavity for small emission periods ΔT as compared to the complete recorded signal, which the experiments have shown to provide a satisfactory time reversal. Under the semiclassical approximation, we described the focalization amplitude for times and positions close to those where refocusing occurs. In agreement with the elastic waves experiments [DFi97], we observed that the use of a single transducer is enough to perform a high-quality reversion. Furthermore, this focalization has shown to be directly proportional to the emission period and the number of transducers, and inversely proportional to the total area of the cavity. Assuming an ergodic cavity, the information carried out by the detected signal becomes "redundant", meaning that the same focalization might be achieved, independently of where the transducers are located or when the emission window is active. As we can expect, this is not the case for cavities with integrable dynamics, where the classical trajectories tend to be dominated by the recurrences of a few periodic orbits leading to periods of "silence" with alternating bursts of signal during the registration. In consequence, the signal may be tracked or not, depending on where the transducer is placed or when it is active. At best, when some portion of the wave packet is detected, the resulting focalization presents low contrast.

In order to obtain a well resolved focalization, the recording time should increase with the size of the cavity. In a numerical implementation in a system of $N \times N$ sites this implies long computational times since it requires the computation of the complete propagator involving $\mathcal{O}(N \times N)$ operations with the Trotter-Suzuki algorithm. To reduce the time required to evaluate the fidelity of the time reversal focusing, we developed the Lanczos-Trotter algorithm. This redefines a new basis through the repeated application of the Hamiltonian over the initial state. This procedure collects relevant information about the dynamics of the wave packet at the site of the transducer. Since the recording stage starts and ends in times of the order of the mesoscopic echo, the truncation of the Lanczos basis at the order N reproduces the signal in the transducer. In consequence, the Lanczos-Trotter method improves the Trotter-Suzuki algorithm when considering the TRM procedure for a single transducer. At the moment, the application of this method

is restricted in systems presenting time-reversal symmetry. However, the generalization of the Lanczos-Trotter to open systems seems possible by including an "escape region" composed by complex site energies.

In Chapter 5, we analized the stability of the TRM procedure in a chaotic cavity against external perturbations. We started considering that the cavity has a small opening which allows the escape of the internal excitations towards the outside world, usually a waveguide or a boundless system. This can be seen as a non-Hermitian perturbation acting on both recording and emission stages. Under the ergodic hypothesis, the focalization becomes independent from the position of the transducer and can be expressed as the time integral of the nonescaping probability to find the excitation still confined inside the cavity. We described this probability in the semiclassical approximation and obtained an exponential decay regime when the number of contributing trajectories remain unaffected by the opening. In this case, the focalization intensity preserves the linear scaling with the emission interval but presents a natural attenuation given by those non-returning trajectories that escaped at the recording time. As we increase the recording and emission intervals, a cumulative semiclassic regime appears. At this point, the focalization grows until a stationary value which is reached in a time characterized by the decay of the wave packet. Here, the number of contributing trajectories drops steadily and the linear scaling with the emission interval is lost.

Inspired by the Loschmidt echo strategy, we evaluated the TRM procedure in a closed chaotic cavity under an external Hermitian perturbation introduced between the recording and emission stages. For this case, the ergodic hypothesis provided the description of the focalization amplitude as the time integral of the Loschmidt echo amplitude during the emission period. We considered a null trace potential consisting of a random arrengement of "Gaussian" impurities and followed the same semiclassical arguments as in the open cavity. Depending on the strenght of the perturbation, we found two regimes in the focalization amplitude. For weak perturbations and short emission periods, the contributing trajectories "feel" the perturbation for almost the same period and the focalization presents a Fermi golden rule regime. In this case, the scaling with the emission period is still linear and the decay time of the attenuation goes inversely proportional to the strenght of the perturbation. For strong perturbations, the contributing trajectories separate according to the traveling time and the focalization shows a cumulative semiclassical regime where refocusing no longer depends neither on the width nor on the center of the emission period. The typical TRM experiments are in the FGR regime, since the recording and emission periods are usually short as compared with the characteristic time of the perturbation. In agreement with the Loschmidt echo regimes of Ref. [CPJ04], the FGR has a characteristic decay time proportional to the Lyapunov exponent. This counterintuitive result, a form of the Quantum Zeno effect, results in a more stable TRM with increasing the randomness or chaos. Thus, this is a leap towards the understanding of why chaos enhances the robustness of the TRM which deserves further numerical and experimental studies.

In summary, the analytical and numerical results of this thesis provide new insights that should lead to improved TRM implementations in acoustics and electromagnetic

communications and also could open new possibilities in the control of quantum excitations. The potential of the PIF strategy may result of interest in ultra-cold atoms and quantum information fields, requiring the coherent control of specific target excitations of well-defined quantum states. Furthermore, we presented a novel analysis of the stability of TRM against external perturbations. In the field of quantum chaos, the similarity observed between both hasty and stubborn daemons gives rise to a natural question: Why the TRM experiments does not seem to present a Lyapunov regime as those in the LE? This question opens new opportunities for further analytical, numerical and experimental studies.

Appendix A

Calculus of Green's functions through decimation

A.1 Quantum Green's functions

In this Appendix, we give a detailed description for the decimation process as a useful technique in the calculation of the Green's function $G_{s,s}(\varepsilon)$ in the site basis. As shown in Fig. A.1, we start with a one-dimensional system composed by 3 sites and we would like to calculate the Green's function of the transducer placed at the left of the chain, referred as the site 1. Hence, the system's Hamiltonian is represented by the tridiagonal matrix

$$\mathbb{H} = \begin{pmatrix} E_1 & V_{1,2} & 0 \\ V_{2,1} & E_2 & V_{2,3} \\ 0 & V_{3,2} & E_3 \end{pmatrix}, \tag{A.1}$$

and the corresponding Schrödinger equation writes according to $(\varepsilon\mathbb{I} - \mathbb{H})\,|\psi\rangle = 0$, *i.e.*

$$\begin{aligned} (\varepsilon - E_1)\psi_1 - V_{1,2}\psi_2 &= 0, & \text{(A.2)} \\ (\varepsilon - E_2)\psi_2 - V_{2,1}\psi_1 - V_{2,3}\psi_3 &= 0, & \text{(A.3)} \\ (\varepsilon - E_3)\psi_3 - V_{3,2}\psi_2 &= 0. & \text{(A.4)} \end{aligned}$$

The first step in order to reduce the number of sites in the system can be achieved by computing the middle equation in terms of the last one. This yields,

$$(\varepsilon - \tilde{E}_2)\psi_2 - V_{2,1}\psi_1 = 0, \tag{A.5}$$

that may be interpreted as the effective site 2 whose energy

$$\tilde{E}_2 = E_2 + V_{2,3}\frac{1}{\varepsilon - E_3}V_{3,2}, \tag{A.6}$$

carries the correction due to the presence of the site 3. The dynamical correction $(\varepsilon - E_3)^{-1}$ accounts for the Green's function $G^{(0)}_{3,3}(\varepsilon)$ of the uncoupled site 3. Reducing again, the

resulting Schrödinger equation takes the following form

$$(\varepsilon - \tilde{E}_1)\psi_1 = 0, \tag{A.7}$$

where

$$\tilde{E}_1 = E_1 + \Sigma_R(\varepsilon) = E_1 + V_{1,2}\frac{1}{\varepsilon - E_2 - V_{2,3}\dfrac{1}{\varepsilon - E_3}V_{2,1}}V_{2,1}, \tag{A.8}$$

contains the self-energy correction $\Sigma_R(\varepsilon)$ given by the sites 2 and 3 respectively.

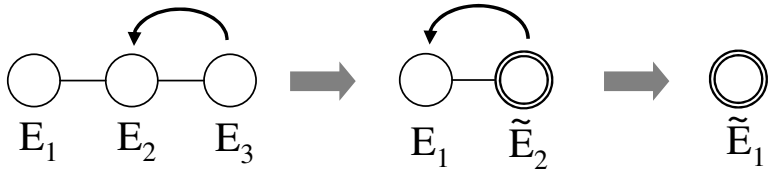

Figure A.1: Scheme of the decimation method. The effective energies $\tilde{E}_i$ contains the self-energy correction due to the decimated sites at the right side of the chain.

Now that we have decimated the 3 sites system into a single effective site, the Green's function is readily obtained by calculating

$$G_{1,1}(\varepsilon) = (\varepsilon - \tilde{E}_1)^{-1} = \frac{1}{\varepsilon - E_1 - V_{1,2}\dfrac{1}{\varepsilon - E_2 - V_{2,3}\dfrac{1}{\varepsilon - E_3}V_{2,1}}V_{2,1}}. \tag{A.9}$$

In a more general situation where the transducer is placed between the cavity and the outer region, a decimation should be accounted at both sides of the s-site. For the cavity, placed at the left of s, it is important to note that the number of sites is finite and hence the self-energy correction $\Sigma_{\text{in}}(\varepsilon)$ consist of a finite number of continued fractions. On the other hand, when considering the outer region as an homogeneus chain where all the energies and hoppings are E_{o} and V respectively, the correction to the self energy corresponding to the n-site can be written in terms of the correction in the $(n+1)$-site as

$$\Sigma_{\text{out}}^{(n)}(\varepsilon) = \frac{V^2}{\varepsilon - E_{\text{o}} - \Sigma_{\text{out}}^{(n+1)}(\varepsilon)}. \tag{A.10}$$

Hence, in the thermodynamic limit where the number of sites increases indefinitely, this correction can be assumed the same as that given by the $(n+1)$-site. Therefore, this can be represented through the recurrence

$$\Sigma_{\text{out}}(\varepsilon) = \frac{V^2}{\varepsilon - E_{\text{o}} - \Sigma_{\text{out}}(\varepsilon)}, \tag{A.11}$$

whose solution comes from the quadratic equation

$$\Sigma_{\rm out}^2(\varepsilon) - (\varepsilon - E_{\rm o})\,\Sigma_{\rm out}(\varepsilon) + V^2 = 0, \tag{A.12}$$

and the chosen branches are in agreement with the limit of the analytic continuation $\varepsilon \to \varepsilon + {\rm i}\eta$ of the *retarded* Green's function in a finite system:

$$\Sigma_{\rm out}(\varepsilon) = \lim_{\eta\to 0}\lim_{n\to\infty} \frac{V^2}{\varepsilon + {\rm i}\eta - E_{\rm o} - \Sigma_{\rm out}^{(n)}(\varepsilon)} \tag{A.13}$$

$$= \Delta(\varepsilon) - {\rm i}\Gamma(\varepsilon) \tag{A.14}$$

with

$$\Delta(\varepsilon) = \begin{cases} \frac{\varepsilon-E_{\rm o}}{2} + \sqrt{\left(\frac{\varepsilon-E_{\rm o}}{2}\right)^2 - V^2} & \frac{\varepsilon-E_{\rm o}}{2V} < -1 \\ \frac{\varepsilon-E_{\rm o}}{2} & \frac{|\varepsilon-E_{\rm o}|}{2V} \le 1 \\ \frac{\varepsilon-E_{\rm o}}{2} - \sqrt{\left(\frac{\varepsilon-E_{\rm o}}{2}\right)^2 - V^2} & \frac{\varepsilon-E_{\rm o}}{2V} > 1 \end{cases}, \tag{A.15}$$

and

$$\Gamma(\varepsilon) = \begin{cases} \sqrt{V^2 - \left(\frac{\varepsilon-E_{\rm o}}{2}\right)^2} & \frac{|\varepsilon-E_{\rm o}|}{2V} \le 1 \\ 0 & \frac{|\varepsilon-E_{\rm o}|}{2V} > 1 \end{cases}. \tag{A.16}$$

in agreement with Eqs.(2.70) and (2.71) from the text.

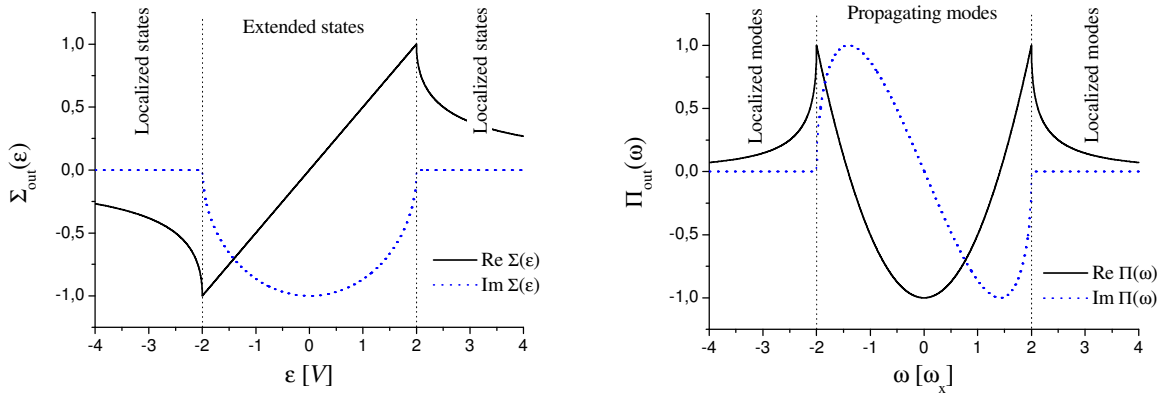

Figure A.2: Corrections to the self energy (left) and the characteristic frequency (right) due to the an open one-dimensional and semi-infinite chain. The real (black solid) and imaginary (blue dotted) are plotted.

A.2 Classical Green's functions

In the classical description of coupled harmonic oscillators, the same procedure can be accomplished in the elements of resolvent matrix of Eq. (3.12). In such case, the displace-

ments in the frequency domain for a chain of three coupled oscillators write

$$(\omega^2 - \tilde{\omega}_1^2)u_1(\omega) + \frac{K_{1,2}}{m_1}u_2(\omega) = 0, \tag{A.17}$$

$$(\omega^2 - \tilde{\omega}_2^2)u_2(\omega) + \frac{K_{1,2}}{m_2}u_1(\omega) + \frac{K_{2,3}}{m_2}u_3(\omega) = 0, \tag{A.18}$$

$$(\omega^2 - \tilde{\omega}_3^2)u_3(\omega) + \frac{K_{2,3}}{m_3}u_2(\omega) = 0. \tag{A.19}$$

Therefore, we can decimate as before by including the third equation into the second one

$$\left(\omega^2 - \tilde{\omega}_2^2 - \frac{K_{2,3}}{m_2}\frac{1}{\omega^2 - \tilde{\omega}_3^2}\frac{K_{2,3}}{m_3}\right)u_2(\omega) + \frac{K_{1,2}}{m_2}u_1(\omega) = 0. \tag{A.20}$$

Here, in addition to the mean-field or static frequency in $\tilde{\omega}_2^2$, it appears a dynamical correction in the effective frequency due to the coupling with the third oscillator. If we reduce again, the effective equation in the first oscillator would read

$$(\omega^2 - \Omega_1^2)u_1(\omega) = 0, \tag{A.21}$$

with

$$\Omega_1^2 = \omega^2 - \tilde{\omega}_1^2 - \frac{K_{1,2}}{m_1}\frac{1}{\omega^2 - \tilde{\omega}_2^2 - \frac{K_{2,3}}{m_2}\frac{1}{\omega^2 - \tilde{\omega}_3^2}\frac{K_{2,3}}{m_3}}\frac{K_{1,2}}{m_2}. \tag{A.22}$$

For the case of an open homogeneous chain, the correction $\Pi(\omega)$ to the characteristic frequency obeys the same recurrence law than in the tight-binding case, *i.e.*

$$\Pi(\omega) = \frac{\omega_{\mathrm{x}}^4}{\omega^2 - 2\omega_{\mathrm{x}}^2 - \Pi(\omega)}, \tag{A.23}$$

where $\omega_{\mathrm{x}}^2 = K/m$ is the exchange frequency. Thus, the solution $\Pi(\omega) = \Delta(\omega) - \mathrm{i}\omega\eta(\omega)$ is obtained by chosing the branches as

$$\Delta(\omega) = \begin{cases} \frac{\omega^2 - 2\omega_{\mathrm{x}}^2}{2} + \frac{\omega}{2}\sqrt{\omega^2 - 4\omega_{\mathrm{x}}^2} & \omega < -2\omega_{\mathrm{x}} \\ \frac{\omega^2 - 2\omega_{\mathrm{x}}^2}{2} & |\omega| \leq 2\omega_{\mathrm{x}} \\ \frac{\omega^2 - 2\omega_{\mathrm{x}}^2}{2} - \frac{\omega}{2}\sqrt{\omega^2 - 4\omega_{\mathrm{x}}^2} & \omega > 2\omega_{\mathrm{x}} \end{cases} \tag{A.24}$$

and

$$\eta(\omega) = \begin{cases} \frac{1}{2}\sqrt{4\omega_{\mathrm{x}}^2 - \omega^2} & |\omega| \leq 2\omega_{\mathrm{x}} \\ 0 & |\omega| > 2\omega_{\mathrm{x}} \end{cases}, \tag{A.25}$$

that yields the relation with the group velocity as

$$v_g(\omega) = c\sqrt{1 - \left(\frac{\omega}{2\omega_{\mathrm{x}}}\right)^2} = a\eta(\omega). \tag{A.26}$$

in agreement with Eq. (3.7) of the text.

Appendix B

Quantum-classical analogy in discrete systems

In this appendix, we show some similarities in the algebraic structure of the discrete quantum and classical wave equations given in Eqs. (2.6) and (3.12) respectively. We introduce a tight-binding model in the quantum domain enabling the description of the classical equation and obtain the same dynamics as that given by the harmonic chains. In this model, we re-adapt the hoppings and number of sites of the quantum system in order to account for the elastic couplings and the natural frequencies in the corresponding harmonic system.

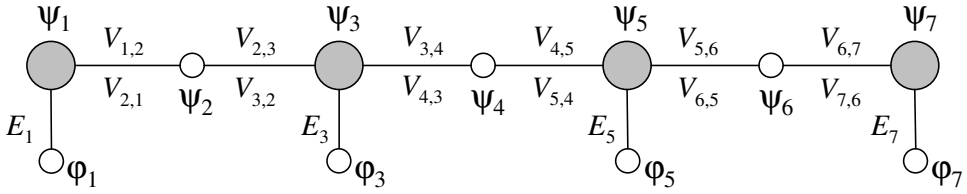

Figure B.1: Tight-binding analogy with the classical chain of coupled harmonic oscillators.

We show in Fig. B.1 as the gray sites those who will compute the movement of the i-th oscillator due to an initial displacement following the Eq. (3.18). They are connected by the "auxiliary" white sites representing the harmonic couplings given by the springs. The natural frequency $\omega_i = E_i/\hbar$ is obtained through the vertical hopping that links the corresponding auxiliary state $\varphi_i(\varepsilon)$ and the horizontal hoppings yield the elastic coupling between the other oscillators. Under these assumptions, the Schrödinger equation for the gray sites takes the form

$$\varepsilon\psi_i(\varepsilon) - E_i\varphi_i(\varepsilon) - V_{i,i-1}\psi_{i-1}(\varepsilon) - V_{i,i+1}\psi_{i+1}(\varepsilon) = 0, \tag{B.1}$$

with the auxiliary states satisfying

$$\begin{aligned} \varepsilon\varphi_i(\varepsilon) - E_i\psi_i(\varepsilon) &= 0, && \text{(B.2)} \\ \varepsilon\psi_{i-1}(\varepsilon) - V_{i-1,i-2}\psi_{i-2}(\varepsilon) - V_{i-1,i}\psi_i(\varepsilon) &= 0, && \text{(B.3)} \\ \varepsilon\psi_{i+1}(\varepsilon) - V_{i+1,i}\psi_i(\varepsilon) - V_{i+1,i+2}\psi_{i+2}(\varepsilon) &= 0. && \text{(B.4)} \end{aligned}$$

Notice that the subspace formed by the gray states is a suitable representation of the displacements amplitudes since they only will take real values (the imaginary components will remain as zero). As we can observe, all the site energies were set as exact zeros. In consequence, the expansion in the the time evolution propagator

$$\begin{aligned} |\psi(t)\rangle &= \exp\left(-\frac{\mathrm{i}}{\hbar}\mathbb{H}t\right)|\psi(0)\rangle && \text{(B.5)} \\ &= \sum_{n=0}^{\infty}\frac{(-1)^n}{(2n)!}\left(\frac{t}{\hbar}\right)^{2n}\mathbb{H}^{2n}|\psi(0)\rangle - \mathrm{i}\sum_{n=0}^{\infty}\frac{(-1)^n}{(2n+1)!}\left(\frac{t}{\hbar}\right)^{2n+1}\mathbb{H}^{2n+1}|\psi(0)\rangle\,, && \text{(B.6)} \end{aligned}$$

and the tridiagonal character of the Hamiltonian yields

$$\begin{aligned} \left[\mathbb{H}^{2n}\right]_{i,j} &= 0, \qquad i \text{ and } j \text{ with different parity}, && \text{(B.7)} \\ \left[\mathbb{H}^{2n+1}\right]_{i,j} &= 0, \qquad i \text{ and } j \text{ with same parity}. && \text{(B.8)} \end{aligned}$$

Furthermore, the non-zero values are real numbers since we assume that the hoppings are real. Hence, if the initial state is a linear combination of real components in the gray sites, the time evolution in these sites will contain only the $\mathbb{H}^{2n}$ expansion and therefore they will not change their phase.

By using a decimation procedure in the auxiliary white sites, one can reduce the Eqs. (B.2)-(B.4) considering only the wave functions that refers to the displacements of the oscillators. Therefore, the effective energies and hoppings are

$$\left(\varepsilon - \frac{\tilde{E}_i^2}{\varepsilon}\right)\psi_i(\varepsilon) - \frac{V_{i,i-1}V_{i-1,i-2}}{\varepsilon}\psi_{i-2}(\varepsilon) - \frac{V_{i,i+1}V_{i+1,i+2}}{\varepsilon}\psi_{i+2}(\varepsilon) = 0, \qquad \text{(B.9)}$$

where $\tilde{E}_i^2 = V_{i,i-1}V_{i-1,i} + E_i^2 + V_{i,i+1}V_{i+1,i}$ is the "effective" energy at the i-site. Since the exchange frequencies in the off-diagonal components of Eq. (3.12) appear as positive and the correction terms in the diagonal are just the exchange frequencies, the following restriction

$$\begin{aligned} V_{i,i-1}V_{i-1,i} &= -V_{i,i-1}V_{i-1,i-2}, && \text{(B.10)} \\ V_{i,i+1}V_{i+1,i} &= -V_{i,i+1}V_{i+1,i+2}. && \text{(B.11)} \end{aligned}$$

is satisfied whenever $V_{i-1,i-2} = -V_{i-1,i}$ and $V_{i+1,i+2} = -V_{i+1,i}$. As compared with the classical case, these terms can be chosen in order to coincide with the exchange frequencies

as

$$\frac{V_{i,i-1}V_{i-1,i}}{\hbar^2} = \frac{K_{i-2,i}}{m_i}, \tag{B.12}$$

$$\frac{V_{i,i+1}V_{i+1,i}}{\hbar^2} = \frac{K_{i,i+2}}{m_i}. \tag{B.13}$$

It is important to notice that such replacement, in the inhomogeneous case, breaks the reciprocity property of the propagators, *i.e.* $G_{i,j}(t) \neq G_{j,i}(t)$. With this in mind, the resulting Green's function matrix acquires the same structure than in the classical case and it allows the representation of the displacements in terms of the wave amplitude of the TB model.

In order to test this analogy, we solve the evolution of a single-mode Helmholtz resonator composed by a heavy mass m_0 and a natural frequency ω_0, and located at the site c. This oscillator is coupled to two homogeneous harmonic chains of lighter masses m acting as the "environment" where all the excitation decays. In the tight-binding model, the relations imposed by Eqs. (B.10)-(B.13) are satisfied by setting the hoppings as

$$V_{c,c-1} = -\hbar\frac{m}{m_0}\sqrt{\frac{K}{m}} \rightarrow V_{c-1,c} = -\hbar\sqrt{\frac{K}{m}}, \tag{B.14}$$

$$V_{c,c+1} = \hbar\sqrt{\frac{K}{m}} \rightarrow V_{c+1,c} = \hbar\frac{m}{m_0}\sqrt{\frac{K}{m}}. \tag{B.15}$$

We start with an initial displacive force applied in the resonator and observe the displacement in several sites of the chain. The quantum evolution is computed through the Trotter-Suzuki algorithm and the classical propagation is calculated using the Pair Partitioning method discussed in Sec. 3.3. According to Fig. B.2, a complete agreement between the two evolutions is observed.

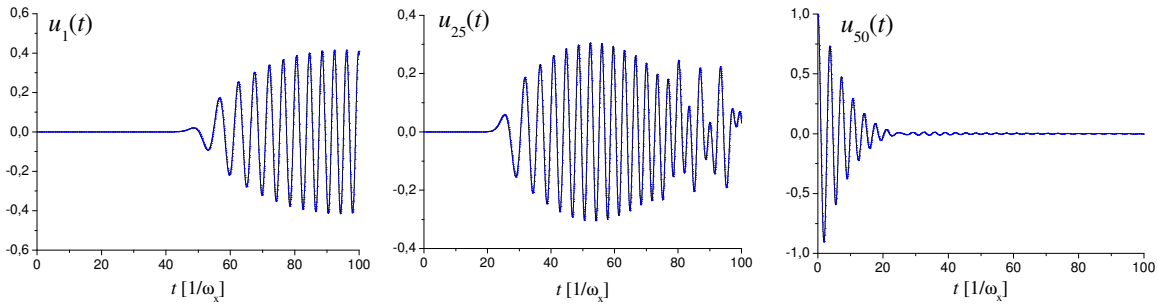

Figure B.2: Numerical test for a Helmholtz resonator with $m_0 = 4m$ and $\omega 0 = 1.5\omega_x$ located in $x = 50a$. The normalized quantum evolutions (blue dotted) and the classical displacements (black solid) are superposed.

Although the classical dynamics is obtained from the Trotter-Suzuki method with high accuracy, is important to take this result carefully: this comparison only concerns to the

algebraic properties of the Green's functions and hence, it does not involve any physical interpretation beyond the formal description of the propagators.

Appendix C

Calculus of integral identities

C.1 Scaling of the focalization

In this appendix we calculate the integral over angles

$$\mathcal{I}_3 = \int_0^{2\pi} \frac{\mathrm{d}\varphi}{2\pi} K\cos\varphi e^{K^2\cos^2\varphi}\mathrm{erf}\left(K\cos\varphi\right), \tag{C.1}$$

presented in Eq. (4.37) of the text. The Taylor expansion in the corresponding integrand gives

$$e^{K^2\cos^2\varphi} = \sum_{n=0}^{\infty} \frac{\left(K\cos\varphi\right)^{2n}}{n!}, \tag{C.2}$$

for the exponential and

$$\begin{aligned}
\mathrm{erf}\left(K\cos\varphi\right) &= \frac{2}{\sqrt{\pi}}\int_0^{K\cos\varphi} e^{-x^2}\mathrm{d}x & \text{(C.3)}\\
&= \frac{2}{\sqrt{\pi}}\sum_{m=0}^{\infty}\frac{(-1)^m}{m!}\int_0^{K\cos\varphi} x^{2m}\mathrm{d}x & \text{(C.4)}\\
&= \frac{2}{\sqrt{\pi}}\sum_{m=0}^{\infty}\frac{(-1)^m\left(K\cos\varphi\right)^{2m+1}}{m!(2m+1)}, & \text{(C.5)}
\end{aligned}$$

the error function. Hence, the corresponding integral leads to

$$\mathcal{I}_3 = \frac{1}{\pi^{3/2}}\sum_{n=0}^{\infty}\sum_{m=0}^{\infty}\frac{(-1)^m}{n!m!(2m+1)}\int_0^{2\pi}\mathrm{d}\varphi\left[K\cos\varphi\right]^{2(n+m+1)}. \tag{C.6}$$

Performing the replacement $l = n + m$, we write n in terms of l and

$$\mathcal{I}_3 = \frac{1}{\pi^{3/2}}\sum_{l=0}^{\infty}\frac{1}{l!}\sum_{m=0}^{l}\left(\begin{array}{c} l \\ m \end{array}\right)\frac{(-1)^m}{2m+1}\int_0^{2\pi}\mathrm{d}\varphi\left[K\cos\varphi\right]^{2(l+1)}. \tag{C.7}$$

The sum over m can be obtained from the identity

$$\sum_{m=0}^{l} \left(\begin{array}{c} l \\ m \end{array} \right) \frac{(-1)^m}{2m+1} = \int_0^1 (1-x^2)^l \mathrm{d}x = \int_0^{\pi/2} \mathrm{d}\phi \cos^{2l+1}\phi = \frac{\sqrt{\pi}}{2} \frac{\Gamma(l+1)}{\Gamma(l+3/2)}. \tag{C.8}$$

On the other hand, the remaining integral takes the value

$$\int_0^{2\pi} \mathrm{d}\varphi \ \cos^{2(l+1)}\varphi = 2\sqrt{\pi} \frac{\Gamma(l+3/2)}{\Gamma(l+2)}, \tag{C.9}$$

yielding

$$\mathcal{I}_3 = \frac{1}{\sqrt{\pi}} \sum_{l=0}^{\infty} \frac{K^{2(l+1)}}{l!} \frac{\Gamma(l+1)}{\Gamma(l+2)} = \frac{1}{\sqrt{\pi}} \sum_{l=0}^{\infty} \frac{K^{2(l+1)}}{(l+1)!} = \frac{1}{\sqrt{\pi}} \left(e^{K^2} - 1 \right), \tag{C.10}$$

in agreement with Eq. (4.37) of the text.

C.2 Focalization in perturbed Hamiltonians

Here we calculate the integral from Eq. (5.38) in the approximation for strong perturbations where the dominant term is

$$I = \int_0^{\infty} \mathrm{d}\eta \ \eta^2 \exp\left(-\eta^2\right) \exp\left(-\frac{\gamma t_1}{\nu\eta}\right). \tag{C.11}$$

By writing the last exponential as the following Gaussian integral

$$\exp\left(-\frac{\gamma t_1}{\nu\eta}\right) = \sqrt{\frac{\eta}{\pi}} \int_{-\infty}^{\infty} \mathrm{d}\rho \exp\left(-\eta\rho^2 + 2\mathrm{i}\sqrt{\frac{\gamma t_1}{\nu}}\rho\right), \tag{C.12}$$

we can include this

$$I = \frac{1}{\sqrt{\pi}} \int_0^{\infty} \mathrm{d}\eta \ \eta^{5/2} \int_{-\infty}^{\infty} \mathrm{d}\rho \exp\left(-\eta^2 - \eta\rho^2 + 2\mathrm{i}\sqrt{\frac{\gamma t_1}{\nu}}\rho\right) \tag{C.13}$$

$$= \frac{1}{\sqrt{\pi}} \int_{-\infty}^{\infty} \mathrm{d}\rho \exp\left(2\mathrm{i}\sqrt{\frac{\gamma t_1}{\nu}}\rho\right) F(\rho), \tag{C.14}$$

with

$$F(\rho) = \int_0^{\infty} \mathrm{d}\eta \ \eta^{5/2} \exp\left(-\eta^2 - \eta\rho^2\right). \tag{C.15}$$

In the Fig C.1 we plot the integrand of $F(\rho)$ as a function of ρ and η.

As we can observe, the function diminishes for values thar are far from the origin at $\rho = 0$. Hence, we can take the quadratic form by expanding $F(\rho)$ up to the second order where

$$F(0) = F_0 = \int_0^{\infty} \mathrm{d}\eta \ \eta^{5/2} \exp\left(-\eta^2\right) = \frac{1}{2}\Gamma\left(\frac{7}{4}\right), \tag{C.16}$$

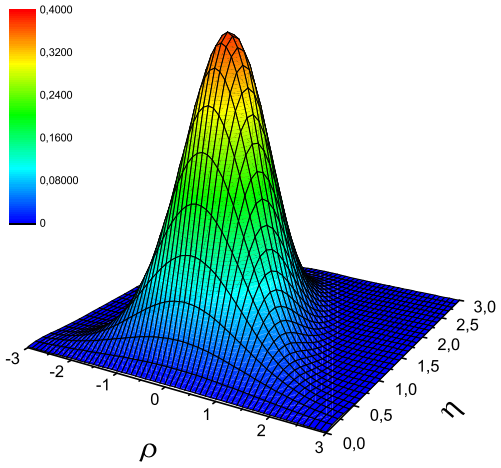

Figure C.1: Integrand of $F(\rho)$ as a function of ρ and the integral variable η. Because of the quadratic dependence of ρ, this function decreases from the center at $\rho = 0$.

and

$$\frac{1}{2!}\frac{\mathrm{d}^2}{\mathrm{d}\rho^2}F(\rho)\bigg|_{\rho=0} = -\int_0^\infty \mathrm{d}\eta\ \eta^{7/2}\exp\left(-\eta^2\right) = -\frac{1}{2}\Gamma\left(\frac{9}{4}\right) = -c. \tag{C.17}$$

Since the decrease in ρ is fast we can approximate $F(\rho)$ by the Gaussian

$$F(\rho) \simeq F_0 - c\rho^2 \simeq F_0 \exp\left(-\frac{c}{F_0}\rho^2\right), \tag{C.18}$$

that yields the form

$$I = \frac{F_0}{\sqrt{\pi}}\int_{-\infty}^{\infty}\mathrm{d}\rho \exp\left(-\frac{c}{F_0}\rho^2 + 2\mathrm{i}\sqrt{\frac{\gamma t_1}{\nu}}\rho\right) \tag{C.19}$$

$$= \frac{F_0^{3/2}}{c^{1/2}}\exp\left(-\frac{F_0}{c}\frac{\gamma t_1}{\nu}\right). \tag{C.20}$$

Therefore, the obtained focalization writes

$$m(t_1,t_2) = \frac{\mathcal{A}_N}{\mathcal{A}}\tilde{\tau}\ 2\sqrt{\pi}\frac{F_0^{3/2}}{c^{1/2}}\exp\left(-\frac{F_0}{\sqrt{\pi}c}\frac{t_1}{\tilde{\tau}}\right) \tag{C.21}$$

$$= \frac{\mathcal{A}_N}{\mathcal{A}}\tilde{\tau}\ c_1\exp\left(-c_2\frac{t_1}{\tilde{\tau}}\right), \tag{C.22}$$

where

$$c_1 = \frac{2\sqrt{\pi}F_0^{3/2}}{c^{1/2}} \simeq 1.467158305, \tag{C.23}$$

$$c_2 = \frac{F_0}{\sqrt{\pi}c} \simeq 0.4576558577. \tag{C.24}$$

Bibliography

[ABS02] A.D. Armour, M.P. Blencowe and K.C. Schwab. *Entanglement and Decoherence of a Micromechanical Resonator via Coupling to a Cooper-Pair Box*. Phys. Rev. Lett. **88**, 148301 (2002).

[All69] G.R. Allcock. *The time of arrival in quantum mechanics I: formal considerations*. Ann. Phys. (N.Y.) **53**, 253 (1969).

[Arg96] N. Argaman. *Semiclassical analysis of the quantum interference corrections to the conductance of mesoscopic systems*. Phys. Rev. B **53**, 7035 (1996).

[BBh97] M. Brack and R.K. Bhaduri. *Semiclassical Physics*. Addison-Wesley, Reading, MA, 1997.

[BEM01] A.D. Baute, I.L. Egusquiza and J.G. Muga. *Sources of quantum waves*. J. Phys. A **34**, 4289 (2001).

[BFi02] C. Bardos and M. Fink. *Mathematical foundations of the time reversal mirror*. Asymptotic Analysis **29**, 157 (2002).

[BHa84] R.G. Brewer and E.L. Hahn. *Atomic memory*. Sci. Am. **251** (6), 50 December issue (1984).

[BRy03] G. Bal and L. Ryzhik. *Time reversal and refocusing in random media*. SIAM J. Appl. Math. **63**, 1475 (2003).

[CBB08] S. Catheline, N. Benech, J. Brum and C. Negreira. *Time reversal of elastic waves in soft solids*. Phys. Rev. Lett. **100**, 064301 (2008).

[CCG86] G. Casati, B.V. Chirikov, I. Guarneri and D.L. Shepelyansky. *Dynamical stability of quantum "chaotic" motion in a hydrogen atom*. Phys. Rev. Lett. **56**, 2437 (1986).

[CDP07] H.L. Calvo, E.P. Danieli and H.M. Pastawski. *Time reversal mirror and perfect inverse filter in a microscopic model for sound propagation*. Physica B **398**, 317 (2007).

[CFi92] D. Cassereau and M. Fink. *Time-reversal of ultrasonic fields - Part III: theory of the closed time-reversal cavity*. IEEE Trans. UFFC **39**, 579 (1992).

[Chu02] S. Chu. *Cold atoms and quantum control*. Nature **416**, 206 (2002).

[CJP08] H.L. Calvo, R.A. Jalabert and H.M. Pastawski. *Semiclassical theory of time-reversal focusing*. Phys. Rev. Lett. **101**, 240403 (2008).

[CLP06] F.M. Cucchietti, C.H. Lewenkopf and H.M. Pastawski. *Decay of the Loschmidt echo in a time-dependent environment*. Phys. Rev. E **74**, 026207 (2006).

[CPa06] H.L. Calvo and H.M. Pastawski. *Dynamical phase transition in vibrational surface modes*. Braz. J. Phys. **36**, 963 (2006).

[CPa07] H.L. Calvo and H.M. Pastawski. *Pair Partitioning in time reversal acoustics*. Mec. Comp. **XXVI**, 74 (2007).

[CPa10] H.L. Calvo and H.M. Pastawski. *Exact time-reversal focusing of acoustic and quantum excitations in open cavities: the perfect inverse filter*. Accepted for publication in EPL, 2010. arXiv:1003.1941

[CPJ04] F.M. Cucchietti, H.M. Pastawski and R.A. Jalabert. *Universality of the Lyapunov regime for the Loschmidt echo*. Phys. Rev. B **70**, 035311 (2004).

[CPJ09] H.L. Calvo, H.M. Pastawski and R.A. Jalabert. *Time-Reversal Mirrors in Chaotic Cavities*. "Complex Phenomena in Nanoscale Systems" 37, G. Casati and D. Matrasulov (eds.), NATO Science for Peace and Security Series B. Springer Science+Business Media B.V. 2009.

[CPW02] F.M. Cucchietti, H.M. Pastawski and D.A. Wisniacki. *Decoherence as decay of the Loschmidt echo in a Lorentz gas*. Phys. Rev. E **65**, 045206 (2002).

[DFi97] C. Draeger and M. Fink. *One-channel time reversal of elastic waves in a chaotic 2D-silicon cavity*. Phys. Rev. Lett. **79**, 407 (1997).

[DPL04] E.P. Danieli, H.M. Pastawski and P.R. Levstein. *Spin projection chromatography*. Chem. Phys. Lett. **384**, 306 (2004).

[DRF95] A. Derode, P. Roux and M. Fink. *Robust acoustic time reversal with high-order multiple scattering*. Phys. Rev. Lett. **75**, 4206 (1995).

[EAH02] G.F. Edelman, T. Akal, W.S. Hodkiss, S. Kim, W.A. Kuperman and H.C. Song. *An initial demonstration underwater acoustic communication using time reversal*. IEEE J. Ocean Eng. **27**, 602 (2002).

[Eco06] E. Economou. *Green's functions in Quantum Physics*. Springer-Verlag, Berlin, 2006.

[Fin97] M. Fink. *Time Reversed Acoustics*. Phys. Today **50** (3), 34 (1997).

[Fin99] M. Fink. *Time-reversed acoustics*. Sci. Am. **281** (5), 67 November issue (1999).

[Fin01] M. Fink. *Chaos and time-reversed acoustics*. Phys. Scr. **T90**, 268 (2001).

[FMT03] M. Fink, G. Montaldo and M. Tanter. *Time-reversal acoustics in biomedical engineering*. Annu. Rev. Biomed. Eng. **5**, 465 (2003).

[GMM95] G. García-Calderón, J.L. Mateos and M. Moshinsky. *Resonant spectra and the time evolution of the survival and nonescape probabilities*. Phys. Rev. Lett. **75**, 337 (1995).

[GWK09] M. Gutierrez, D. Waltner, J. Kuipers and K. Richter. *Semiclassical theory for decay and fragmentation processes in chaotic quantum systems*. Phys. Rev. E **79**, 046211 (2009).

[GWR08] A. Goussev, D. Waltner, K. Richter and R.A. Jalabert. *Loschmidt echo for local perturbations: non-monotonic cross-over from the Fermi-Golden-Rule to the escape-rate regime*. New J. Phys. **10**, 093010 (2008).

[Hah50] E.L. Hahn. *Spin echoes*. Phys. Rev. **80**, 580 (1950).

[HSt04] B.E. Henty and D.D. Stancil. *Multipath-Enabled Super-Resolution for rf and Microwave Communication using Phase-Conjugate Arrays*. Phys. Rev. Lett. **93**, 243904 (2004).

[HTS92] E.J. Heller, S. Tomsovic and M.A. Sepúlveda. *Time domain approach to semiclassical dynamics: breaking the log time barrier*. Chaos **2**, 105 (1992).

[JPa01] R.A. Jalabert and H.M. Pastawski. *Environment-independent decoherence rate in classically chaotic systems*. Phys. Rev. Lett. **86**, 2490 (2001).

[Kuh87] T.S. Kuhn. *Black-body theory and the quantum discontinuity*. University of Chicago Press 1894, 1987.

[Kup06] W.A. Kuperman. *Acoustical Society of America: Silver Medal in Biomedical ultrasound/Bioresponse to Vibration and Acoustical Oceanography*. J. Acoust. Soc. Am. **119** (5), 3359 (2006).

[LRT04] G. Lerosey, J. de Rosny, A. Tourin, A. Derode, G. Montaldo and M. Fink. *Time reversal of electromagnetic waves*. Phys. Rev. Lett. **92**, 193904 (2004).

[LRT07] G. Lerosey, J. de Rosny, A. Tourin and M. Fink. *Focusing beyond the diffraction limit with far-field time reversal*. Science **315**, 1120 (2007).

[LUP98] P.R. Levstein, G. Usaj and H.M. Pastawski. *Attenuation of polarization echoes in NMR: a study of the emergence of dynamical irreversibility in many-body quantum systems.* J. Chem. Phys. **108**, 2718 (1998).

[MBB00] A.L. Moustakas, H.U. Baranger, L. Balents, A.M. Sengupta and S.H. Simon. *Communication through a diffusive medium: coherence and capacity.* Science **287**, 287 (2000).

[MBS97] Z.L. Mádi, B. Brutscher, T. Schulte-Herbruggen, R. Bruschweiller and R.R. Ernst. *Time-resolved observation of spin waves in a linear chain of nuclear spins.* Chem. Phys. Lett. **268**, 300 (1997).

[MKB74] L. Müller, A. Kumar, T. Baumann and R.R. Ernst. *Transient oscillations in NMR cross-polarization experiments in solids.* Phys. Rev. Lett. **32**, 1402 (1974).

[MPN07] G. Montaldo, N. Perez, C. Negreira and M. Fink. *The spatial focusing of a leaky time reversal chaotic cavity.* Wave Random Complex **17**, 67 (2007).

[Pas92] H.M. Pastawski. *Classical and quantum transport from generalized Landauer-Büttiker equations. II. Time-dependent resonant tunneling.* Phys. Rev. B **46**, 4053 (1992).

[PUL01] H.M. Pastawski, G. Usaj and P.R. Levstein *Quantum Chaos: an answer to the Boltzmann-Loschmidt controversy? An experimental approach.* "Some Contemporary Problems of Condensed Matter Physics", V.V. Dvoeglazov, S.J. Vlaev and L.M. Gaggero Sager, eds. New York: NOVA Science Publ., Inc. 2001. p. 223-258.

[PDC07] H.M. Pastawski, E.P. Danieli, H.L. Calvo and L.E.F. Foa Torres. *Towards a time-reveral mirror for quantum systems.* EPL **77**, 40001 (2007).

[PFM02] H.M. Pastawski, L.E.F. Foa Torres and E. Medina. *Electron-Phonon interaction and electronic decoherence in molecular conductors.* Chem. Phys. **281**, 257 (2002).

[PLU95] H.M. Pastawski, P.R. Levstein and G. Usaj. *Quantum dynamical echoes in the spin diffusion in mesoscopic systems.* Phys. Rev. Lett. **75**, 4310 (1995).

[PLU00] H.M. Pastawski, P.R. Levstein, G. Usaj, J. Raya and J. Hirschinger. *A nuclear magnetic resonance answer to the Boltzmann-Loschmidt controversy?.* Physica A **283**, 166 (2000).

[PMe01] H.M. Pastawski and E. Medina. *Tight Binding methods in quantum transport through molecules and small devices: from the coherent to the decoherent description.* Rev. Mex. Fís. **47**, 1 (2001).

[PUL96] H.M. Pastawski, G. Usaj and P.R. Levstein. *Quantum interference phenomena in the local polarization dynamics of mesoscopic systems: an NMR observation*. Chem. Phys. Lett. **261**, 329 (1996).

[Rae96] H. De Raedt. *Computer simulation of quantum phenomena in nano-scale devices*. Ann. Rev. of Comp. Physics **IV**, 107 (1996).

[RFP06] E. Rufeil-Fiori and H.M. Pastawski. *Non-Markovian decay beyond the Fermi Golden Rule: survival collapse of the polarization in spin chains*. Chem. Phys. Lett. **420**, 35 (2006).

[RPW71] W.K. Rhim, A. Pines and J.S. Waugh. *Violation of the spin-temperature hypothesis*. Phys. Rev. Lett. **25**, 218 (1971).

[RTD04] J. de Rosny, A. Tourin, A. Derode, B. van Tiggelen and M. Fink. *Relation between time reversal focusing and coherent backscattering in multiple scattering media: A diagrammatic approach*. Phys. Rev. E **70**, 046601 (2004).

[Rub63] R.J. Rubin. *Momentum autocorrelation functions and energy transport in harmonic crystals containing isotopic defects*. Phys. Rev. **131**, 964 (1963).

[Sie99] M. Sieber. *Geometrical theory of diffraction and spectral statistics*. J. Phys. A **32**, 7679 (1999).

[SRo05] K.C. Schwab and M.L. Roukes. *Putting Mechanics into Quantum Mechanics*. Phys. Today **58** (7), 36 (2005).

[SSc98] R.K. Snieder and J.A. Scales. *Time-reversed imaging as a diagnostic of wave and particle chaos*. Phys. Rev. E **58**, 5668 (1998).

[TDF01] A. Tourin, A. Derode and M. Fink *Sensitivity to perturbations of a time-reversed acoustic wave in a multiple scattering medium*. Phys. Rev. Lett. **87**, 274301 (2001).

[TSo07] G. Tanner and N. Sondergaard. *Wave chaos in acoustics and elasticity*. J. Phys. A **40**, R443 (2007).

[TTF00] M. Tanter, J-L. Thomas and M. Fink. *Time reversal and the inverse filter*. J. Acoust. Soc. Am. **108**, 223 (2000).

[UPL98] G. Usaj, H.M. Pastawski and P.R. Levstein. *Gaussian to exponential crossover in the attenuation of polarization echoes in NMR*. Mol. Phys. **95**, 1229 (1998).

[VRA07] F. Vignon, J. de Rosny, J-F. Aubry and M. Fink. *Optimal adaptive focusing through heterogeneous media with the minimally invasive inverse filter*. J. Acoust. Soc. Am. **122**, 2715 (2007).

[WGG08] D. Waltner, M. Gutierrez, A. Goussev and K. Richter. *Semiclassical mechanism for the quantum decay in open chaotic systems*. Phys. Rev. Lett. **101**, 174101 (2008).

[Whe94] J.A. Wheeler. *Physical origins of time asymmetry*. Perez Mercader and W. H. Zurek eds., Cambridge University Press 1, 1994.

[WLE93] H. van Willigen, P.R. Levstein and M. Ebersole. *Application of Fourier transform electron paramagnetic resonance in the study of photochemical reactions*. Chem. Rev. **93**, 173 (1993).

[WVP02] D.A. Wisniacki, E.G. Vergini, H.M. Pastawski and F.M. Cucchietti. *Sensitivity to perturbations in a quantum chaotic billiard*. Phys. Rev. E **65**, 055206 (2002).

[Zew00] A.H. Zewail. *Femtochemistry: atomic-scale dynamics of the chemical bond*. J. Phys. Chem. A. **104**, 5660 (2000).

[ZME92] S. Zhang, B.H Meier and R.R. Ernst. *Polarization echoes in NMR*. Phys. Rev. Lett. **69**, 2149 (1992).